A time-space synchronization of coherent Doppler scanning lidars for 3D measurements of wind fields

Vasiljevic, Nikola

Publication date:
2014

Document Version
Publisher's PDF, also known as Version of record

A time-space synchronization of coherent Doppler scanning lidars for 3D measurements of wind fields

DTU Wind Energy - PhD

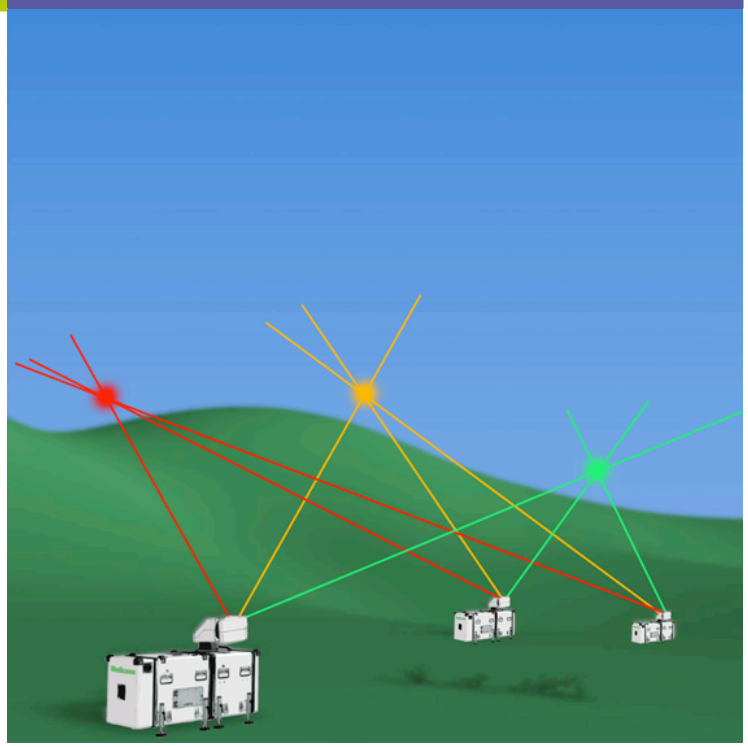

Nikola Vasiljević

DTU Wind Energy PhD-0027 (EN)

April 2014

DTU Wind Energy
Department of Wind Energy

Author: Nikola Vasiljević
Title: A time-space synchronization of coherent Doppler scanning lidars for 3D measurements of wind fields
Department: DTU Wind Energy

Abstract:

This thesis consists of the results of a Ph.D. study that was focused on the development of the system of three time-space synchronized pulsed coherent Doppler scanning lidars, which are coordinated by a remote 'master computer'. This system has the unique capability to measure a complete three-dimensional flow field by emitting the laser beams from the three spatially separated lidars, directing them to intersect, and moving the beam intersection over an area of interest.

Each individual lidar was engineered to be powered by two real servo motors, and one virtual stepper motor. The stepper motor initiates the laser pulse emission and acquisition of the backscattered light, while the two servo motors conduct the scanner head rotation that provides means to direct the laser pulses into the atmosphere. By controlling the rotation of the three motors from the motion controller the strict synchronization and time control of the emission, steering and acquisition were achieved, resulting that the complete lidar measurement process is controlled from the single hardware component.

The system was formed using a novel approach, in which the master computer simultaneously coordinates the remote lidars through a UDP/IP and TCP/IP network by exchange of network packets. Since the size of the packets is roughly 1 kB, this approach allows an uninterrupted and fast coordination of the lidars, even in the case of mobile networks such as GSM. With this approach a maximum lag of 10 ms was observed in terms of the scanner heads' rotation and the measurements among the lidars in the system.

The laser beam pointing accuracy of each lidar was estimated to $\pm 0.5^\circ$ for the laser beam direction, and roughly ± 5 m for the sensing distance. A set of procedures were proposed that can improve the pointing accuracy by a factor of 20.

Subsequently, two experiments were carried out in which the developed multiple lidars system was used to synchronously measure wind velocity fields in multiple points in the atmosphere.

DTU Wind Energy
PhD-0027 (EN)

2014

ISBN 978-87-92896-62-9

Sponsorship:
WAUDIT, WindScanner.dk

Contact information:
niva@dtu.dk
nikola@nikolavasiljevic.com

Pages: 173
References: 84

Technical University of Denmark
DTU Wind Energy
Risø Campus
Frederiksborgvej 399
DK-4000 Roskilde

www.vindenergi.dtu.dk

For my mother and sister -
whose love gave me the strength to complete this *magnum opus*

Preface

This research was carried out as a Ph.D. project within "Test and measurement" section of DTU Wind Energy. It was supervised by senior scientist Michael Courtney, and co-supervised by Professor Jakob Mann. The work started on the 1^{st} of June 2010 and was finished on the 31^{st} of December 2013. It comprised three industrial secondments, two of which took place at the French lidar manufacturer Leosphere, from February 2011 until May 2011 and from February 2012 until June 2012. The third secondment took place at the British motion system integrator Heason in September 2013.

From the 1^{st} of June 2010 until the 1^{st} of June 2013 the Ph.D. project was funded by the European Commission through the Marie Curie FP7-ITN-WAUDIT Project, under the grant number # 238576. The secondments and the period from the 1^{st} of June 2013 until the 31^{st} of December 2013, were financially supported by the WindScanner.dk project. The WindScanner.dk project was funded by the Danish Agency for Science, Technology and Innovation through the grant number # 2136-08-0022.

The Ph.D. project focused on the development of a system of coherent Doppler scanning lidars, known as the long-range WindScanner system, for three-dimensional (3D) measurements of wind velocity fields within a large volume of the atmospheric boundary layer (ABL).

A minimum of three spatially separated coherent Doppler scanning lidars are needed to perform this type of measurements, since a single lidar is only able to measure the component of wind velocity projected on the lidar laser beam propagation path, thus measuring only a portion of the vector. By steering three laser beams to meet at the point of interest, the wind velocity can be measured. Furthermore, by moving the beam intersection over an area of interest, the complete wind velocity field can be measured. This requires time-space synchronization of the coherent Doppler scanning lidars. The previous statement formulated the main research question, which was:

"***How to develop a multiple coherent scanning Doppler lidar system whose lidars are time-space synchronized?***"

This question will be answered through the example of the long-range WindScanner system development, whose three pulsed coherent Doppler scanning lidars are time-space synchronized.

The research has its special significance in solving the lack of wind velocity fields measurements at full scale, thus providing the basis for the advancement of our understanding of the flows in the ABL, relating to wind energy in particular. Given all this, this Ph.D. project can be characterized as applied research, with the quantitative-experimental approach. The research represents a mix of control theory, signal processing, computer science and electrical engineering.

The thesis, which summarizes the results of the research, includes a method for the time-space synchronization of coherent Doppler scanning lidars. The thesis is focused on practical solutions, since the ambition of the Waudit and the WindScanner.dk project was to generate new knowledge that is immediately applicable in industry, particularly in the wind energy sector. However, necessary theoretical discussions are included in the thesis.

A reader of this thesis will gain the following insights into:

- The fundamental processes of a coherent Doppler lidar that provide grounds for the radial velocity measurements
- How to synchronize the laser pulse emission, laser pulse steering and the acquisition of backscattered light
- How to form a system of coherent Doppler scanning lidars that is able to measure all three components of the wind velocity over a volume of interest
- How to achieve time synchronization of coherent Doppler scanning lidars in the system
- What are the contributions to the uncertainty of the laser beam pointing, which influence the space synchronization of coherent Doppler scanning lidars
- What tests are advisable in order to quantify the uncertainty
- How to improve the laser beam pointing accuracy, and thus the space synchronization of the coherent Doppler scanning lidars

This thesis has been adapted for a wide audience, ranging from atmospheric scientists, who need appropriate instrumentation for their ABL investigations, to industry, which seeks ideas for building complex wind velocity measurement systems. Above all, the thesis is aimed at future Ph.D. students, and everybody else who will use, modify and/or improve the long-range WindScanner system.

A short description of the contents of each chapter is given below.

Chapter 1: Introduction gives a brief explanation on why the wind energy research and the wind energy sector are moving from traditional anemometry, which includes wind velocity measurements from mast mounted sensors, towards coherent Doppler lidars. The chapter also includes the review of the experiments conducted with multiple coherent Doppler scanning lidars, and the

WindScanner.dk project presentation.

Chapter 2: Engineering coherent Doppler scanning lidars explains the operational principles and the architecture of the software applied to the development of the pulsed coherent Doppler scanning lidars that the long-range WindScanner system consists of. These operational principles and the architecture of the software provide the synchronization and the accurate time control of the laser pulse emission, steering of the laser pulses, and the acquisition of the backscattered light. This forms the foundation for the time-space synchronization of the coherent Doppler scanning lidars in the long-range WindScanner system. Also, this chapter includes the theoretical background of the coherent Doppler lidar radial velocity measurements.

Chapter 3: Unifying lidars in the single measurement system addresses the formation of the long-range WindScanner system which, along with the three lidars, also includes a remote 'master computer'. This chapter describes the application layer protocol that allows the communication between the master computer and the lidars. The chapter provides information on how the time synchronization is achieved among the coherent Doppler scanning lidars in the long-range WindScanner system.

Chapter 4: Uncertainty of the laser beam pointing deals with the space synchronization of the coherent Doppler scanning lidars in the long-range WindScanner system. It describes sources of uncertainty in a Doppler scanning lidar beam pointing. It devises the tests for each source of uncertainty and it provides the first estimation of total uncertainty. This chapter also includes suggestions on how to improve the laser beam pointing accuracy, and thus the space synchronization of the coherent Doppler scanning lidars in the long-range WindScanner system.

Chapter 5: Swinging musketeer experiment gives details on the first experiment with the long-range WindScanner system, which has been performed to validate the application of concepts and software solutions for wind velocity measurements. The experiment consisted of measurements of the wind velocity at three points of interest, which were located close to three sonic anemometers.

Chapter 6: IBL WiSH experiment addresses the second experiment with the long-range WindScanner system in which the three long-range WindScanners were used to acquire components of the wind velocity in a large volume of the atmosphere for the investigation of changes of a sea-land internal boundary layer (IBL).

Chapter 7: Conclusion sums up the main conclusions that can be drawn from this thesis.

Nikola Vasiljević
Roskilde, April 1, 2014.

Notes to the printed thesis

The results of this thesis were presented for the public examination and debate on July 7, 2014 at the Technical University of Denmark, Risø Campus, Roskilde. The evaluation committee consisted of Head of Section Hans E. Jørgensen (DTU Wind Energy), Dr. Michael S. Margulis (Lockheed Martin), and Dr. Ir. Adrian M. Rankers (Mechatronics Academy).

Some minor corrections have been made to the originally submitted thesis before printing.

Nikola Vasiljević
Roskilde, November 24, 2014.

Acknowledgment

Somewhere I have read that the acknowledgement chapter of a PhD thesis can be written without the scientific rigor. I will take this suggestion since I feel that I have been bounding myself within somewhat dry language of academia, where hardly one can grasp the author's personality, apart from his/hers ability to produce impeccable scientific results.

Unlike many other Ph.D. students who typically start this chapter by acknowledging their supervisors, advisors, bosses, etc. I will start by thanking to my family.

Zorica Vasiljević, my mother, was present either physically or spiritually in every moment, from giving me hug full of reassurance at the airport Nikola Tesla in Belgrade together with my uncle Radojica Ćiraković when I went for the interview for this position, during the hard times when the whole project was at the edge of total failure, till the day when the assessment committee gave their final decision. She is probably one of a few people that know how the whole system functions, since she was the first person to hear all my ideas, concepts and approaches to solve often difficult problems.

My sister Milica Vasiljević was reading most of the things I wrote, checking if the graphical representation of concepts and results are neatly made, self explanatory and eye-catching. She had made many gloomy winter days in Denmark enjoyable. Simply Milica was a true companion throughout this journey.

Without Zorica and Milica, hardly the long-range WindScanner system would reach the form which it has now, hardly I will complete my Ph.D. studies, and hardly I would take the most from all the situations I have been through. They are the two most important persons in my life.

I would like to thank to my supervisor Mike Courtney and co-supervisor Jakob Mann for devoting their energy to achieve the success of this Ph.D. project. Their support, comments, critics and skillful teaching were exceptionally useful and appreciated. Particularly, I would like to express my gratitude to Mike Courtney for being not just a supervisor, but a great friend and my family in Denmark together with Maria Fay Courtney Bohr (lil sis). Mike you gave me wings to travel, meet new people, and find myself in terms of research.

In order to materialize ideas and concepts one need to have an enthusiastic and skillful person to work with (minimum one). With that person he or she needs to share the same dream. Luckily I met Guillaume Lea in 2011 during my first stay in Leosphere. We both share the same passion for technology, we

have wild imagination and vision, and hardly something or someone can stop us to achieve what we have on our minds. All this comes with emotions, so beware. Since 2011 we became a dream team for scanning lidars (aka Long-Rangers), and the long-range WindScanner system is the product of two pair of hands, Guillaume's and mine. However, if Stéphanie Bertin-Hugault was not as supportive, loving and carrying, hardly Guillaume would share an office with me today. So thank you Stéph very much!

Poul Hummelshøj was taking quite some risks by backing up some of my wild ideas, and protecting me along the process of the WindScanner development. Not everybody can grasp my personality as good as Poul. He always found ways to provide me what I needed, and somehow he knew in advance what I will ask for (I think he can read my mind).

The idea about WindScanner systems originates from Torben Mikkelsen, whose vision and enthusiasm brought the WindScanner.dk project. I am thankful to Torben for the trust he had in me and all the support he gave when I took over the development of the long-range WindScanner system.

I think this is a good moment to thank to Javier Sanz Rodrigo for setting up the WAUDIT project, and opening the opportunity for many of us who became the WAUDIT fellows to explore new things with sufficient amount of funding.

Not everybody likes to be outside warm office during cold windy rainy days. A good gear is not sufficient, while warm heart, positive attitude, spirit of adventure and curiosity are essential. Per Hansen has it all. He was there with me in numerous field activities, from the preparation of the field trips, installation and decommissioning, to the on site repair. He is truly 'one and the only'.

Same goes to Claus Pedersen, who saved us lot of trouble by grounding properly electrical components in our WindScanners. Before that we have been getting a regular electro-shock therapy while plugging our devices to the power, at the same time we were unable to explain why we have an extent of outgoing laser pulses (this one is a long story, which deserves a whole chapter).

Great things happen outside the confront zone. This sounds prosaic, and rather philosophical, however it is true. Jacob Berg and Mark Kelly were the first scientists that used the long-range WindScanner system, who at the same time loudly and clearly 'advertize' it in the MET section. Not many people have guts to do that, since the confront of the known overwhelms the initial discomfort of the unknown. However, if it does not hurt it is not worth. I owe them big thank for this. Moreover, Jacob Berg was extremely supportive in crucial moments of my Ph.D. studies, when seeing the end of it all was almost impossible. He is a great roll model to me.

The question of what the scientific writing really means and how it should be performed was giving me nightmares in early months of the thesis writing. Alfredo Peña Diaz offered to read some of the things I wrote, and he came with fantastic comments and hints that help me understand the writing process more clearly and go through it with less pain. I am very grateful for his help.

Industrial stays played an important roll in my Ph.D. project. Jean-Pierre Cariou was open to have me in Leosphere in 2011 and 2012. Moreover, he made a

move which is rare in collaborations between industry and academia. He granted me full access to the hardware of Windcube and Leosphere lab, participation in building of the long-range WindScanners/Windcube 200s, and gave me full access to former versions Windcube software with a possibility to use parts of the software (DLLs and hardware libraries) to build the WindScanner Client Software. For all of this I am immensely grateful to him. The same goes to his colleague Guillaume Gorju who helped me understand optics much better, while promptly answering many of my questions. Other employees at Leosphere provided important help. Furthermore, they made my stays in Leosphere and Paris enjoyable (13e/La Butte-aux-Cailles). Because of them I did not feel like l'étranger, but as an essential member of big (EOB) crew. Many of them became truly great friends of mine. Merci Les Vrais!

Now when we are talking about friends and crews, I would like to thank to all my friends from DTU Wind Energy and WAUDIT. Among them I would like to express my gratitude to Iva Hrgovan, Paula Gómez, Louis-Etienne Boudreault, Venkatesh Duraisamy Jothiprakasam, George Fitton, Francesco Cuzzola and Heather Holmes.

The experience I had with Heason is similar to the one I had with Leosphere. My short stay in Heason resulted in a big part of the chapter focused on the laser beam pointing accuracy. Jon Howard was eager to make a test rig which I used for the assessment and improvement of the scanner head positioning accuracy. His advices and support for many of my activities related to the motion control were of great importance. I am utterly grateful for this, and for the possibility to stay in Heason and see the fantastic world of the motion systems.

During my short stay in ForWind the RSComPro was born. I am thankful to Juan José Trujillo, Davide Trabucchi and Jörge Schneemann for their time, efforts and dedication for the development of the RSComPro.

When I finally wrote the first draft of my thesis I had a big doubt. Can I call what I have done during my Ph.D. studies research, and if yes where my research results belong to. The doubt arose simply because I was surrounded by Ph.D. students doing theoretical research or research based on modeling (which is good stuff don't get me wrong). What I was doing did not fit in this picture. My old mentor and supervisor of diploma and master thesis Miodrag Zlatanović dispel doubts. He devoted solid portion of his time in January 2014 to help me organize the thesis' chapters better, and to adequately find the title of this thesis. Moreover, he explained what research means, and that as my results and findings belong to the applied research I should be proud of what I've done, since there will be many who will use my results. I'll always be grateful to him for being one of rare persons left to stand next to me and give me positive energy in probably the toughest moments of my Ph.D. studies.

For the end I would like to thank to the members of my assessment committee Hans Jørgensen, Michael Margulis and Adrian Rankers for spending time reading the thesis, assessing its contributions, and making the day of my defense extraordinary. Your efforts and your presence at the defense made the end of this Ph.D. studies glorious.

Contents

Acronyms

$2D$	Two-dimensions
$3D$	Three-dimensions
$3DoF$	Three Degrees of Freedom
$6DoF$	Six Degrees of Freedom
ABL	Atmospheric Boundary Layer
AOM	Acousto-Optic Modulator
CNR	Carrier-to-Noise Ratio
CSV	Comma-Separated Values
CW	Continuous-Wave
DBS	Doppler Beam Swinging
$EDFA$	Erbium-Doped Fiber Amplifiers
FFT	Fast Furrier Transform
$IBL\,WiSH$	Internal Boundary Layer, WindScanners at Høvsøre
IP	Internet Protocol
IPS	Internet Protocol Suite
$Lidar$	Light detection and ranging
LO	Local Oscillator
LOS	Line-Of-Sight
MCS	Master Computer Software
MLE	Maximum-Likelihood Estimator
$MusketeerEX$	Musketeer EXperiment
$PMAC$	Programable Multi Axis Controller
PLC	Programable Logic Controller
PPI	Plan Position Indicator
PPM	Parts Per Million
PRF	Pulse Repetition Frequency
RHI	Range Height Indicator
$RSComPro$	Remote Sensing Communication Protocol
TCP	Transmission Control Protocol
UPD	User Datagram Protocol
VAD	Velocity Azimuth Display
VAP	Velocity Azimuth Process
WCS	Windscanner Client Software
$WLAN$	Wireless Local Area Network
XML	Extensible Markup Language

"Let the future tell the truth, and evaluate each one according to his work and accomplishments. The present is theirs; the future, for which I have really worked, is mine."

- Nikola Tesla

Chapter 1

Introduction

1.1 Why do we need coherent Doppler lidars for wind energy?

During the last few decades the wind industry has been developing rapidly. Wind turbines have been growing in size, power and number. Manufacturers such as Enercon, Vestas, Siemens and Gamesa have wind turbines with rotor diameters and hub heights greater than 120 m in their product portfolio. This growth leads to a demand for tall meteorological masts, since the current IEC standard demands that wind turbine power curves have to be derived by measurements of wind velocity with cup-anemometers at hub height [1]. The production, installation and maintenance of such masts are expensive.

In [2, 3], the authors have shown first with simulations, then with experimental data that the power output of a wind turbine correlates significantly better to an 'equivalent wind speed', for which wind velocity measurements at different heights over the swept rotor area are needed, rather than just a single point hub height horizontal wind velocity. If the equivalent wind speed becomes the accepted approach in relating the power output to the wind velocity by a new revision of the IEC standard, this would mean that even taller meteorological masts are needed.

Meanwhile the search for the best unexploited wind resources drives wind turbine installation both further offshore and into more complex terrain onshore. Before a wind farm can be realized a wind resource assessment is performed. This assessment encompasses calculation of the wind farm power production based on the wind velocity measurements from the site and power curves of future wind turbines. For this study, it is recommended to measure the wind velocity at future hub heights of wind turbines for period of at least one year [4].

In the experiment [5] authors have shown that even in a case of a smooth surface such as sea surface, near-shore, the wind velocity field above it shows strong spatial and temporal variability, which means that the wind velocity

measurements from a single meteorological mast are not representative of the whole area of the future wind farm. Therefore, more than one meteorological mast is advisable in order to reduce the uncertainty in the estimation of the power production of the future wind farm.

Typically, in order to reduce the costs of the wind resource studies, they are often performed with wind velocity measurements from as few meteorological masts as possible in conjunction with ABL flow models. These models, such as WAsP [6], extrapolate wind velocity horizontally and vertically over the area of the future wind farm using wind velocity measurements from a single point and wind farm site's orography and roughness data. Therefore, they produce artificially measurements at multiple locations and they create wind velocity maps over a large area of interest. The wind velocity maps are further used to optimize the layout of the future wind farm and to estimate the power production.

The combination of flow models and in-situ measurements gives acceptable results for both flat terrain and offshore. However, the models fail to predict the behavior of complex flows, encountered in complex terrain, which can have damaging effects on wind turbines.

Efforts to improve the flow modeling rely heavily on comparisons to flow measurements performed at full scale. For a long time, wind velocity measurements acquired during the Askervein hill experiment [7], from 50 masts, represented a test case for the flow models validation in complex terrain [8, 9, 10, 11]. In the current state of the flow models, the Askervein hill is not sufficiently demanding. The recent data set obtained from 10 masts during the experiment which took place at the Bolund peninsula [12, 13] represents a real challenge for flow models [14, 15].

However, the Bolund experiment was not performed at full scale. The peninsula is very small, and the flow over it does not have large scale flow phenomena that are found at many other wind farm sites. New experiments at much larger sites with the Bolund complexity are needed to support progress of the flow modeling. One of the conclusions of the Bolund experiment was that the future experiments should encompass wind velocity measurements within a large volume of the ABL [13]. These experiments are economically and technically challenging using traditional anemometry.

From all above-mentioned, in order to support the current pace of the wind industry and research there is a necessity for cost-effective and at the same time accurate wind velocity measurements from higher heights and greater coverage. Therefore, there is a necessity for alternatives to the existing in-situ techniques with mast mounted wind velocity sensors. The most promising alternative is the optical remote sensing technique based on the coherent detection and the analysis of the Doppler shift with coherent Doppler lidars (LIght Detection And Ranging) [16].

In comparison to the traditional anemometry, coherent Doppler lidars acquire wind velocity measurements remotely, without physical contact with moving air. Coherent Doppler lidars achieve this by directing a beam of laser light into the atmosphere, some of which is reflected back by entrained aerosols particles, which are assumed to have the same velocity as the velocity of the moving

air. The motion of the particles induces a shift in the frequency between the emitted light and backscattered light, known as the Doppler shift, which represents the direct measure of the wind velocity projected on the propagation path of the laser beam. A priori knowledge of the emitted light frequency allows the detection of the Doppler shift in the backscattered light (i.e. coherent detection), and thus the determination of the projected wind velocity. This projected wind velocity, which is known as radial or line-of-sight (LOS) velocity, represents only a part of the three-dimensional vector. Coherent Doppler lidars measure multiple radial velocities along multiple laser light propagation paths and with the use of well-established radar wind retrieval techniques, such as Velocity Azimuth Display (VAD) [17], Doppler Beam Swinging (DBS) [18] or Velocity Azimuth Process (VAP)[19], they estimate two or all three components of the wind velocity under the condition of the horizontal homogeneity of the flow.

Coherent Doppler lidars have several advantages in comparison to traditional anemometry. Usually their deployment is simple. Coherent Doppler lidars are compact, versatile and unlike masts can be easily redeployed to another location. Depending on the design, coherent Doppler lidars can derive wind velocity up to 2 km in height [20] and 20 km in distance [21], which is much higher than conventional masts and with much greater coverage. For coherent Doppler lidar installation, no operation permits are needed, which is often a huge advantage. However, coherent Doppler lidars consume orders of magnitude more power than a mast based wind velocity measurement system and this has to be carefully taken into consideration before deployment.

1.2 Coherent Doppler lidars in wind energy

The coherent Doppler lidars are not novel technology for wind velocity measurements. Feasibility studies for this type of measurements have been performed in the late 1960s [22], while the first coherent Doppler lidar measurements of remote winds occurred in the early 1970s [23]. More extensive use of coherent Doppler lidars for remote wind velocity measurements started in the 1980s, particularly by NOAA [24] and NASA [25]. One of the first attempts to quantify specifications for coherent Doppler lidars for wind energy applications, such as measurements of wind potential over areas of interest and wake flows behind wind turbines, were given in 1983 [26]. In 2002, Coherent Technologies, an American company, introduced the Windtracer the first commercial, eye-safe, long-range scanning coherent Doppler lidar after an extensive work on coherent Doppler lidars, which started in the late 1980s [27]. A wider acceptance of coherent Doppler lidars in wind energy occurred after the introduction of the ZephIR lidars by the British company QinetiQ in 2006, and the Windcube, by the French company Leosphere in 2007. In the meantime other companies started to produce coherent Doppler lidars intended for wind energy applications, where the latest review of the commercial lidars has been presented in [28].

Coherent Doppler lidars have a diverse range of application in wind energy, and they come as a ground- or turbine- based instruments that either emit a pulsed or continuous-wave (CW) light, which is directed using a fixed or arbitrary scanning geometry.

In case of wind resource assessment, ground-based coherent Doppler lidars with fixed scanning geometry for vertical profiling of the wind velocity have shown to be a suitable tool for both coastal and flat terrain sites [29]. Power curve measurements performed with this type of lidars have the same level of accuracy as the ones acquired with mast mounted cup anemometers [3, 30], or can even show higher correlation between input wind velocity and output power if turbine-based coherent Doppler lidars with the fixed scanning geometry for horizontal profiling are used [31, 32]. For some sites, this type of lidar can accelerate power curve measurements by reducing the time needed for their derivation [31, 32]. Turbine-based coherent Doppler lidars seem to be an attractive solution for power curve measurements for offshore wind turbines, since the necessity for the installation of a tall meteorological mast offshore can be eliminated [33].

There are other applications of coherent Doppler lidars where the use of traditional anemometry is either impossible or extremely expensive. Such applications are: an enhancement of the feed-forward control of a wind turbine, mapping of wind turbines wakes and measurement of wind potential over large areas of interest.

In an early study from 2006 [34], the authors examined the requirements for a forward-looking turbine-based coherent Doppler lidar for the turbine control. Also, the authors reviewed potential advantages of an advance warning of wind velocity fluctuations, and they demonstrated, with simulations, the load reduction of a wind turbine if the control of the turbine is supported by the measurements of the incoming flow with the turbine-based coherent Doppler lidar. The first measurements of the incoming flow with the turbine-based coherent Doppler lidar were performed with a prototype ZephIR lidar that was mounted on top of the nacelle behind the rotor on a Nordex N90 turbine [35], while in the field test [36] authors demonstrated for the first time that a turbine-based coherent Doppler lidar can be used to improve collective pitch control of a wind turbine.

Modern wind farms consist of a large number of wind turbines, which are often installed close to each other. Due to the turbine generated wakes, there is always interaction among wind turbines. Consequences of wakes are a wind farm power production deficit and wake-generated loads on wind turbines, i.e. shorter lifetime of wind turbines. Proper modeling of wake flows plays an important role in mitigating these issues, for which the measurements of the flows are important. In the study [37, 38] it has been shown that turbine-based coherent Doppler lidars can produce radial velocity measurements of the wake flow behind a single turbine. The lidars in this study were used to verify a basic assumption for dynamic wake modeling. Similarly ground-based long-range scanning coherent Doppler lidars can be used to measure the wake flow of multiple wind turbines [39].

The long-range scanning coherent Doppler lidars have an interesting application for mapping of wind resources over a large area of interest. Instead of deriving wind velocity maps by coupling a flow model with wind velocity measurements from a few masts, the maps can be produced by applying retrieval techniques on lidars measurements of the radial velocity fields [40].

1.3 The need for multiple coherent Doppler lidars

The retrieval techniques (VAD, DBS, etc.) make a good estimation of the two or all three components of the wind velocity in flat terrain and offshore, since the flow is often horizontally uniform. This has been shown in tests of ground-based commercial vertical profilers in flat terrain and offshore, where the 10-minute average horizontal wind velocity derived by the lidars show close agreement, typically within one percent, with those acquired from co-located mast mounted anemometers [41, 42]. Similar agreement was found in tests of a turbine-based horizontal profiler in flat terrain [32].

As the flow becomes more influenced by terrain orography or nearby objects, the flow becomes more complex, and the condition of the horizontal homogeneity of the flow is no longer satisfied. As a consequence, while applying retrieval techniques assuming the homogeneity, coherent Doppler lidars will derive erroneous wind velocities. It was shown that for ground-based vertical profilers errors in complex terrain of the horizontal wind velocity can be up to 10% [43]. Wind velocity maps produced using ground-based scanning coherent Doppler lidars can have errors of the same order of magnitude [21]. At the same time the application of turbine-based coherent Doppler lidars for power curve measurements in complex terrain is not advisable [32] while, due to high complexity, the wake flow can only be characterized in terms of radial velocities using a single lidar.

If the flow is influenced by terrain orography, to some extent the error can be predicted and decreased using flow models [43, 44]. The results show that this approach is more successful in terrain with gentle slopes [43, 45, 44] than in more complex sites [43]. However, this approach cannot eliminate lidar errors.

The only way of eliminating lidar errors is to avoid the condition of horizontal homogeneity. The condition is unavoidable with a measurement system consisting of a single lidar, since it is necessary to measure multiple independent radial velocities at points of interest in order to avoid the condition. To achieve this it is necessary to have the measurement system that consists of multiple spatially separated coherent Doppler lidars. A minimum of two lidars are needed to characterize two components of the flow, while a minimum of three lidars is needed to completely characterize all three components of the flow.

Dual-Doppler lidar measurement techniques have been used in a diversity of atmospheric studies since the 1980s. In 1982, the first dual-Doppler lidar measurements were recorded during the Joint Airport Weather Studies (JAWS)

Project field experiment [46]. The objective of JAWS was to study convectively driven downdrafts and resulting outflows near the surface. For this experiment, aside from numerous in-situ sensors and a scanning Doppler radar, two long-range coherent scanning Doppler lidars from NOAA and NASA/ERL were used [47]. Each lidar performed multiple Plan Position Indicator (PPI) sector-scans at elevation angles ranging from 1° to 5°, during which the laser beams 'sliced' the atmosphere at multiple horizontal planes (see the PPI graphical representation in Figure 1.1). The laser beams of the two lidars did not intersect at the same time at the points of interest, but rather crossed the points in separate time frames. Since the radial wind velocities were measured at the planes which practically overlapped, analysis of the dual-Doppler measurements allowed calculation of the 2D wind velocity maps of horizontal winds near the surface.

In the Joint Urban 2003 (JU2003) field experiment, two coherent scanning Doppler lidars were operated in Oklahoma City for the purpose of studying the boundary layer transport and dispersion processes in the urban canopy [48]. Similarly to JAWS, the lidars in JU2003 performed coordinated PPI sector-scans at multiple elevation angles, which allowed characterization of the flow in terms of the horizontal velocity vector at the plane of interest [49]. Also, the data from the coordinated PPI scans was used to assess the accuracy of single-Doppler retrievals of microscale wind and temperature fields obtained by four-dimensional variational data assimilation [50]. In addition to the PPI scans, the lidars were configured to perform coordinated Range Height Indicator (RHI) scans at multiple azimuth angles, during which the laser beams 'sliced' the atmosphere at multiple vertical planes (see the RHI graphical representation in Figure 1.1). The planes intersected along 8 vertical axes along which the vertical profiles (i.e. virtual towers) of the horizontal velocity vector were derived under the assumption of the zero vertical component of the wind velocity [51]. The data was used to study the spatial variability of the wind across downtown Oklahoma City.

In rural and urban areas of the United Kingdom, during the Invest-to-Save Budget project 52 (ISB52), two scanning coherent Doppler lidars were used and configured to perform a variety of coordinated PPI and RHI scans, in order to retrieve dispersion relevant parameters to improve dispersion models [52].

Two coherent scanning Doppler lidars played an important role in the instrumentation of the Terrain-Induced Rotor Experiment (T-REX) in the southern Sierra Nevada mountain range [53]. During T-REX, two coherent scanning Doppler lidars were employed for studies of rotary flows in the lee of mountains [54] and for the assessment of an algorithm for 3D wind retrieval using dual-Doppler data [55, 56]. The lidars performed coordinated RHI scans with the same azimuthal angle, which allowed measurements of radial velocities in the same vertical plane, and thus the calculation of the 2D wind velocity maps for the rotary flows studies. Coordinated VAD scans at multiple elevation angles were performed for the assessment of the 3D wind retrieval algorithm (see the VAD graphical representation in Figure 1.1).

Three coherent scanning Doppler lidars were used to characterize in detail the wake of a 2 MW Enercon E-70 wind turbine [57]. Two of the three lidars were

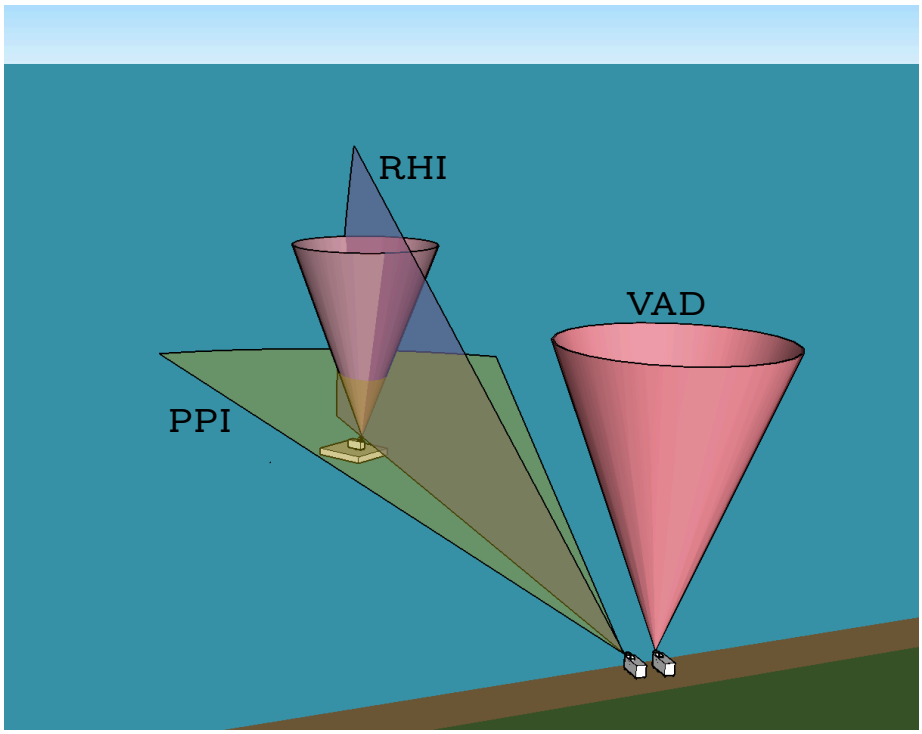

Figure 1.1: Typical scanning scenarios

positioned behind the wind turbine where they performed either coordinated RHI scans or step-stare scans. The third lidar was positioned in front of the turbine and it was used to characterize the incoming flow.

In all the above-described experiments with multiple coherent Doppler lidars, it was possible to measure mean wind velocity fields without the condition of horizontal homogeneity of the flow. It should be noted that the laser beam pointing accuracy was not quantified in the experiments, which means that for the interpretation of radial velocity fields it was assumed that the lidars were synchronized in space (i.e. laser beams crossed the same points of interest). For the measurements of fluctuating wind velocity fields (i.e. turbulence measurements) or for shorter time averages of measurements it is necessary that lidars are synchronized both in time and space, thus it is necessary to have lidars which are able to direct and intersect laser beams at the points of interest at the same time.

So far, there has only been one published study in which three coherent Doppler lidars were used to completely characterize the flow in terms of all three components of the wind velocity. In the Musketeer Experiment (MusketeerEX), using three spatially separated coherent Doppler lidars in a staring mode, the feasibility of the measurements of the fluctuating wind velocity at one point

in the atmosphere was demonstrated for the first time [58]. The installation and the configuration of the three Doppler lidars allowed the intersection of their laser beams at a single point at 78 m above the ground level, close to a sonic anemometer. The time series of the wind velocity made with the sonic anemometer and the three lidars show generally very good correlation [59]. In this experiment lidars were synchronized in time and space, which did not present a challenge since the wind velocity measurements were done only in one point.

The common point of the experiments discussed is that the lidars functioned independently from each other. There was no centralized control or coordination of their activities. Authors in [54] discussed that in order to enhance the dual-Doppler lidar measurement techniques, one of the aspects that needs to be improved is lidar synchronicity. It was commented in [51] that the precise control of synchronicity and spatial co-sampling (A/N time-space synchronization) with two lidars in the field is challenging, while the authors in [54] suggested that this would probably require the centralization of the lidars control with a single computer, clock and scanning algorithm. This means that multiple lidars should be joined into a unified measurement system.

1.4 DTU Wind Energy's windscanner systems

In 2008, DTU Wind Energy, at that time Risø DTU, presented an ambitious idea about the development of the unified measurement systems, known as windscanner systems, which consist of three time-space synchronized scanning coherent Doppler lidars (i.e. WindScanners), specialized for detailed remote measurements of real-time wind velocity fields [58].

The realization of this idea was carried out under the WindScanner.dk project, where the previously described MusketeerEX represented a pilot study. The project started in 2009 with the development of a short-range WindScanner (Figure 1.2). This type of a WindScanner is based on the CW coherent Doppler lidar ZephIR from the British company Natural Power (at that time QinetiQ) and dual-axis, prism-based scanner head [60] designed by DTU Wind Energy and DTU's industrial design company IPU with support from the British motion system integrator Heason. A short-range WindScanner is intended for radial velocity measurements from the range of distances between 10 m and 200 m, with the maximum measurement rate of 400 Hz. Since the short-range WindScanner is based on the CW technology, it is only possible to acquire single radial velocity at any measurement rate. Typically, short-range WindScanners are applied to perform small-scale measurements of 3D wind fields, with a particular scope on measurements of velocity fields in front of, and behind a wind turbine rotor.

The first experiments with short-range WindScanners took place in 2011. In these experiments, a single short-range WindScanner was used for the measurements of the wake of a small building [61] and multiple vertical profiles of horizontal velocity close to the ground including a recirculation zone on an escarpment [62], while the short-range WindScanner system, consisting of two

short-range WindScanners, was used for the measurements of a helicopter downwash [63].

Parallel with the development of the short-range WindScanner, DTU Wind Energy, IPU, Leosphere and Heason engaged jointly to develop a long-range WindScanner, a scanning lidar based on the pulsed lidar Windcube 200 from Leosphere and a dual-axis mirror based steerable scanner head designed by DTU Wind Energy and IPU. Long-range WindScanners are intended for radial velocity measurements from the range of distances between 50 m and 8000 m, within a larger volume of the atmosphere. The current maximum measurement rate is 10 Hz. The maximum number of simultaneous radial velocities acquired at any rate along each LOS is 500. These measurements have a broad span of application ranging from wind energy (wind resource mapping, wind farm layout optimization, wind farm wake monitoring, etc.), airport safety (wind shear measurements, wake vortices measurements, etc.), to studies of the pollutants dispersion and meteorological studies. Table 1.1 summarizes main characteristics of the short-range and long-range WindScanners.

Figure 1.2: The short-range WindScanner (left) and the long-range WindScanner (right)

WindScanner	Short-Range	Long-Range
Laser type	Continuous wave	Pulsed
Range	10 - 200 m	25 - 8000 m
Maximum measurement rate	400 Hz	10 Hz
Simultaneous measurements	1	500
Dual axis scanner head	Double prism based	Triple or Dual mirror based
Mechanical rotation	Belt driven	Gear-box driven
Rotation	Endless	Endless
Atmospheric coverage	Cone with a full opening angle of 120°	Hemisphere
Maximum rotational speed	$2880°/s$	$50°/s$
Weight	120 kg	150 kg

Table 1.1: Specifications of the short-range and long-range WindScanners

The intention from the beginning of the long-range WindScanner development was to create a commercial product, which is available via Leosphere as a full-sky, beam-steerable wind profiler Windcube 200S since 2011 (Figure 1.3)[64, 65]. During 2011, two validation campaigns of Windcube 200S were performed at the airport Charles de Gaulle in Paris [66, 67]. Moreover, since mid 2011 one device is deployed at the Nice airport where it is used for the detection of harmful wind shears [68, 64].

Figure 1.3: The latest version of Windcube 200S, weight 232 kg

It should be noted that due to the differences in the requirements for research and industry (Table 1.2), the long-range WindScanner and Windcube

200S only have the same hardware components, drivers for the hardware components, fast Fourier transform (FFT) algorithm and Maximum-Likelihood estimator (MLE). The operational principles are different, as well as the software architecture. From Table 1.2, it can be seen that the operational principles of the long-range WindScanner and the software were intended to provide great flexibility in terms of the motion of the scanner head and configurability of the wind velocity measurements, while the operational principles of Windcube 200S restricted configurability of the lidar to fewer options. Also, the WindScanner software allows synchronization of the measurement process among multiple WindScanners, where for the Windcube 200S this is not possible. In order to achieve the synchronization, the WindScanner software was conceptualized as network-based, which is another characteristic that differentiate this software from the Windcube 200S software.

On the other hand the Windcube 200S software was conceptualized as commercial software, and the lidar itself was primarily intended for the airport safety applications. For these reasons, robustness was one of the main attributes, and due to this, a limited set of configurable parameters was desirable, since a larger set of configurable parameters used by an inexperienced user can produce fatal damages to rather expensive and sophisticated equipment.

	Windcube 200s	**Long-range WindScanner**
Motion of the scanner head	One axis at time	**Two axes at time**
Motion regulated by	Speed	**Speed and Time**
Possible speed	0.5, 1, 2, 3 and 4 $^\circ/s$	**Any speed up to 50**$^\circ/s$
Minimum move	0.5°	**0.001°**
Type of trajectory	LOS, DBS, PPI and RHI	**Arbitrary trajectories within the kinematic limits**
Minimum acquisition time of measurements	0.5 s	**0.1 s**
Maximum acquisition time of measurements	10 s	Unspecified
Acquisition time between two consecutive measurements	Fixed	**Flexible**
Minimum distance between two consecutive radial velocities retrieved along the same LOS	25 m	**0.6 m**
Maximum distance between two consecutive radial wind speeds retrieved along the same LOS	200 m	**Up to the maximum range**
Distances at which radial velocities are retrieved from one to another LOS	Fixed	**Flexible**
Synchronization with other lidars	Not possible	**Possible**
Type of software	Standalone	**Network-based**

Table 1.2: Requirements for Windcube 200S and long-range WindScanner from **2010**, details regarding the Windcube 200S originate from Leosphere's brochure 'Weather & Climate Lidar Products' published in 2011

Chapter 2

Engineering coherent Doppler scanning lidars

2.1 Introduction

In the literature investigated in the previous chapter, we could see that the great majority of the ground-based coherent Doppler scanning lidars have been used to perform measurements scenarios which consist of PPI or RHI scans. These measurement scenarios can be defined as simple, since a scanner head of a coherent Doppler scanning lidar, dedicated for the laser beam steering, rotates around a single axis of rotation with constant angular speed.

For PPI scans, the scanner head is rotated around the azimuth axis, while retaining constant elevation. During the rotation there is a continual emission of laser pulses and acquisition of the backscattered light. Usually, the emission and acquisition processes are initiated once the speed of the scanner head reaches the desired constant value. This is done in order to ensure a uniform distribution of the laser pulses per angular sector.

The same can be said for RHI scans, for which the scanner head is rotated around the elevation axis with a constant azimuth. Therefore, both RHI and PPI scans are speed controlled. Also, for both scans, distances at which the radial velocities are extracted along LOS are fixed from one angular sector to another.

The exceptions from PPI and RHI scans are step-stare scans, performed by Halo photonics lidars, in the wake characterization experiment. The Halo photonics software only allows setting the maximum LOS distance at which the radial velocity should be retrieved and submission of an ASCII-file that contains the set of the azimuth and elevation angles at which the LOS velocity measurements should be taken. There is no control over the execution of the step-stare trajectory or the measurement rate, nor for the distances at which the radial velocities should be retrieved, apart from the maximum one. Above all, the scanner head is rotated around one axis at a time.

Restricting a Doppler scanning lidar to perform measurement scenarios based on PPI, RHI and step-stare scans, simplifies the operational principles of the lidar and the architecture of the lidar software. This same restriction is valid for the commercial version of the long-range WindScanner, namely Windcube 200S. However, this restriction prohibits the time-space synchronization of Doppler scanning lidars. With measurement scenarios based on PPI scans, geometrically it is not feasible to intersect laser beams and to move the point of intersection over an area of interest. The same is true for the step-stare scans of the Halo photonics lidars. On the other hand, with measurement scenarios based on RHI scans, this is theoretically possible along vertical axes, but only if lidars are symmetrically arranged around them.

To further advance the measurement techniques of a single or multiple Doppler lidars, it is advisable to lessen the restrictions and allow more configurability of the measurement scenarios. This calls for novel operational principles and architecture of the software.

In this chapter, we will present the operational principles and architecture of the software that allow non-restrictive time-space synchronization of coherent Doppler scanning lidars on the example of a long-range WindScanner. These operation principles and architecture of the software consist of the following aspects:

- Synchronization among the laser pulse emission, acquisition of the backscattered light and steering of the laser pulses
- Accurate time control of the emission, acquisition and steering
- Arbitrary trajectories of the scanner head
- Flexible acquisition time of LOS measurements
- Flexible distribution of the distances at which radial velocity is retrieved from LOS measurement

Since the current literature does not encompass discussions on the operational principles and architecture of the software that include any of the above mentioned aspects, the operational principles and architecture to be explained in this chapter represent a novelty and as such, a contribution to knowledge.

In addition to the discussion about the operational principles and architecture of the software, an end-to-end measurement process of the long-range WindScanner will be explained. This discussion includes a detailed description of the key hardware components of the long-range WindScanner and the background theory that governs the measurement process of coherent Doppler lidars.

2.2 Operational principles

A coherent pulsed Doppler scanning lidar performs four fundamental processes that enable measurements of radial velocity:

- Emission of laser pulses
- Steering of laser pulses into the atmosphere by rotation of the scanner head
- Acquisition of the backscattered light
- Analysis of the acquired backscattered light

All these processes have to be closely coordinated. In order to achieve seamless integration and coordination of the fundamental processes, the long-range WindScanner operational principles consist of the centralization of the control of emission, steering and acquisition in a single hardware component, namely the motion controller, and strict time control over these processes. This is achieved by equating the process of the emission and acquisition to the process of rotation of the shaft of a phantom stepper motor.

An incremental move (i.e. step) of the stepper motor shaft is produced each time when the motor receives a voltage pulse, hereinafter referred to as a trigger. The motion controller has the role of sending the triggers. By controlling the number of sent triggers, the motor will perform different angular moves. From the control perspective if there is no load on the shaft there is no need for position readings of the shaft and closure of the feedback loop, thus the control of the stepper motor can be simplified to an open loop control (i.e. feedforward control).

Similarly, the hardware components responsible for the emission and acquisition are optimized to send the laser pulse and acquire the backscattered light, respectively, each time they receive a trigger. The processes of the emission and acquisition occur simultaneously, and thus can be 'modeled' as the rotation of a single stepper motor. From the control perspective this represents the rotation of zero load around one axis, which we will call a phantom axis. The configuration of the trigger rate and trigger number permits accurate time control of the emission and acquisition. After the end of each acquisition of the backscattered light, the acquired signal is forwarded to the lidar computer that performs the analysis of the acquired signal.

The motion controller of the long-range WindScanner is Delta Tau TURBO PMAC, a multi-axis controller, which can simultaneously control up to 32 servo or stepper motor axes. In case of the long-range WindScanner, besides the phantom axis, the motion controller controls two real servo motors that rotate the scanner head around the azimuth and elevation axes.

Therefore, the motion controller simultaneously controls three axes, two real and one phantom. In this way the problem of attaining close coordination among the fundamental processes is solved by transforming the non-motion processes into motion processes, and controlling all processes from a single hardware component.

2.3 End-to-end measurement process

2.3.1 Introduction

In this section, the previously described operation principles will be placed in the function of the radial velocity measurements of a pulsed coherent Doppler scanning lidar. Where appropriate, the long-range WindScanner will be used as an example.

2.3.2 Emission

A measurement process starts with the emission of the laser pulses. Each emitted laser pulse has a characteristic Gaussian shape with a certain temporal length T_{pulse}, energy content E and wavelength λ (Figure 2.1,a). Laser pulses are usually emitted in bursts that last continuously over some period of time (Figure 2.1,b). The emission frequency is constant and is known as the pulse repetition frequency (PRF).

In the case of the long-range WindScanner, there are two different laser pulse types, the Long and the Middle pulse, and two corresponding PRFs (Table 2.1). The Long pulses contain more energy than the Middle pulses, and due to the two times larger temporal length the aerosols particles at any distance are exposed to the laser light for a longer period. This results in higher carrier-to-noise ratio (CNR), which directly influences the maximum distance from which the radial velocity can be retrieved. The drawback of the Long pulses is that the retrieved radial velocity is characterized by the two times larger range resolution than in the case of the Middle pulses, which means that eddies smaller than the range resolution are filtered out. Typically the Long pulses are used to retrieve the radial velocity from distances of up to 8 kilometers. On the other hand, the Middle pulses are suitable for the retrieval of radial velocity from distances of up to 4 kilometers with the half range resolution of the Long pulse.

Type	Wavelength [nm]	Temporal length [ns]	Shape	Energy [μJ]	PRF [kHz]
Long	1543	400	Leosphere 400	100	10
Middle	1543	200	Leosphere 200	50	20

Table 2.1: Type of laser pulses

In the case of the long-range WindScanner, prior to the emission of the laser pulses, the hardware components that drive the process of the emission are configured. The motion controller receives the number of laser pulses that will be emitted and the value of the pulse repetition frequency. The pulse generator receives the shape and temporal length of the pulse, and the Erbium-doped fiber amplifiers (EDFA) receives information about the energy content of each laser pulse (Figure 2.2). After the completion of the hardware configuration, the CW

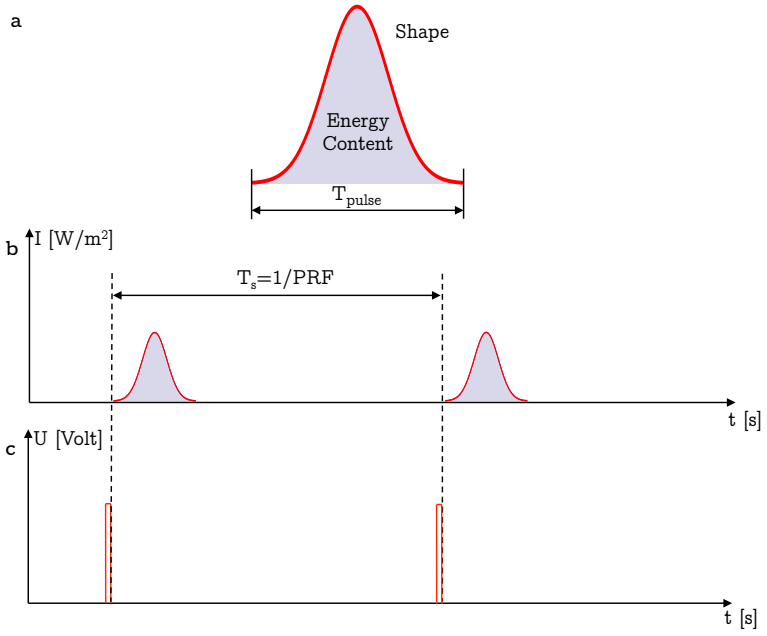

Figure 2.1: Emission: a - laser pulse, b - pulse train, c - trigger signal

laser starts the generation of the monochromatic low-energy laser light with the frequency f_{cw}.

The emission process begins with the start of the trigger signal (Figure 2.1, c). Each time the pulse generator receives a trigger, it sends an analog signal of the pulse shape and a copy of the trigger to the acousto-optic modulator (AOM) (Figure 2.2). Based on these two input signals and the low-energy laser light from the CW laser, the AOM forms a low-energy laser pulse. In comparison to the original CW light, the laser pulse frequency is shifted to $f_0 = f_{cw} + f_{AOM}$, where the AOM frequency is equal to 68 MHz. The shift in the frequency allows determining the retrieved radial velocity sign.

Once the low-energy laser pulse is formed, it is directed to the EDFA, which increases the energy content of the pulse. This forms the high-energy laser pulse. After the EDFA, the high-energy laser pulse passes through the optical circulator and telescope (Figure 2.2). The optical circulator has the role to separate directions of the outgoing laser pulses and the incoming backscattered light. By using the optical circulator, the transmitter of the laser pulses and the receiver of the backscattered light can both use the same optical path. The telescope is used to magnify the laser beam and to focus the beam at a certain distance. The magnification reduces the beam divergence in the far field, while the focusing is used to optimize the distribution of the laser beam power along the distance. The process of steering starts once the laser pulse enters the scanner head.

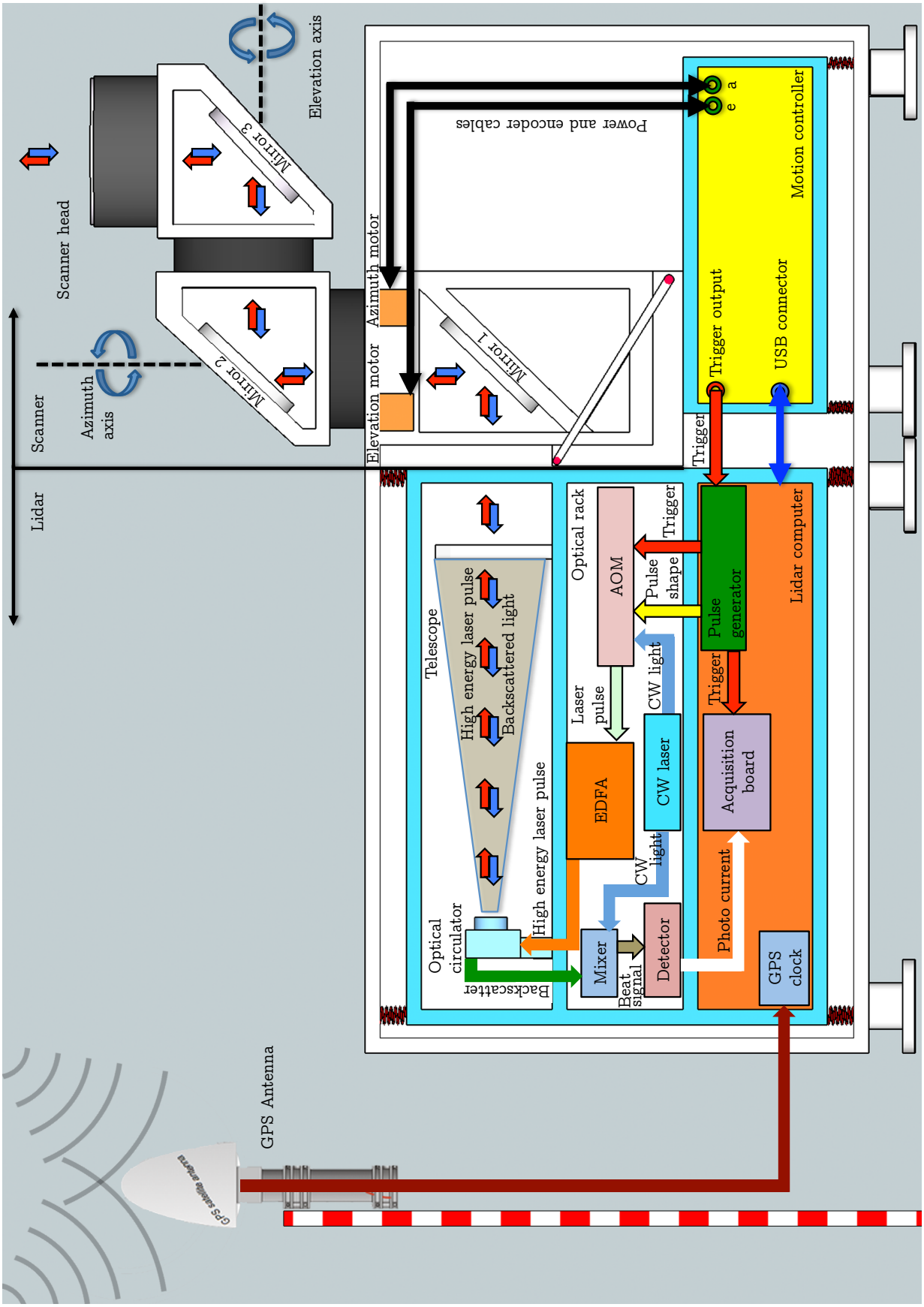

Figure 2.2: Schematics of the long-range WindScanner

2.3.3 Steering

The laser pulses are either steered by means of moving prisms or mirrors. Typically the former is used for CW scanning lidars, and the latter for pulsed scanning lidars.

In the case of the long-range WindScanner the steering is done using the scanner head that consists of three mirrors (Figure 2.2). The first mirror is connected to the fixed part of the scanner head (the base of the scanner head), while the remaining two mirrors are connected to the moving parts of the scanner head. The scanner head has two rotational degrees of freedom and can rotate around the azimuth and/or elevation axes, thus it directs the laser pulses into the atmosphere at any combination of azimuth and elevation. These two axes are perpendicular to each other.

The rotation is achieved by two brushless servo motors that each drive a gear box (Figure 2.3, a). Each motor has a worm coupled to the shaft (Figure 2.3, b). In order to avoid slip-rings, bevel gears are used to transmit the rotation of the elevation motor to the rotation around the elevation axis of the scanner head (Figure 2.3, c). A consequence of this is a kinematic coupling between the elevation and azimuth axis. Because of the coupling, in order to only move the scanner head around the azimuth axis, it is necessary to rotate both motors, though in opposite directions (Figure 2.3, d).

The rotation of the scanner head is controlled by the feedback and feedforward control of the motion controller. The position information, necessary for the correct functioning of the feedback loop, is acquired using the rotary encoders attached to the motors' shafts. The resolution of these sensors is $0.0001°$, where this at the same time represents the minimum commandable move. The maximum scanner head rotation speed is $50°/s$, while the maximum acceleration is $100°/s^2$. The scanner head can rotate around both axes from $0°$ to $360°$, and the rotation can be endless.

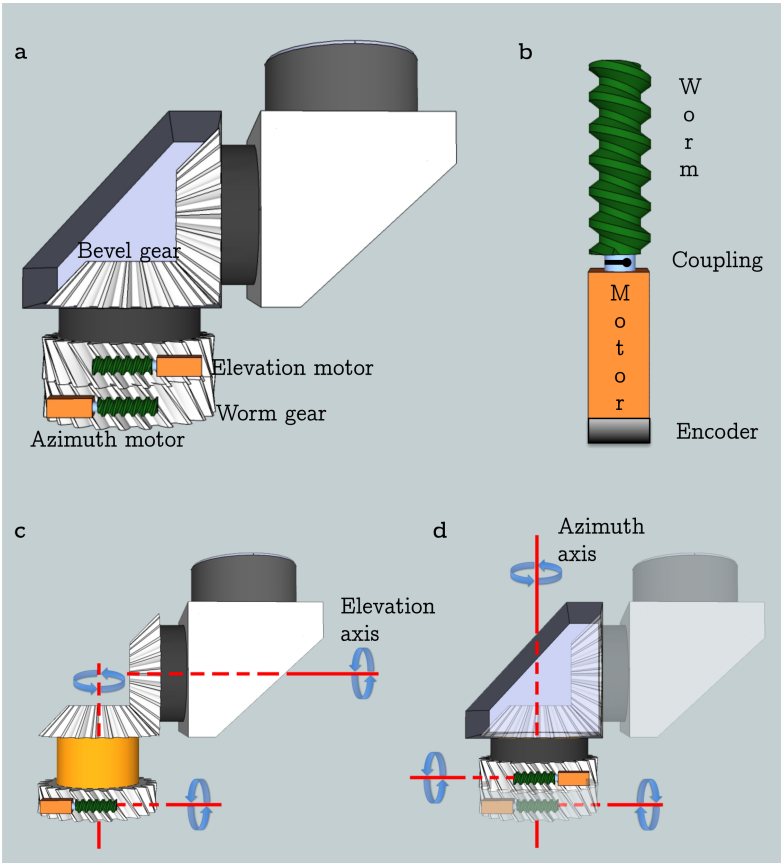

Figure 2.3: a - mechanical design concept, b - motor with the coupled worm, c - rotation about the elevation axis, and d - rotation about the azimuth axis

2.3.4 Acquisition

As the laser pulse propagates through the atmosphere, along a direction given by the azimuth and elevation angles of the scanner head, it interacts with dispersed moving aerosol particles in the atmosphere. As it has been mentioned in Chapter 1, it is assumed that the particles velocities are equal to the wind velocity.

Due to the optical Doppler effect, the particles perceive the incoming laser pulse light with slightly shifted frequency $f_{perceived}$, where the difference in frequency corresponds to the velocity of the particles projected on the laser pulse propagation path, i.e. radial or LOS velocity. The relation between the perceived frequency and radial velocity is given with the following equation:

$$f_{perceived} = f_0 + f_0 \frac{V_{radial}}{c} = f_0(1 + \frac{V_{radial}}{c}) \tag{2.1}$$

where, f_0 is the frequency of the laser pulse, c is the speed of light, and

V_{radial} is the radial speed or the projected speed of the particles on the laser pulse propagation path (i.e. LOS).

In the interaction between the particles and laser pulse, a small portion of the laser pulse light is reflected from the moving particles back to the lidar (Figure 2.4). Because of the movement of the particles, the backscattered light has the original frequency f_0 shifted by twice the radial velocity divided by the speed of light:

$$f_{bslight} = f_0(1 + 2\frac{V_{radial}}{c}) = f_0 + \Delta f \tag{2.2}$$

where, $f_{bslight}$ is the frequency of the backscattered light, and term Δf represents the frequency shift commonly known as the Doppler shift. The sign of the Doppler shift will be positive if the particles are moving towards the lidar and negative if the particles are moving away from the lidar.

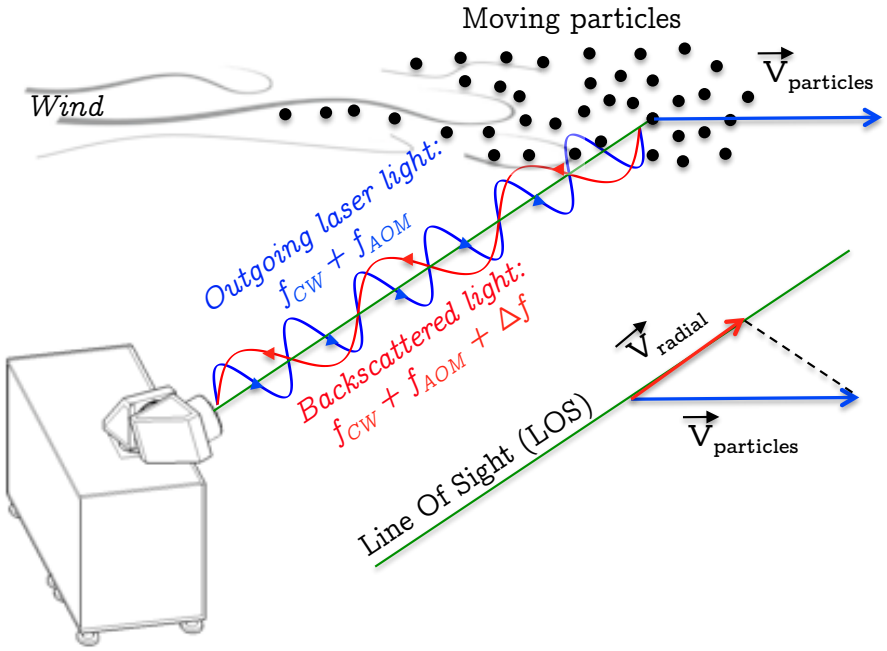

Figure 2.4: Doppler effect

Due to the laser pulse's propagation through the atmosphere, the lidar, in this case WindScanner, continuously receives the backscattered light from different distances and thus the information about the radial velocity. Using the range gating technique, discrimination between distances is achieved by using the backscattered light's time of arrival in relation to the start of the laser pulse.

Once the backscattered light reaches the WindScanner, it follows the path of the outgoing laser pulses (Figure 2.2). It reflects on the mirrors, and it passes

through the telescope after which it enters the optical circulator. Through the system of optical fibers, the backscattered light is directed towards the optical mixer, where it is optically mixed with the copy of the low-energy CW laser light, known as the local oscillator (LO) beam. The mixing of two light signals leads to the 'beat' phenomenon, in which the amplitude of the resulting light oscillates at the frequency difference between two light signals. This beating light signal is focused on the photodetector that transforms the light signal into an analog signal that follows the oscillation of the light intensity. For the analog signal we will use the description given in [69]:

$$\begin{aligned} i_s(t) \propto (E_{LO}\cos(2\pi f_{cw}t) + E_s\cos(2\pi(f_{cw}+f_{AOM}+\Delta f)t))^2 = \\ = (E_{LO}^2\cos(2\pi f_{cw}t)^2 + E_s^2\cos(2\pi(f_{cw}+f_{AOM}+\Delta f)t)^2) + \\ +2E_{LO}E_s cos(2\pi(f_{AOM}+\Delta f)t) \approx \\ E_{LO}^2 + E_s^2 + 2E_{LO}E_s cos(2\pi(f_{AOM}+\Delta f)t) \end{aligned} \tag{2.3}$$

where E_{LO} and E_s are a LO field and backscattered light field respectively. The reason why the previous relation is reduced to the constant term, representing the LO and backscattered light beam, and oscillating term, which includes the Doppler shift and AOM frequency, is due to the fact that the photodetector can only follow the fluctuations of the net field up to GHz range.

The signal $i_s(t)$ is digitized by the acquisition board at a sampling rate of f_s=250 MHz, which defines the sampling period of T_s=4 ns. The acquisition of the photodetector output occurs each time the acquisition board receives a trigger from the motion controller (Figure 2.5). The number of sample points of the digitized signal determines the maximum distance at which the radial velocity will be retrieved.

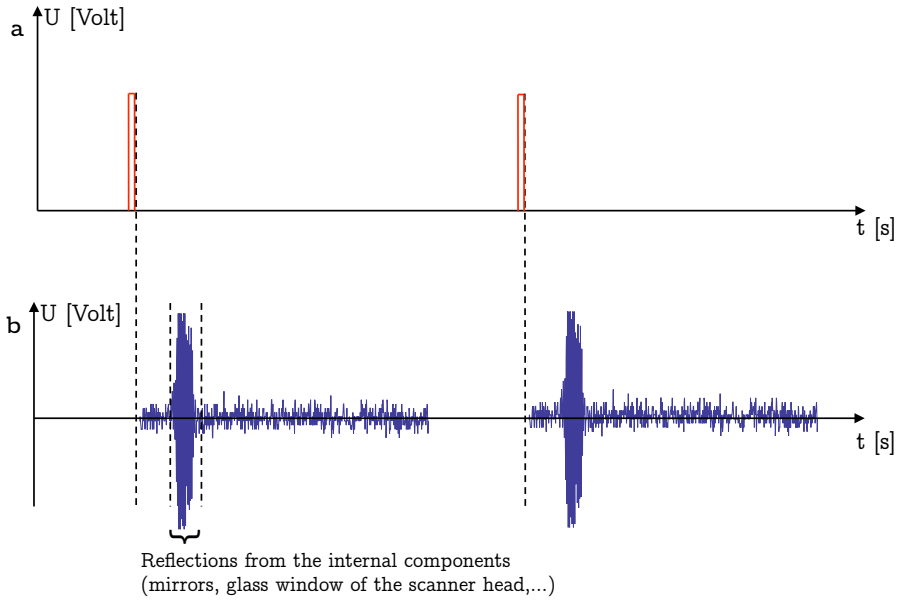

Figure 2.5: a - trigger signal, b - acquired analog signal

2.3.5 Analysis

The radial velocity at a distance d can be retrieved from the return of a single laser pulse by the estimation of the mean Doppler shift Δf from M sample points of the corresponding digitized output of the photodetector. These M sample points define the observation time $T_{FFT}(s) = MT_s$, and they include the information regarding the backscattered light that originates from a range of distances [d-$\Delta d/2$,d+$\Delta d/2$] centered at the distance d (Figure 2.6).

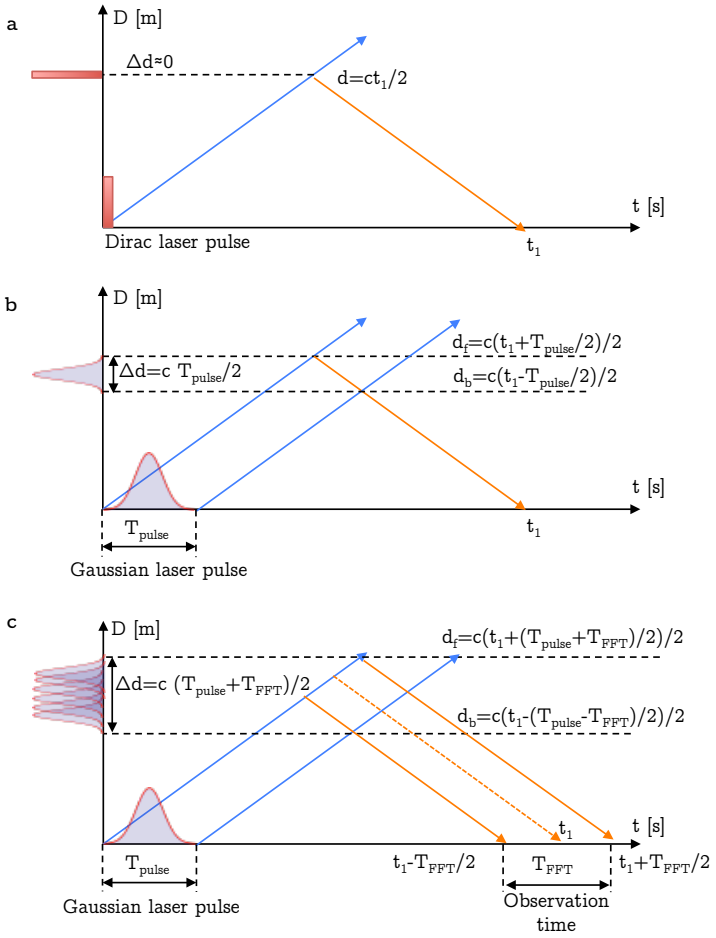

Figure 2.6: Retrival of the radial velocity: a - one sample point of the Dirac return, b - one sample point of the Gaussian return, c - M sample points of the Gaussian return

If the finite discrete signal, given with M sample points, is transformed to the frequency domain, and spectrum of the transformed signal calculated, then by applying a frequency estimator on the spectrum, such as an MLE, the frequency of the spectral peak can be estimated. Subtracting the AOM frequency f_{AOM} from the estimated frequency yields the mean Doppler shift Δf of the backscattered light from the range of distance [d-$\Delta d/2$,d+$\Delta d/2$] centered at the distance d. Along with the Doppler shift, the MLE estimates the spectral broadening and CNR from the signal spectrum.

In order to express the signal of M sample points in terms of the spectrum, the observation time T_{FFT} should be larger than the backscattered light correlation time τ, which can be approximated as the temporal length of the emitted laser pulse T_{pulse} [70]. The narrower the spectrum is, the more sample points are used to derive the spectrum. This results in the improved velocity resolution, since each frequency bin in the spectrum will be defined on the smaller frequency range. The consequence of this is an increase in the range resolution, since more sample points mean bigger range of distance [d-$\Delta d/2$,d+$\Delta d/2$] from which the backscattered light is acquired and analyzed. Due to the tradeoff between the velocity and range resolution, the observation time T_{FFT} is usually set to the temporal length of the emitted laser pulse T_{pulse}, which provides one independent retrieval of the radial velocity per observation time.

The retrieval of the radial velocity from a single laser pulse return encompasses the random error that originates from the uncorrelated noise [71], which leads to the incorrect estimate of the spectral peak. As an alternative, the estimation of the mean Doppler shift Δf from N accumulations of the laser pulse returns leads to the suppression of the random error and improvement of the Doppler shift estimation accuracy [72]. In this method, the frequency estimator is applied on the averaged sum of N spectra (Figure 2.7). It has been shown in [70] that the number of accumulations N of the order of 10 is useful for eliminating the incorrect estimates of the radial velocity at low CNR. The accuracy of the Doppler shift estimate can be calculated without a priori knowledge of the wind velocity field using the expression given in [72] :

$$\Delta V_r \approx \frac{0.2\frac{\lambda}{2T_s}}{N^{1/2}CNR}\left(\left(\frac{T_s}{T_{pulse}}\right)^{1/3}\left(\frac{1}{M}\right)\right)^{1/2}\left(1+1.42\frac{T_{pulse}CNR}{T_s}\right) \quad (2.4)$$

The accumulation method has been applied for the long-range WindScanner retrieval of radial velocities. The FFT algorithm used to transform the acquired signal to the frequency domain is adopted by Leosphere to work only with the number of sample points M given as a power-of-two. Consequently, the corresponding minimum observation time T_{FFT} for the Middle and Long laser pulses is 256 and 512 ns respectively. In other words, the minimum FFT size is 64 points for the Middle pulses, and 128 points for the Long pulses.

The time interval for the accumulation cannot be lower than 100 ms, since the WindScanner client software (WCS) is developed to process the acquired backscattered light in real-time. This results in the minimum number of accu-

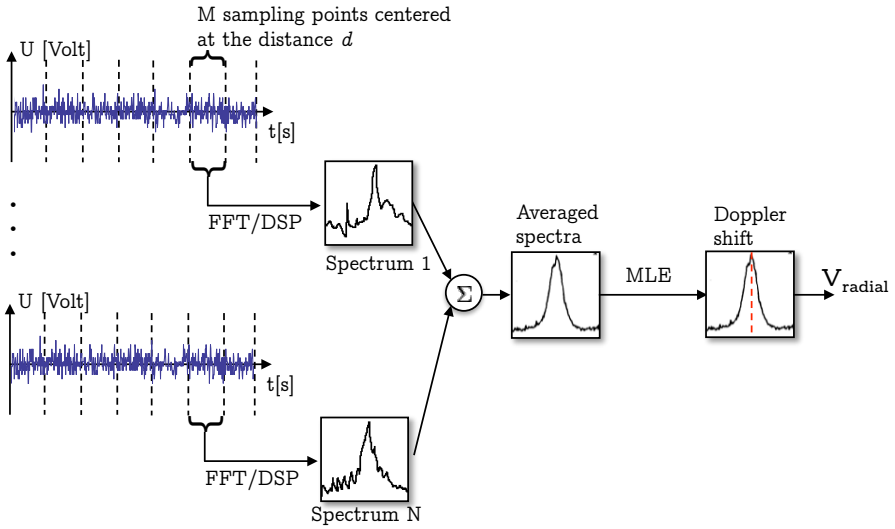

Figure 2.7: Accumulation method

mulations N of 2000 and 1000 for the Middle and Long laser pulses respectively, and thus the maximum measurement rate of 10 Hz. The frequency estimator applied on the averaged spectra is the MLE developed by Leosphere. The MLE is Leosphere's proprietary "blackbox" in the long-range WindScanner.

2.4 Architecture of WindScanner client software

2.4.1 Introduction

The previously described operational principles and end-to-end measurement process are handled by the WCS, which is installed on the lidar computer. It is developed in LabView, and run on a Windows platform. The WCS is a network-based application, which is remote controlled by the software that resides in the master computer. The WCS provides a broad range of tunable parameters, which offer users flexibility to design measurement campaigns with the long-range WindScanners. In the following sections of this chapter details regarding the WCS will be explained.

2.4.2 Main loop of the software

At the start of the software initial checks are done, the log file recorded, connection with all physically present devices in the WindScanner made, together with the connection to the distant master computer (Figure 2.8). Before the retrieval of the radial velocities starts, the WCS initializes WindScanner's devices such as the EDFA, motion controller, etc. (Figure 2.9). Afterwards, the software

waits for the list of measurement scenarios from the master computer. In case of a long-range WindScanner measurement scenarios define the scanner head movement, emission of laser pulses, backscattered light acquisition, acquired backscattered light analysis. Therefore, the measurement scenario completely describe the WindScanner measurement process. Each long-range WindScanner measurement scenario consists of the following information:

- Positions of the scanner head in azimuth and elevation in respect to time (i.e. trajectory)
- How many pulses should be emitted at certain azimuth and elevation angles (i.e. LOS measurements)
- What type of laser pulses should be emitted and at what pulse repetition frequency
- What is the maximum distance at which the radial velocity is retrieved
- What FFT size should be used to convert backscatter signal into the signal spectrum
- How many accumulations of the laser pulse returns should be used per Doppler shift estimate (i.e. number of accumulations N)
- At what distances the Doppler shift, and thus radial velocity, should be retrieved along each LOS
- How many iterations same scenarios will have (N_S)

Once the list of scenarios is received and a command from the master computer sent to start the execution of the scenarios, the WCS reads the first scenario and configures the devices accordingly.

All the information regarding the measurement scenario is provided within two files. One file is named 'motion program' and the other 'range gate file'. These files are either manually made and then uploaded to the WCS, or are generated on the basis of user's input parameters by a sub-program that runs in the WCS.

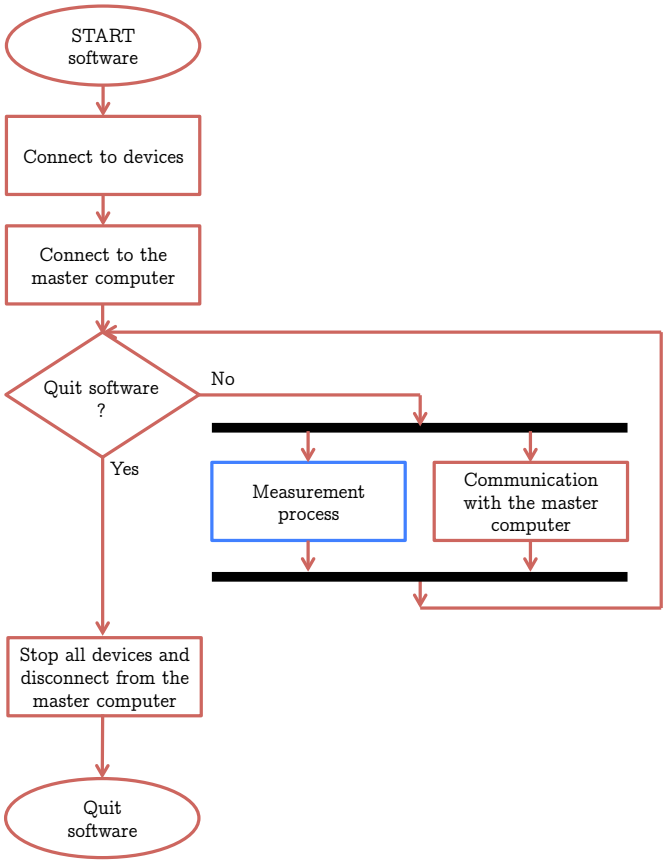

Figure 2.8: The flow diagram of the main loop of WCS

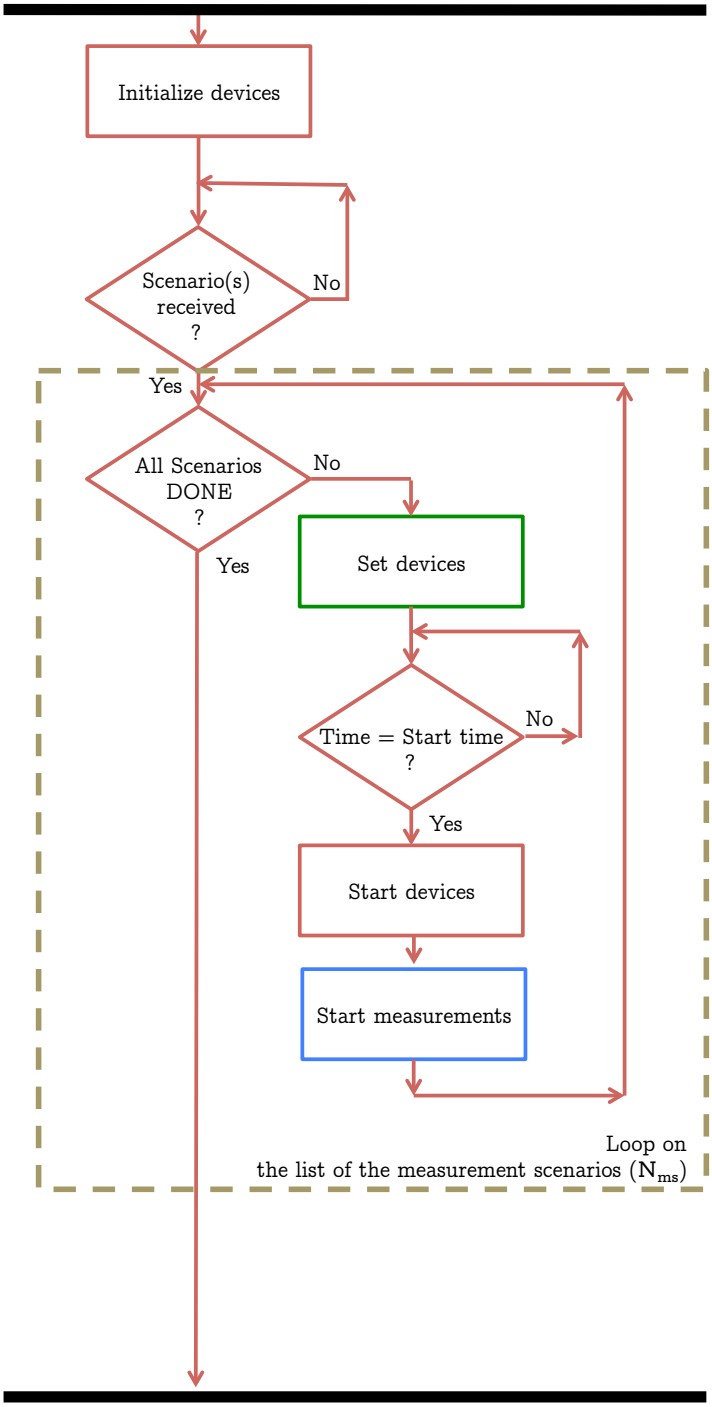

Figure 2.9: The flow diagram of the loop which governs the measurement process, the number of iterations of the loop is equal to the number of received scenarios (N_{ms})

2.4.3 Motion programs

In the case of the long-range WindScanner, motion programs represent the motion controller's mechanism for describing the desired trajectory of the scanner head with the associated distribution of the triggers. As previously mentioned, the triggers represent voltage pulses that are sent from the motion controller to the hardware components responsible for the emission and acquisition. Since the triggers result in the emission of the laser pulses and acquisition of the backscattered light, this distribution corresponds to the desired positions of the scanner head at which the measurements will take place.

Turbo PMAC's motion program language is used to write motion programs. The program language represents a cross between a high-level computer language like BASIC or Pascal, and G-Code (RS-274) machine tool language. In fact, the motion program can be written directly in G-Code. Numerical values in the program can be specified as constants or expressions.

The standard form of a motion program used for the long-range WindScanner applications is shown in Table 2.2. In the initial part of the motion program the coordinate system is set, where the positions of motor 1 and 2 describe the rotation around the azimuth and elevation axis of the scanner head, and the position of motor 3 (i.e. phantom motor) corresponds to the number of sent triggers, which drive the emission of the laser pulses and acquisition of the backscattered light.

Usually, the motion program starts from the initial position of the scanner head, which corresponds to the start of the measurements. Also, at this part of the motion program, the position of the motor 3 is zeroed. Once the scanner head is set to the initial position, the motion program enters the loop over the trajectory with the associated distribution of the triggers, during which the measurements occur.

The loop can consist of parts which describe:

- Rotation around one or two axes at a time
- Fixed position of the scanner head during which the certain number of triggers are transmitted at a constant frequency which corresponds to the PRF
- Rotation around one or two axes at a time during which the triggers are also transmitted

In order to have time control over the steering of the laser pulses, each movement of the scanner head and transmission of triggers is performed during the precise time set by the user (Table 2.2). The source for precise timing of moves and transmission is the motion controller crystal clock oscillator, which has a frequency of 20 MHz with the accuracy of $\pm$ 50 parts per million (PPM).

With the above described features, the motion program provides means to:

- Perform any type of trajectory within the kinematic limits

- Precisely distribute a number of triggers in respect to the scanner head positions
- Accurately control time that the emission of the laser pulses, their steering, and acquisition of their backscatter light will take
- Elegantly solve the synchronization of these fundamental lidar processes

1 − > A	; Assign motor 1 to the Azimuth axis
2 − > E - A	; Assign motor 2 to the Elevation and Azimuth axis
	; with opposite signs in order to compensate
	; for the kinematic coupling
3 − > T	; Assign phantom motor 3 to the Trigger axis
$N_s = 100$	; Number of iterations of the same scenario
TM10000	; 10000 ms move time to the azimuth
A(20)E(5)	; position equal to 20° and elevation to 5°
M361=0	; Reset motor 3 position
WHILE($N_s \geq 0$)	; Loop on the number of iterations
$N_s = N_s$ - 1	; Decrement counter
TM1000	; 1000 ms move time to the azimuth
A(20)E(5)	; position equal to 20° and elevation to 5°
TM1000	; 1000 ms stand still and execution of
T(10000)	; 10000 triggers, which corresponds to PRF=10 kHz
TM800	; 800 ms move time to the azimuth
A(30)	; position equal to 30°
T(M361+8000)	; while executing 8000 triggers (PRF=10 kHz)
TM2000	; 2000 ms move time to the azimuth
A(60)E(30)	; position equal to 60° and elevation to 30°
T(M361+20000)	; while executing 20000 triggers (PRF=10 kHz)
M361=0	; Reset motor 3 position
ENDWHILE	

Table 2.2: Motion program

2.4.4 Range gate files

In order to complete the description of the measurement scenario, the range gate file comprises the following information:

- The type of the laser pulse (temporal length, shape, and energy content)
- Maximum distance for the retrieval of the radial velocity
- FFT size
- Number of accumulations per LOS measurement
- Distances at which radial velocities will be retrieved along each LOS measurement

All this information is written in comma-separated values (CSV) text file. One example of the range gate file is given in Table 2.3.

It is important that the range gate file matches the motion program in order to correctly configure hardware components and processes. For manually made measurement scenarios this responsibility lies with the user, while for the automatic generated measurement scenarios a dedicated sub-program performs the checking procedure. The given example of the range gate file matches the motion program from Table 2.2. Since the trigger frequency in the motion program is equal to 10 kHz, the appropriate pulse type in the range gate file is set to Long, and the FFT size to 128 points (see Table 2.1). The maximum distance is a free parameter, and for this range gate file it is set to 5000 m.

Finally, there is information about the acquisition and analysis process for each LOS measurement. Once again the number of LOS measurements coincides with the three parts of the motion program during which the transmission of the triggers occurs. The number of accumulations matches the number of triggers for each of these three parts.

The number of distances at which the radial velocity is retrieved for each LOS measurement is a free parameter. The smallest number is one and largest 500, which is the processing limit of the acquisition board. The number of distances can differ from one LOS measurement to another. They can also be set randomly.

Pulse type	Middle		
FFT size	128		
Maximum distance	5000		
Measurement point	Number of accumulations (N_A)	Distance 1	Distance 2
1	10000	1100	
2	8000	300	241
3	20000	4000	

Table 2.3: Range gate file

2.4.5 Automatic generation of scenarios files

The automatic generation of scenario files was made to save time, avoid mistakes in coding of motion programs and writing range gate files, as well as to ensure that motion programs and range gate files are aligned with each other. Currently, the automatic generation of the motion programs and range gate files covers following measurement scenarios: LOS, PPI, RHI, DBS and step-stare. The step-stare scenarios are named here as 'Complex Trajectory Discontinuous' (CTD), due to the discontinuous motion of the scanner head.

LOS is the simplest measurement scenario and it represents the measurement of the radial velocity along one beam direction. Therefore, the scanner head position is fixed and the laser pulses are sent to the atmosphere.

During the execution of the PPI scenario, the elevation angle of the scanner head is kept constant while the azimuth angle varies, with the constant speed being accompanied by constant emission of the laser pulses into the atmosphere. The measured radial velocity can then be mapped on a horizontal plane. PPI scenarios can either cover a range of azimuth angles smaller than 360° (this is known as a "sector scan") or the scanner head can endlessly rotate around the azimuth axis (this is known as a "surveillance scan").

The RHI scenario is somewhat similar to the PPI. In this case, the azimuth angle of the scanner head is kept constant while the elevation angle varies, with the constant speed being accompanied by constant emission of the laser pulses into the atmosphere. RHI scenarios are always sector scans. The measured radial velocity can be mapped on a vertical plane.

The DBS contains LOS measurements along 4 or 5 beam directions. In case of a DBS scenario with 4 beam directions, the elevation angle is kept constant (usually around 60°) for each direction, while the azimuth angle differs from one direction to another by 90°. For a DBS scenario with 5 beams, one extra LOS measurement is performed along the vertical axis (elevation angle equal to 90°). A DBS scenario is used for vertical profiling of the wind velocity.

The CTD consists of a certain number of user configurable beam directions, along which radial velocity measurements are taken with the configurable motion time from one beam direction to another, accumulation time, etc.

The automatic creation of the scenarios is done by a sub-program called TeslaBlackBox that has been developed by the author of this thesis, and it represents DTU Wind Energy's proprietary "blackbox". The input parameters to this sub program are given in Table 2.4 and Table 2.5. These parameters are sent from the master computer when forming a list of measurement scenarios.

Scenario type	LOS	PPI	RHI	DBS	CTD
Number of iterations N_s	√	√	√	√	√
Start azimuth	√	√	√		
Stop azimuth		√			
Start elevation	√	√	√	√	
Stop elevation			√		
Number of beams				√	
Rotational speed	√	√	√	√	
Or time to move	√	√	√	√	
Number of triggers/accumulation N per LOS measurement	√	√	√	√	
Pulse type	√	√	√	√	√
Maximum distance	√	√	√	√	√
FFT size	√	√	√	√	√
Distances along LOS measurement	√	√	√	√	√
CTD Array					√

Table 2.4: Input parameters of TeslaBlackBox, ticks √ correspond to the parameters that are the inputs necessary in order for TeslaBlackBox to generate a scenario

MP No.	Time to move	Azimuth	Elevation	Triggers
1	1000	20	15	10000
2	1000	40	35	5000
...	...	...	...	...
N	2000	160	95	10000

Table 2.5: An example of CTD Array

2.4.6 Acquisition and analysis

Following the configuration of the WindScanner devices, based on the desired measurement scenario, the software waits for the current time to be equal to the desired start time (Figure 2.9). The current time is provided by the WindScanner GPS clock, which has an accuracy of 250 ns. Once the current time coincides with the desired time, the WCS starts the measurement process. During the measurements, the WCS simultaneously runs the acquisition of the backscattered light, analysis of the backscattered light and storing of the information about the wind velocity, scanner head and system state (Figure 2.10).

The acquisition loop is configured with the range gate file. Each time the acquisition occurs, the acquired time signal is read and cut into slices that correspond to the distances described by the range gate file for the current LOS measurement. These 'slices', which contain a certain number of sample points, are further sent to the FFT algorithm that calculates spectra. Each new spectrum is added to the existing accumulated spectra and once all the

accumulations are done for the current LOS measurement, the acquisition loop sets Acquisition Flag to true and it starts the acquisition of the backscattered signal for the following LOS measurement(Figure 2.11).

Acquisition Flag set to true starts the analysis loop. This loop averages the sum of spectra and sends the averaged spectra to the MLE, which extracts radial velocity information (Figure 2.11). During the analysis, the acquisition loop runs in parallel with the acquisition of the new LOS measurement.

Since the acquisition board has a double buffer for the acquisition of the backscatter signal, during the execution of the acquisition loop there is no loss of data.

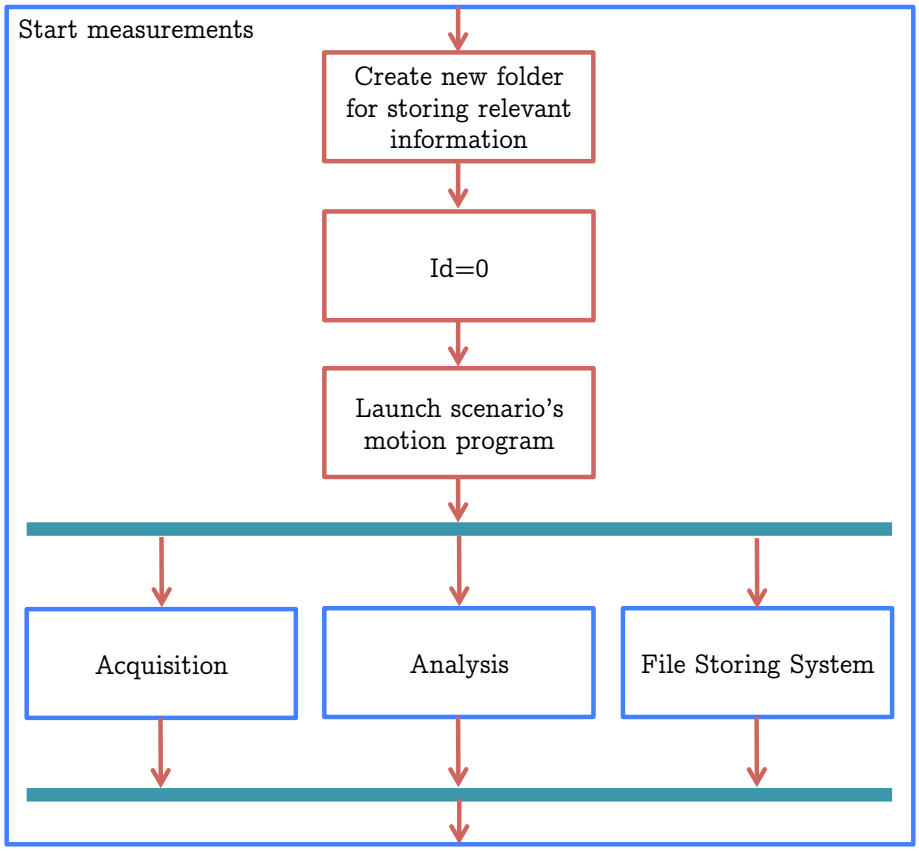

Figure 2.10: The flow diagram of the subloop that governs the measurement process and storing of relevant data

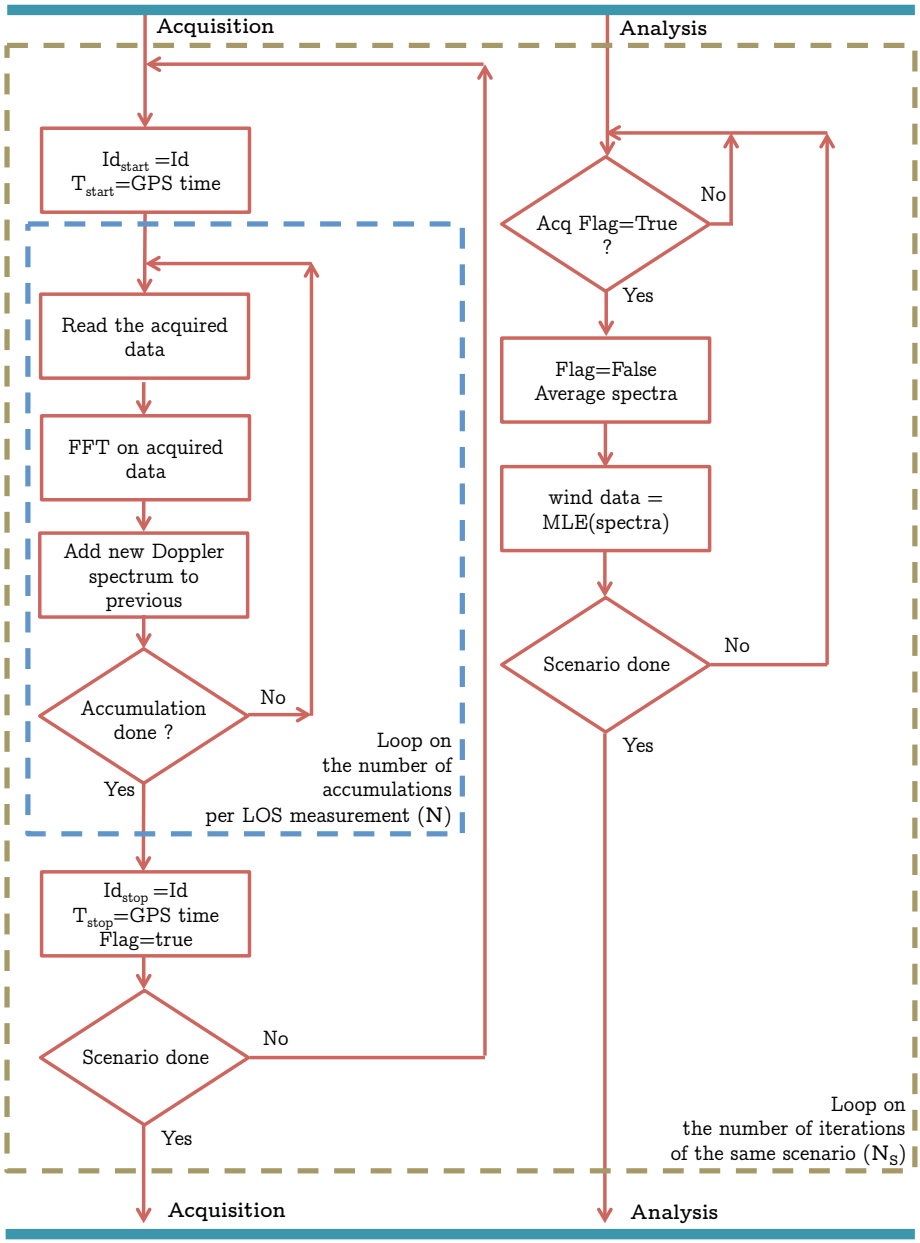

Figure 2.11: The flow diagram of the acquisition and analysis subloop

2.4.7 File storing system

During the execution of the measurement scenario, the WCS stores numerous information on the WindScanner mass storage. This information is organized in the scanner, wind and system file, which structure reflects underlying database structure. The scanner files contain values of the motors positions. The wind files contain retrieved radial velocity, CNR and spectral broadening for all distances of each LOS measurement. Apart from these two files which are linked to the measurement process itself, the system file holds system state information such as the GPS position, orientation, leveling and temperature of the WindScanner. All three files are interconnected, yet the information which they contain is written with different sampling rate. The link between these files is achieved using a primary key that is stored in the first column (scanner and system file) or in the first two columns (wind file) of the files.

This primary key is the variable Id, which evolves in the loop of the file storing system that appends this value together with the values of the motors positions to the scanner file (Figure 2.12). Each row of this file is written every 10 ms, and Id is incremented with this rate. Since the system states, such as temperature, do not change as fast as the motor positions, their values are written to the system file about every 1000 ms. These values are written together with Id_{system} which takes the value of Id at the time of appending a new row to the file (Figure 2.12).

At the beginning and the end of the accumulation, for each LOS measurement the current values of Id are stored in the variables Id_{start} and Id_{stop} (Figure 2.11). Also, the GPS time is saved in the variables T_{start} and T_{stop} at the same moment (Figure 2.11). After the MLE extracts information about the radial velocity for each distance of the current LOS measurement, it forwards the information to the file storing system that stores this information together with the values Id_{start}, Id_{stop}, T_{start} and T_{stop} to the wind file (Figure 2.12). In this way, all retrieved radial velocities can be directly related to both time and motor positions, and consequently, space.

The scanner, system and wind files are updated during a 10 minute period, after which the new set of files is made and updated during the next 10 minute period. The files are stored in the folder, the name of which corresponds to the name of the measurement scenario and date of the scenario execution. Once the scenario is completed, all the files from the corresponding scenario folder are uploaded to a remote database.

The file storing system allows an accurate reconstruction of the scanner head positions and system states during the accumulation of the backscatter signal for each LOS measurement of a measurement scenario. This is simply achieved by extracting the motors' positions from the scanner files that are in the range of Id values between the values of Id_{start} and Id_{stop} of any LOS measurement. The same holds for the case of the system file. This is illustrated in the examples of the scanner, system and wind files given in Table 2.6 that are related to the measurement scenario described in Table 2.2 and Table 2.3.

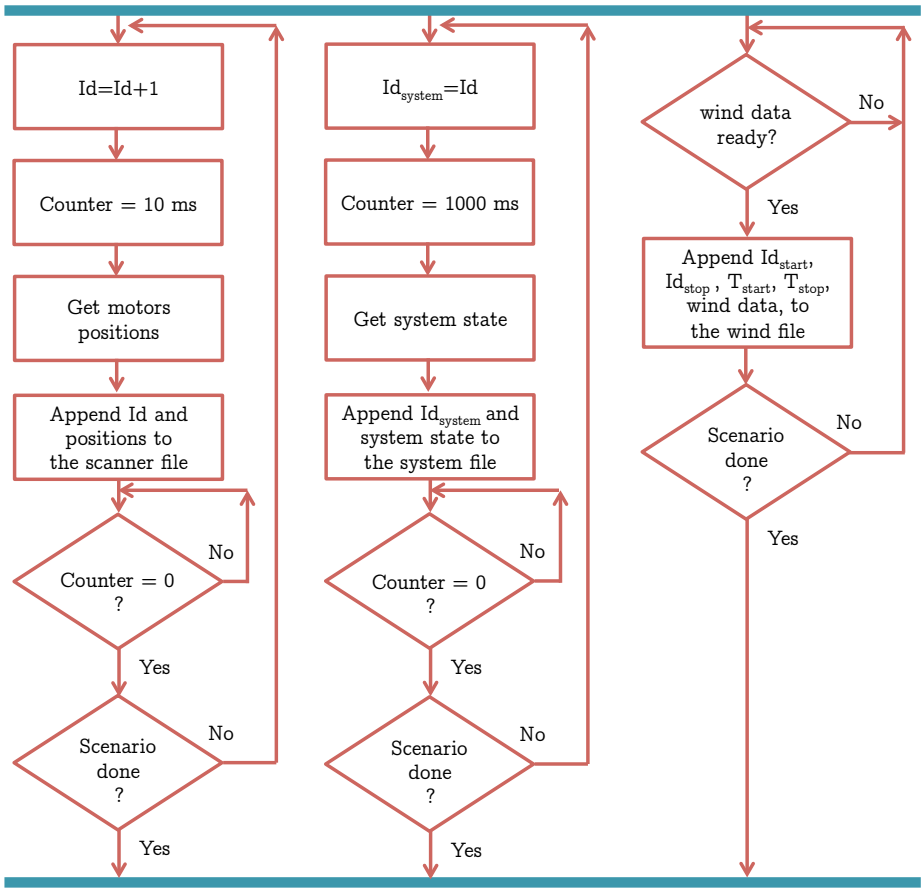

Figure 2.12: The flow diagram of the file storing system

Table 2.6: Parts of the wind file (top), scanner file (bottom left) and system file (bottom right) that were made during the execution of the measurement scenario described by Table 2.2 and Table 2.3

Id_{start}	Id_{stop}	T_{start} [s]	T_{stop} [s]	Distance [m]	Speed [m/s]	CNR [dB]	Dispersion [m/s]	Distance [m]	Speed [m/s]	CNR [dB]	Dispersion [m/s]
...	...	...	...	...	...	...	...	...	...	...	...
13072	13172	0.371	1.373	1100	11.4	-15.3	1.3				
13173	13252	1.384	2.185	300	9.3	-11.5	0.5	241	8.7	-9.43	0.7
13253	13452	2.186	4.173	4000	63	-30.5	3.2				
...	...	...	...	...	...	...	...	...	...	...	...

Id	Motor 1 [°]	Motor 2 [°]	Motor 3 [triggers]
...	...	...	...
13072	20.000	-15.000	1
...	...	...	. ..
13122	20.000	-15.000	5000
...	...	...	...
13172	20.000	-15.000	10000
13173	20.007	-15.007	10133
...	...	...	...
13212	25	-20	14000
...	...	...	...
13252	30	-25	18000
13253	30.05	-25.005	18100
...	...	...	...
13452	60	-90	28000
...	...	...	...

Id	Temperature [°C]	Tilt [°]	Pitch [°]	Heading [°]	Other
...	...	...	...	...	...
...	...	...	...	...	...
...	...	...	...	...	...
...	...	...	...	...	...
...	...	...	...	...	...
...	...	...	...	...	...
13100	25.5	0.5	-0.1	359.0	...
13160	25.5	0.5	-0.1	359.5	...
13260	25.5	0.5	0.1	359.0	...
...	...	...	...	...	...
...	...	...	...	...	...
...	...	...	...	...	...
...	...	...	...	...	...
...	...	...	...	...	...
...	...	...	...	...	...

2.5 Discussion

The presented operational principles and architecture of the software provide the synchronization of the fundamental lidar processes and their accurate time control. As we will see in the next chapter this forms the basis for the time-space synchronization of multiple coherent Doppler scanning lidars. The principles and architecture are portable to other remote sensing devices, such as Doppler radars which emit and steer radio waves, and collect and analyze their returns.

Currently, the principles and architecture have been applied for the development of the long-range WindScanner. The resulting WindScanner client software has been used by DTU Wind Energy on their three WindScanners. Apart from DTU Wind Energy, the software has been installed on three WindScanners owned by the Wind Energy Systems research group from ForWind, University of Oldenburg. Apart from DTU Wind Energy, who has the rights to issue licenses for the software to the participants in the WindScanner.Eu project, the rights are also given to Leosphere. Therefore, the knowledge and experience have been disseminated and it is accepted outside DTU Wind Energy, both by industry and academia.

The next version of the WindScanner client software will include an extended set of measurement scenarios that can be automatically generated. However, the continuation of the WindScanner client software development is limited if the software continues to include Leosphere's proprietary "blackbox", namely the MLE. Future work should be focused on the development of in-house MLE. For this reason, the research should be steered towards the field of signal processing. In order to support this research it would be beneficial to develop a model, such as the Feuilleté model [73, 74], that simulates propagation and return of the laser light under various atmospheric conditions in the time domain, and signal processing of the backscatter signal.

The motion controller of the long-range WindScanners should be used for other applications apart from the applications such as the control of steering, emission and acquisition. For example, the deployment of the long-range WindScanners on ships, or floating platforms, would need compensation for wave induced motion. Providing the information on the yaw, pitch and roll of the platform and by using the inverse kinematics, the motion controller could compensate to a certain extent the impacts of the non-stationary deployment of the lidar. This has been earlier discussed in the case of NOAA's HRDL coherent Doppler scanning lidar [75]. Similarly, providing the long-range WindScanners' feet with motors, and feeding the information on the pitch and roll to the motion controller, the latter can then perform automatic leveling of the long-range WindScanner, which can significantly reduce the time necessary for lidar installation.

Chapter 3

Unifying lidars in the single measurement system

3.1 Introduction

Using multiple coherent Doppler scanning lidars for an experiment, as separate entities without a distant master computer that manages them, tends to create a complex environment, which an experimenter needs to control in order to obtain desirable results. In simpler words, if multiple lidars are used without a master computer, the experimenter would need to prepare measurement scenarios, to execute these scenarios, and to monitor measurements on each lidar individually, usually using multiple remote sessions. These individual and separate interactions with lidars can be time consuming and difficult. Moreover, without the master computer, time synchronization of coherent Doppler scanning lidars is nearly impossible. Central management of the lidars is necessary in order to achieve synchronization.

There are numerous approaches in forming a unified measurement system of multiple lidars managed by a master computer. However, currently two distinct approaches have been identified. In the first approach, which we will call the control approach, the master computer has complete control over the fundamental processes of each lidar in the system. This approach has been somewhat suggested in [54].

The control approach is suitable for those systems where lidars and master computers are connected with cables. Using a wireless instead of a wired connection is prohibitive from the motion control perspective, since the wireless motion control suffers from a large closed loop delay, which represents the time interval needed for the position reading to be received by the motion controller, and further for the according control signal to be received by the actuator. Within the existing wireless techniques, IEEE 802.11b Wireless Local Area Network User Datagram Protocol / Internet Protocol (WLAN UDP/IP) provides the minimum closed loop delay, which is about 3.6 ms [76]. In the ex-

periment on the wireless control of an inverted pendulum using WLAN UPD/IP, it was shown that this closed loop delay resulted in a difference of 20° between the commanded and actual position of the motion system, which is a rather mediocre result [77]. Moreover, the motion controller or the actuator might not get the position reading or the control signal due to lost network packets or the downtime of a wireless link. Situations like these will increase the closed loop delay, leading to a decreased phase margin in the control loop and a potentially unstable motion system [78].

The control approach with a wired connection between the master computer and lidars has been partially applied in the realization of the short-range WindScanner system, with its three short-range WindScanners connected to the master computer using optical fiber cables, with the total length of around 300 meters. The master computer in the short-range WindScanner system has the role to control and synchronize the movement of the lidars' scanner heads.

If the separation between the lidars in a future unified measurement system of multiple lidars is expected to be greater than a few hundred meters, and if a diverse range of the system deployments is anticipated (e.g. offshore, complex terrain, etc.), then the control approach with a wired connection is unsuitable for the realization of the system due to the costs and complexity of the installation. For these reasons a different approach is needed.

In this chapter a novel approach is suggested which mitigates the costs and complexity of the installation. In this approach, hereinafter referred to as the coordination approach, control over the fundamental processes remains on lidars, while the master computer has a role to prepare lidars to perform measurement scenarios, issue the start of the measurements, monitor lidars' activities and intervene if necessary. This approach has been applied in the case of the long-range WindScanner system. Later in this chapter we will see that the coordination approach is not influenced by the wireless network latency, and that it allows freedom in the deployment of lidars and their time synchronization. It should be noted that the time synchronization of multiple lidars is essential for the measurements of fluctuating wind velocity fields (i.e. turbulence measurements) or for shorter time averages of measurements.

The text of the chapter is organized as follows: Section 2 consists of the requirements that were proposed for the formation of the long-range WindScanner system using the coordination approach. The communication protocol used to coordinate the lidars activities with the master computer is given in Section 3. Section 4 is dedicated to time synchronization of the lidars in the long-range WindScanner system.

3.2 Requirements for the coordination

The following requirements have been set in order to apply the coordination approach and to achieve accurate time synchronization of the lidars in the long-range WindScanner system:

1. Synchronization of the fundamental processes and their accurate time control at the level of a single lidar
2. Lidars have to be equipped with an accurate clock, which will provide a common time base
3. Master computer should be able to communicate with the lidars by exchanging data packets using a wide range of network types
4. Communication between the master computer and lidars should consist of a general set of commands sent from the master computer to lidars, their responses to commands and their action on commands
5. Data packets, which encapsulate the commands and responses, should be small enough to allow an uninterrupted and fast coordination of lidars even in the case of mobile networks such as GSM

The first requirement has been met with the operational principles and corresponding WCS, which have been described in the previous chapter. The second requirement has been met with the installation of a GPS clock with the accuracy of 250 ns in each WindScanner. The remaining three requirements have been achieved with the development of a special remote sensing communication protocol (RSComPro) [79], and appropriate optimization of the WCS and development of the master computer software (MCS) based on this protocol.

The requirement for the general set of commands has been set, since it is anticipated that in future we would be able to coordinate a diverse range of lidars and other remote sensing instruments from the master computer.

3.3 Remote sensing communication protocol

3.3.1 Introduction

The RSComPro defines a set of:

- Commands sent from master computer to WindScanners
- Appropriate WindScanners' actions in response to commands
- Responses to commands sent from WindScanners to master computer
- Possible alerts sent from WindScanners to master computer
- Packet structure of each command, response and alert

The coordination of the WindScanners by the master computer is achieved by exchanging commands and responses, which are encapsulated in network packets containing strings formatted using Extensible Markup Language (XML). The RSComPro defines the packet structure.

Consequently, each command sent to a WindScanner actually represents a network packet, which is sent via network, and once it is delivered to a WindScanner, the packet information is extracted and parsed, which results in an action (e.g. moving a scanner head to a certain position) or in a set of actions (e.g. forming measurement scenario's motion program and range gate file). Once the command has been carried out, the WindScanner sends a response to the command. As in the case of the command, the response is encapsulated into the RSComPro packet, which is sent over the network to the master computer. Upon receiving the packet, the information is extracted and parsed, resulting in an action (e.g. display of the latest retrieved radial velocity) or a set of actions (e.g. synchronization of multiple WindScanners). Alerts are sent independently from WindScanners in case of states of alarm, such as high temperature, low disk space, etc. Also, they are encapsulated into the RSComPro packet.

The MCS and WCS accomplish the encapsulation of the commands, responses and alerts, their sending and actuation.

3.3.2 Exchange of the RSComPro packets

Interaction between the master computer and WindScanners is achieved using the set of communication protocols defined by the Internet protocol suite (IPS). These protocols create an environment in which the MCS and WCS are able to exchange RSComPro packets, therefore they are able to send and receive commands, responses, and alerts. The IPS specifies how RSComPro packets are addressed, transmitted, routed and received by the master computer and/or WindScanners. On the other hand, the RSComPro forms the packets and assigns the actions that the reception of these packets will produce. The whole configuration of the IPS and RSComPro can be described as a four-layer structure, commonly known as the Transmission Control Protocol/Internet protocol suite stack (i.e. TCP/IP stack) (Figure 3.1).

Hierarchically, the RSComPro represent the protocol that governs the application layer of the TCP/IP stack. At this layer the packets are formed, or the information from the packets is extracted and actuated in the software (either the MCS or the WCS). Each packet, whether it represents a command, response or an alert, has an XML structure given in Table 3.1.

The XML element, named **packet**, has four attributes. The first attribute is **Client** which contains the name of the device that sends the packet (e.g. "Kosava" for the WindScanner named Kosava). The attribute **PckNo** indicates the number of the package in the form of $SysID.Current$, where $SysID$ value is given by the master computer and depends on what number a WindScanner has in the list of all connected WindScanners. $SysID$ has the value equal to 0, if the packet is sent from the master computer. $Current$ is the sequence number of the current packet. The value contained in the attribute **Cmd** indicates what

command is sent from the master computer. In the case of the WindScanner's response to the command, it retains the same value as the command. If a WindScanner is issuing an alert (e.g. for low disk space) the attribute **Cmd** is equal to 0000. The last attribute is **Alert**, which is equal to 0, if the execution of the master computer command was performed without errors, 1 if an error occurred during the execution, or 2 if an alert is issued by WindScanners. For values of **Alert** different than 0, the element **msg** contains an explanation. The elements **element 1, element 2, . . . , element N** contain values that depend on the command and response.

<packet **Client**="*Kosava*" **PckNo**="1.3" **Cmd**="2200" **Alert**="0">
<element 1> 124520.50 < /element 1>
<element 2> 141212 < /element 2>
. . .
<element N> 40.091042 < /element N>
<msg>< /msg>
< /packet>

Table 3.1: The XML structure of a RSComPro packet

Before sending the RSComPro packet from the source computer to the destination computer, the MCS or the WCS supply the 5-tuple to the lower layers of the TCP/IP stack. The 5-tuple consists of the following information:

1. Source IP address
2. Source Port
3. Destination IP address
4. Destination Port
5. Protocol type (e.g. TCP)

After this step the encapsulation of the packet starts, as it descends through the lower layers of the TCP/IP stack (Figure 3.1).

The protocol type, source and destination ports represent the necessary information that is provided to the transport layer of the stack. By using this information at the transport layer, the RSComPro packet is encapsulated in the data part of the transport layer message, where the header part of the message contains the source and destination ports and other information, depending on the protocol type (Figure 3.1). TCP and UDP are the protocol types used for communication between the master computer and the WindScanners.

Following the transport layer, the network layer wraps the message in the payload of an IP Datagram, assigning the source and destination IP address from the 5-tuple to the header of the IP Datagram. The creation of an IP Datagram represents the creation of a basic networking element, which is sent to the destination computer using the link layer. Typical size of an IP Datagram is

around 1 kB, of which the overhead is around 40 B and the rest is the RSComPro packet. The additional encapsulation occurs at the link layer, where the IP Datagrams are turned into bits which are appropriate for a particular type of network (e.g. LAN). Once the IP Datagram reaches the destination computer, the process is reversed. A payload is extracted from the IP Datagram. The transport layer extracts data from the payload and passes it to the application layer. Finally the RSComPro decodes data from the XML format to a format useful for the application. This data is further used in the MCS or the WCS and it results in an action or a set of actions.

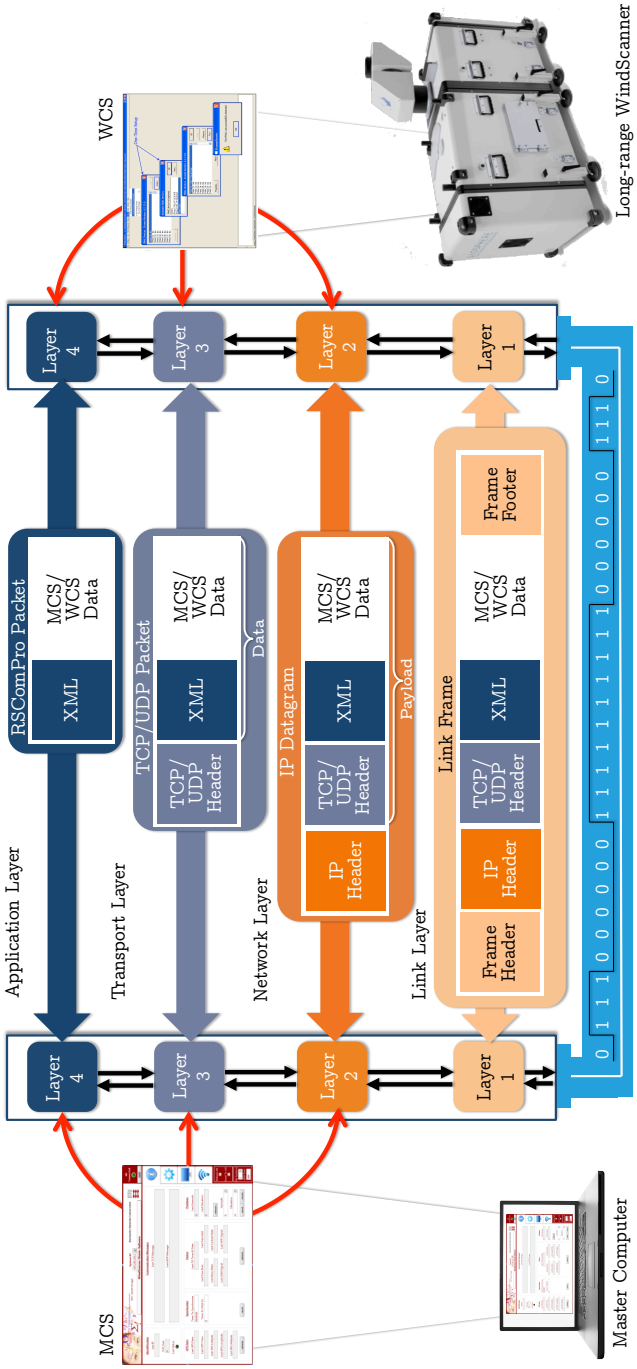

Figure 3.1: Encapsulation and transport of RSComPro packets

3.3.3 UDP commands and responses

UDP does not have handshaking dialogues, which means that the MCS and WCS can exchange transport layer messages without setup of special transmission channels or data paths. The characteristic of this protocol is that it offers fast delivery of messages. However, there is no guarantee that the messages will be delivered. In the case of the RSComPro, UDP is used to support the handshaking process for the TCP connection and to send basic commands that activate core processes in WindScanners.

All UDP commands are sent over port 62300 from the master computer to WindScanners, and the master computer utilizes the same port to receive incoming responses and alerts from WindScanners. Therefore, the MCS and WCS reserve this port for the exchange of UDP commands and responses. All the commands can be routed simultaneously to all WindScanners (Figure 3.2, left image), to a number of WindScanners (Figure 3.2, central image), or to a single WindScanner in the network (Figure 3.2, right image). These three methods of routing commands over the network are known as broadcast, multicast and unicast, and they are supported by the IP protocol, version 4. WindScanners are restricted to unicast responses and alerts only to the master computer.

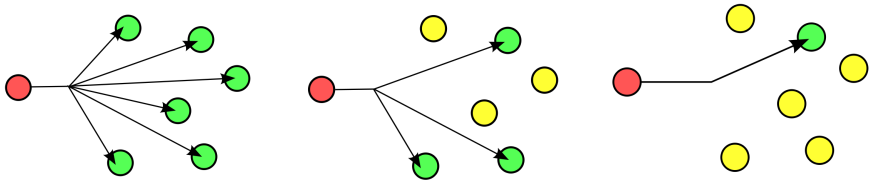

Figure 3.2: Left image Broadcast, central image Multicast, right image Unicast. Red circles represent the master computer, green and yellow circles WindScanners.

The list of the RSComPro commands that are sent using UDP are given in Table 3.2. This list represents the UPD commands defined by the RSComPro version 1 from September 2013. The following is the summary of all the implemented commands, where details about their XML structure and examples of the communication between the master computer and WindScanners can be found in [79]:

- With the **WhoIsThere?** command TCP connections are established between the master computer and available WindScanners in the network. When broadcast, it is used to detect how many lidars are present in the network and to further support the process of the multi-step handshake for the TCP connection.

- When **Abort** is received by a WindScanner, it performs a sudden stop of the current operations, resulting in an immediate stop of any moving parts, laser pulse emission and acquisition of the backscattered light. After the

completion of the command the WindScanner is locked, and it does not react to any command apart from the commands **Unlock** and **IsBusy?**.

- Command **Unlock** unlocks the WindScanner for further use, while command **IsBusy?** returns the information about the current status of the WindScanner (e.g. measuring).
- The command **Stop** results in a soft stop of the current operations.
- With the command **GetStates** the master computer application receives information about the WindScanner, such as current GPS (computer) time, available system RAM, available hard drive space, if the WindScanner is available to perform measurements, if it is locked, the strength of the GSM signal, and the strength of the Wi-Fi signal.
- Command **Reset** resets the WindScanner (i. e. its computer).
- The **Shutdown** command, upon receipt, results in the shutdown of the WindScanner.

Command	Code
WhoIsThere?	1100
Abort	1200
Unlock	1300
Stop	1400
GetStates	1500
IsBusy?	1600
Shutdown	1700
Reset	1800

Table 3.2: Implemented UDP commands

3.3.4 TCP commands and responses

TCP is one of the core protocols of IPS that offers reliable delivery of data from the software on the source computer to the software on the destination computer. IP Datagrams can be lost, duplicated, or delivered out of order due to numerous problems with the network, such as network congestion and high traffic load. For these reasons TCP has a mechanism that can detect problems, request retransmission of lost data, rearrange out of order data and also minimize network congestion. It guarantees that all received bytes are identical to the bytes sent, and as such TCP is optimized for accurate delivery rather than timely delivery. TCP is a connection orientated protocol, which means that in order to use TCP, special data paths have to be established in a multi-step handshake process before any data transfer is achieved.

Therefore, before sending any command over TCP, it is necessary to create the TCP connection between the master computer and WindScanners. After the start of the MCS, the software broadcasts the **WhoIsThere?** command over UDP through the network (Figure 3.3). Once the WindScanners receive this command, they respond to the master computer with information about their names, IP addresses and an enquiry for a TCP port. After receiving their responses, the master computer initializes the three-step handshaking mechanism that occurs at the transport layer, which establishes the TCP connections among the master computer and WindScanners (Figure 3.3). The formation of the TCP connections further allows sending and receiving of the TCP commands and responses.

The list of the RSComPro commands that are sent over TCP are given in Table 3.3. Similar to the UDP list of commands, the list of TCP commands represents the commands defined by the RSComPro version 1 from September 2013, apart from the last command which will be added to the new version of the RSComPro. The following is the summary of all the implemented commands:

- Upon receiving the command **GoHome**, a WindScanner sets the scanner head to the home position (see the home position definition in Chapter 4). Once the scanner head reaches the home position, the WindScanner sends a response regarding the success of this task to the master computer.

- With the **GetGPS** the master computer acquires information concerning longitude, latitude, elevation and GPS time and date from the WindScanner.

- The response to the command **GetCompass** contains the information from the WindScanner compass - heading, pitch, roll, and also the internal temperature of the WindScanner. This last information is a precedent, and it is due to the hardware configuration of the WindScanner compass that it also allows measurements of the temperature.

- The command **GetConfiguration** returns information regarding the lidar configuration of the WindScanner. This information includes the parameters used for the configuration of EDFA, pulse generator, acquisition board, etc.

- The reply on command **GetPosition** provides the current position of the scanner head.

- On the other hand, the command **SetPosition** results in actuating the position of the scanner head to the position given by this command.

- A current measurement scenario or a list of scenarios are provided through the response to the **GetScenario** command.

- In order to set a new scenario or a list of scenarios, the master computer sends the **SetScenario** command. This command contains following information: type of trajectory (e.g. VAD, DBS, PPI, RHI,...), number of

LOS measurements, distances at which the radial velocity will be retrieved for each LOS measurement, number of repetitions of the same measurement scenario, laser pulse type, accumulation time per measurement point and FFT size.

- Once the scenario or the scenario list is set, the WindScanner will start to execute the scenario(s) at the precise time given with the command **Measure**.
- The response to the command **GetData** is the instantaneous data stream of measurements, at the moment they are done.
- Command **Wipe** executes cleaning procedure of the glass window of the scanner head.
- Command **GetCapabilities** retrieves the capabilities of the WindScanners.
- Command **Synchronize** is used to keep the fundamental lidars' processes among multiple WindScanners in sync during the synchronous wind velocity field measurements.

More details about the **Synchronize** command will be explained in the following section of this chapter, while details about the rest of the implemented TCP commands can be found in [79].

Command	**Code**
GoHome	2100
GetGPS	2200
GetCompass	2300
GetConfiguration	2400
GetPosition	2600
SetPosition	2700
GetScenario	2900
SetScenario	3000
Measure	3100
GetData	3200
Wipe	3300
GetCapabilities	3400
Synchronize	3500

Table 3.3: Implemented TCP commands

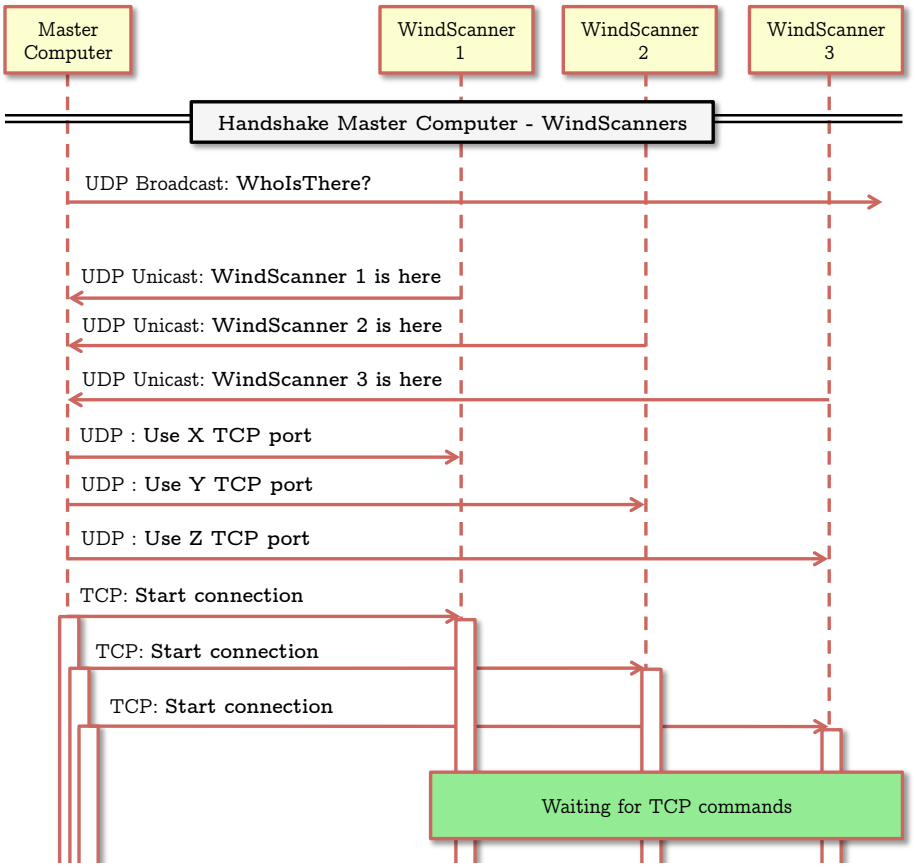

Figure 3.3: Sequence diagram of initial handshake between master computer and WindScanners

3.4 Time syncronization

3.4.1 Introduction

Within the motion controller, the phase and servo clocks' signals set the heart beat for the controller, synchronizing the controller's hardware and software operations that provide accurate control. Also, these signals control the timing of the scanner head moves and trigger signal. The source for the phase and servo clocks' signals is the crystal clock oscillator.

From the motion controller perspective, the time of each action (e.g. motion of the scanner head, sending triggers, etc.) is represented as a number of crystal clock oscillator beats. Two consecutive beats are separated in time for a value

equal to the reciprocal of the crystal clock oscillator frequency, which is 20 MHz. Since the crystal clock oscillator frequency has an accuracy of roughly ± 50 PPM, commanded duration of an action (e.g. time move of the scanner head) or set of actions (e.g. duration of the motion program) will drift from the expected duration with a drift speed in the range of ± 50 $\mu s/s$.

Based on this value, it should be expected that in the case of synchronous 3D wind field measurements with the long-range WindScanner system, the WindScanners will drift apart during the execution of the scenario if there is no intervention by the master computer or the user. In the worst case scenario the theoretical maximum time difference between the 'fastest' and 'slowest' WindScanner in the system, or simply the maximum lag, will increase over time with the drift speed which is in a range of ± 100 $\mu s/s$ regardless of the number of WindScanners in the system. This means that the maximum lag will be in a range of ± 720 ms after two hours of continuous synchronized measurements with multiple long-range WindScanners.

3.4.2 Maximum lag without the synchronization routine

An experiment was performed in order to test if the calculated drift speed range is correct. During the experiment, three WindScanners were prepared to synchronously intersect their laser beams at three points in the atmosphere. These points were positioned next to three sonic anemometers located at a meteorological mast at three heights (76, 94, and 118 m). At each point of intersection radial velocity measurements were taken, while between each point of intersection there were no measurements but pure motion. The first iteration of the experiment lasted for two hours.

The WindScanners and the master computer formed a Local Area Network via Ethernet and one router/switch. The measurement scenarios for this experiment were prepared at the master computer and sent to the WindScanners using the command **SetScenario**. Following the response from the WindScanners that the scenarios were received, the start of the measurement scenarios was set using the command **Measure** for each WindScanner. The start time was set to be identical at all WindScanners. Following the start of the measurement scenarios, the command **GetData** was issued to all WindScanners, which resulted in the instantaneous data stream of radial velocity measurements, corresponding GPS time of completion of the measurements, scanner heads' positions, etc. Therefore, all the necessary information was received by the master computer in order to monitor the time synchronization of the WindScanners in real-time. During the execution of the measurement scenario there was no interaction with the motion controllers of the WindScanners. Instead, the master computer only acted as a receptor for the information. Details on the location of the experiment, measurement scenarios, measurement results, etc. are provided in Chapter 5.

The received information was used to compute the maximum lag as a function of time. The evolution of the maximum lag during the two-hour period is given in Figure 3.4. As expected, the derived drift speed using the experimental

data corresponds well to the upper limit of the drift speed calculated using the crystal clock oscillator accuracy.

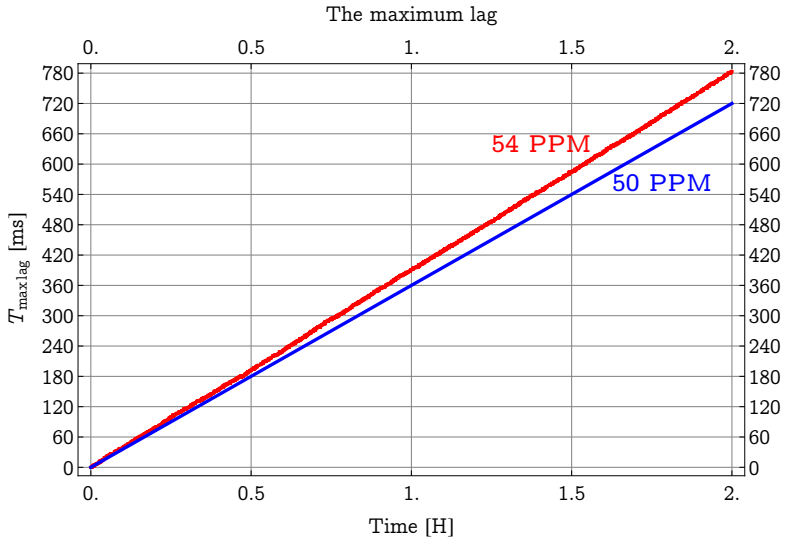

Figure 3.4: Experimental evolution of the maximum lag of the long-range WindScaner system (red line) during a two-hour execution of the synchronous 3D wind field measurements in three points, and the nominal uper limit of the drift speed (blue line).

3.4.3 Diminishing the maximum lag

In the course of time, the evolution of the maximum lag of the long-range WindScanner system prohibits the application of the system for the synchronous 3D measurements of wind velocity fields. As previously showed the crystal clock oscillator accuracy determines the level of the lag. In the absence of a central clock providing synchronicity, a few approaches have been identified that could help in diminishing the maximum lag and prevent its evolution in the course of time. These approaches consist of:

- Replacing the crystal clock oscillator in the motion controller with an oven controlled crystal clock oscillator with the same frequency and the level of accuracy higher than 0.05 PPM, which would provide the maximum lag of the system below 10 ms after 24 hours of the continuous synchronized measurements
- Substitution of the crystal clock oscillator and GPS clock with an atomic clock which would provide accurate time and frequency base
- Interaction of the master computer with the motion controllers during the execution of the synchronous measurements

The first two approaches would need an upgrade of the existing hardware of the WindScanners, which would increase the total cost of the WindScanners. The last approach employs the existing hardware and software to attain and keep the WindScanners synchronized. In short, this approach uses the master computer to slow down WindScanners that are faster than the slowest WindScanner in the system by extending the commanded time of their motions in the measurement scenarios' loops. Since this approach does not raise any extra costs, it was used to diminish the maximum lag of the system and to prohibit its evolution in the course of time. Updates of the WCS were made in order for this approach to work.

First, the structure of motion programs has been changed by adding extra lines of the code. An example of an updated motion program concerning the experiment from the previous section is given in Table 3.4. The extra lines in the motion programs' code allow the dynamic change of the commanded time for the motion of the scanner head, by changing the variable $P1983$. Also, the network module of the WCS, which is responsible for communicating with the master computer, was formed in a way that once it receives the command **Synchronize** from the master computer, it extracts the value that indicates how much the WindScanner, on which it runs, is in the lead in comparison to the slowest WindScanner in the system. Further on, the WCS sets the variable $P1983$ to be equal to this value, which results in the extension of the last motion of the motion program. By extending the commanded time, WindScanners that are faster than the slowest WindScanner are slowed down, and thus synchronized with the slowest WindScanner in the long-range WindScanners system.

On the other hand, the MCS was coded from the beginning to calculate the lag between the slowest and and other faster WindScanners in the system in real-time, during synchronous measurements. An automatic routine was set in the MCS, which sends the synchronization commands to WindScanners that are faster than the slowest WindScanner, once a user configured maximum lag threshold is passed.

```
1 -> A                  ; Assign motor 1 to the Azimuth axis
2 -> E - A              ; Assign motor 2 to the Elevation and Azimuth axis
                        ; with opposite signs in order to compensate
                        ; for the kinematic coupling
3 -> T                  ; Assign phantom motor 3 to the Trigger axis

N_s = 1500              ; Number of iterations of the same scenario
TM10000                 ; 10000 milliseconds move time to the first intersection
A(54.8)E(59.3)          ; point at 118 m

M361=0                  ; Reset motor 3 position

P1983=0                 ; Reset the synchronization variable

WHILE(N_s ≥ 0 )         ; Loop on the number of iterations

   N_s = N_s - 1        ; Decrement counter

   TM700                ; 700 ms move time
   A(54.8)E(59.3)       ; to the first intersection point

   TM1000               ; 1000 ms stand still and execution of
   T(M361+10000)        ; 10000 triggers, which corresponds to PRF=10 kHz

   TM500                ; 500 ms move time
   A(54.6)E(53.2)       ; to the second intersection point

   TM1000               ; 1000 ms stand still and execution of
   T(M361+10000)        ; 10000 triggers, which corresponds to PRF=10 kHz

   IF(P1983 > 0)        ; IF-case for synchronization
     TM(600+P1983)      ; (600 + P1983) ms move time
     A(54.4)E(47.6)     ; to the third intersection point
     P1983=0            ; Reset the synchronization variable
   ELSEIF               ;
     TM600              ; 600 ms move time
     A(54.4)E(47.6)     ; to the third intersection point
   ENDIF                ;

   TM1000               ; 1000 ms stand still and execution of
   T(M361+10000)        ; 10000 triggers, which corresponds to PRF=10 kHz

   M361=0               ; Reset motor 3 position
ENDWHILE
```

Table 3.4: Motion program for the synchronous wind velocity measurements. The blue lines of the code indicate the extension of the initial motion program for synchronization.

3.4.4 Maximum lag with the synchronization routine

With the automatic routine switched on, the threshold set to 10 ms, and modifications of the WCS, the previous experiment was repeated and run during a few days (see details in Chapter 5).

In Figure 3.5 the results for the first 30 minutes of the experiment made with and without the automatic routine are shown. The results with the automatic routine switched on indicate that the evolution of the maximum lag was prevented, by zeroing the lag in the system each time the threshold of 10 ms was passed.

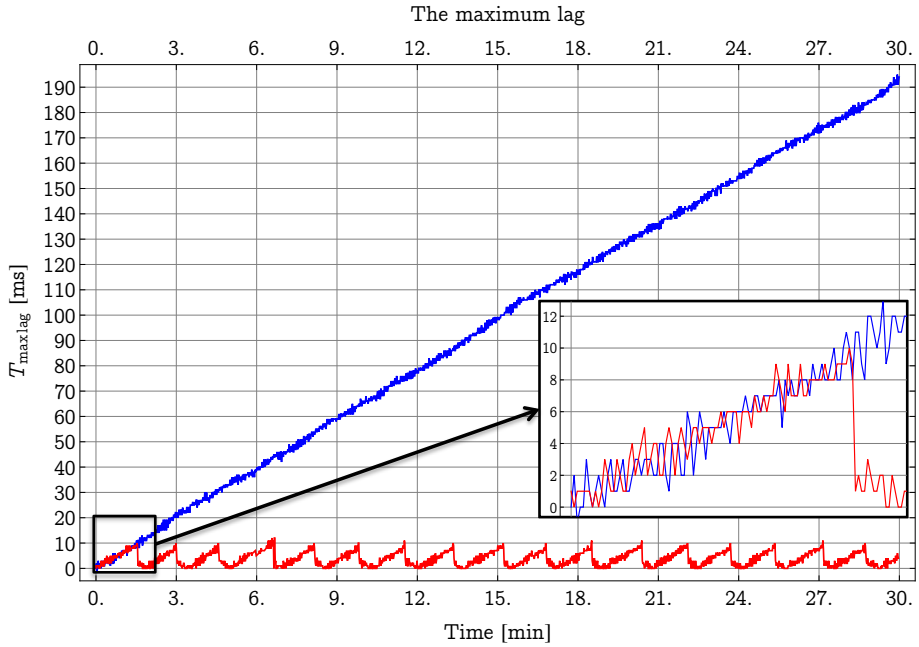

Figure 3.5: Experimental evolution of the maximum lag of the long-range WindScaner system with (red curve) and without (blue curve) the syncronization routine

The threshold can be lower, but the value of 10 ms has been used so far in all synchronous wind velocity measurements with the long-range WindScanner system. The value of 10 ms was chosen since, for the highest measurement frequency of 10 Hz, in the worst case scenario, 90% of accumulation will occur at the same time for all WindScanners in the system, providing we use step-stare measurement scenarios. This practically means that the maximum lag of the system can be considered negligible, and therefore the WindScanners in the long-range WindScanner system are synchronized.

Moreover, with the threshold of 10 ms, the master computer software sends the synchronization commands every 1.5 minutes which does not overload the

network. The IP Datagram of these commands is not bigger than 600 B. Also, the IP Datagrams responding to command **GetData**, needed to calculate the lag, are of similar size. This practically means that even with the GSM technology, which has data transfer speed of up to 9.6 kb/s, the synchronization of the multiple WindScanners can be achieved within a few seconds, during which the evolution of the maximum lag is negligible. This means that the network latency has a negligible effect on the synchronization.

For the lower threshold value, the transmission of the commands would be more frequent and, particularly for threshold values below 3 ms with the current crystal clock oscillator, the transmission could possibly overload the network since this threshold value corresponds to the level of the jitter in the curves shown in Figure 3.5. This jitter originates from both the stability of the crystal clock oscillator frequency and from the interval needed for the execution of the WCS request for the GPS time.

3.5 Discussion

In this chapter, the novel approach in the formation of a unified measurement system of multiple lidars, which allows simultaneous coordination of multiple lidars through a UDP/IP and TCP/IP network, has been presented. This approach has two particular aspects.

Since the lidars can be connected with the master computer using a wireless network, there is no limitation regarding the separation between the lidars in the system. Therefore, the first aspect of the coordination approach is the flexibility of the lidars deployment.

It has been shown that time synchronization between the lidars in the system has been successfully achieved, with the maximum lag of 10 ms in the case of the long-range WindScanner system. The number of lidars and the duration of the measurement scenarios do not influence the maximum lag. This represents the second aspect.

However, the coordination approach requires lidars' operational principles that provide accurate synchronization and time control of the fundamental lidar processes. Also, it is required that the lidars have accurate clocks, such as a GPS or an atomic clock, since the common time base for lidars is essential for the lidars' time synchronization monitoring. Moreover, the master computer and lidars software have to be developed in a way which allows the exchange, processing and actuation of the RSComPro packets. Above all, the master computer and lidars have to be connected to a network. Potentially, the coordination approach might provide faster exchange, processing and actuation of the RSComPro packets, if the packets are encoded in the binary format instead of the XML format, since the parsing of the RSComPro packets can be the bottleneck of efficiency.

It would be interesting to test the maximum rate at which the RSComPro packets can be received, parsed and actuated in the MCS and WCS without the loss of the packets. This test would provide means to investigate whether it is

necessary to switch to the binary encoding of the RSComPro packets. Also, it would be interesting to use the protocol for the software optimization of other remote sensing instruments, which would allow the coordination of diverse range of remote sensing instruments from a single master computer. By doing this, measurement campaigns with remote sensing devices would be less complex to prepare, monitor and control.

In relation to the existing software solutions and long-range WindScanner system, future work should be focused on developing the MCS extensions. For example, implementation of routines in the MCS that handle a range of the WindScanner alarm states would improve the autonomy of the long-range WindScanner system, which would probably boost the availability of data. An interesting extension of the MCS would be the implementation of a routine that automatically generates the measurement scenarios depending on the user criteria, such as the criteria for the wind farm wake tracking. Moreover, the kinematic model of the scanner head should be integrated in the MCS. This will allow an automatic generation of the optimized measurement scenario for the synchronized measurements with multiple WindScanners, using the positions of the WindScanners and the positions of measurement points in the atmosphere, as well as the kinematic limits.

Along with software development, the replacement of the existing crystal clock should be made in order to achieve tighter synchronization of the WindScanners, and a decreased usage of the network for this task.

Chapter 4

Uncertainty of the laser beam pointing

4.1 Introduction

One of the main advantages of coherent Doppler scanning lidars in comparison to the traditional anemometry is the possibility to acquire information regarding the wind velocity in a great many points of interest in the atmosphere. As explained earlier, this is done by measuring the radial velocities at those points.

In order to interpret these measurements correctly, it is imperative to know how accurately a scanning lidar can direct the laser beam towards the points of interest, and how accurately the lidar can sense the distance from which the backscattered light is coming from. In other words, it is necessary to estimate the uncertainty of the laser beam direction and sensing distance of the lidar, which together define the laser beam pointing uncertainty (Figure 4.1).

Expressing the laser beam pointing uncertainty and setting the coverage factor to be equal to one provides the means to define the volume of the atmosphere, within which with a 68% probability we expect the acquisition of the radial velocity for a given laser beam direction and particular distance along the laser beam (Figure 4.2). It can be shown that the volume has the shape similar to a cube. For this reason we will refer to it as the probability cube in the following text. The center of this volume represents the location of the point of interest in the atmosphere where we want the acquisition to take place.

From the perspective of the long-range WindScanner system, under the assumption of the absolute time synchronization of the system, the smaller the dimensions of the probability cube are, the closer the laser beams are to intersect each other at the points of interest. This reflects on the better space synchronization of the long-range WindScanner system.

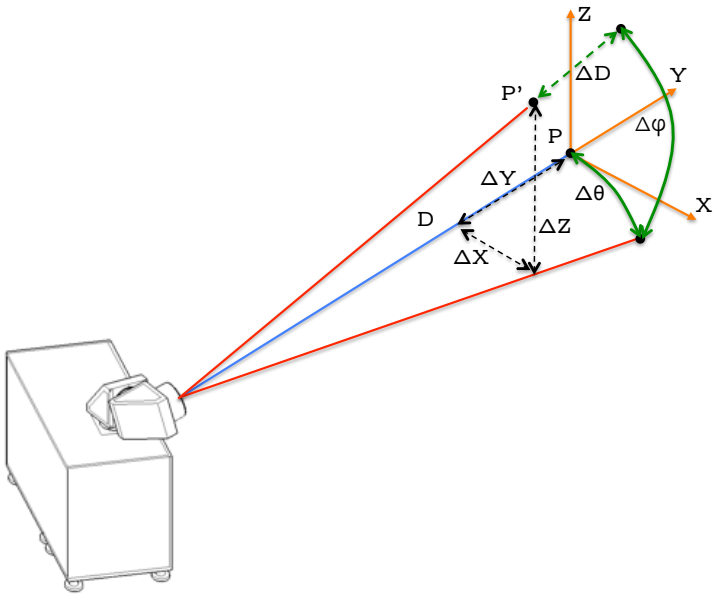

Figure 4.1: The point P represents the expected position in the atmosphere at which the radial velocity should be retrieved. However, due to the displacement of the laser beam direction around the azimuth axis $\Delta\theta$ and the elevation axis $\Delta\varphi$, and due to an error in the sensing distance ΔD, the measurements are taken at the point P'.

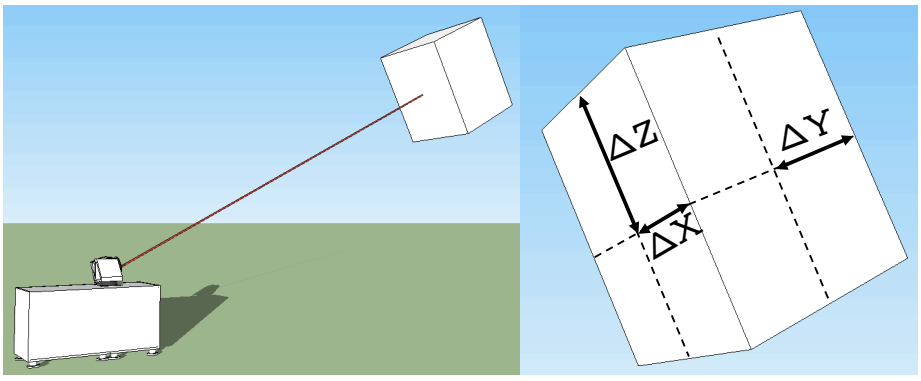

Figure 4.2: The actual position of the point P from Figure 4.1 is probably within the volume of the probability cube.

There are many factors that influence the accuracy of the laser beam pointing. Currently, the error in measurements of the time of flight of the laser pulse has been identified as the only source of the sensing distance uncertainty. On the other hand, the following sources of the laser beam direction uncertainty have been identified as uncertainty contributions:

- Perpendicularity of the rotation axes
- Servo error
- Mechanical imperfections of the scanner head gear box
- Gear backlash
- Position readings of the scanner head coming from the motor encoder
- Connection of the scanner head with the stiff part of the lidar such as the lidar casing
- Dynamics of the lidar (e.g. mechanical resonances)
- Flatness of the mirrors' surface
- Consistency of the reflective index of the mirrors' surface and the glass window of the scanner head
- Alignment of the optical components, particularly mounting of the mirrors
- Home position of the scanner head
- Leveling of the lidar during measurements
- Refractive index of the atmosphere

The following sections of this chapter contain discussions on the laser beam pointing uncertainty contributions originating from position readings of the scanner head coming from the motor encoder, connection of the scanner head with the casing, mounting of the mirrors, home position of the scanner head, leveling of the lidar and measurements of the time of flight of the laser pulse. Since the mechanical imperfections of the gear box and gear backlash are related to the position readings of the scanner head, the corresponding section of this chapter also includes discussions on these two uncertainty contributions. The discussions are based on the example of the long-range WindScanner. Other sources of the uncertainty have not been studied due the limited time to perform the assessment.

For each discussed source of the laser beam pointing uncertainty, a testing procedure will be suggested, and where the testing procedure has been applied the magnitude of the contribution to the laser beam pointing uncertainty will be calculated. Also, for each source of uncertainty, a suitable approach in reducing its uncertainty contribution will be proposed. The chapter ends with a section

consisting of a rough estimation of total uncertainty, which takes into account all the discussed uncertainty sources.

In the existing literature, the information relating to the laser beam pointing accuracy of any type of coherent Doppler lidar are scarce. The most comprehensive accuracy study was performed for a nacelle based lidar [80]. This study devises the testing procedure necessary for the estimation of the laser beam pointing accuracy of nacelle based lidars. In comparison to this work, the study [29] only discusses the implications of the laser beam pointing accuracy on the retrieved wind velocity with ground-based coherent Doppler lidars with the fixed scanning geometry for vertical profiling of the wind velocity. There are no such studies for scanning lidars known to the author, therefore the following testing procedures and the approaches for the improvement of the laser beam pointing accuracy are new and original work.

4.2 Position readings from the motor encoder

4.2.1 Control of the scanner head positioning

Directing the laser beam into the atmosphere is done by executing a pre-defined trajectory, consisting of consecutive positions of the scanner head in azimuth and elevation angles in respect to time. These angles define the expected (or commanded) laser beam direction. Vibrations from the environment, imperfections of the moving mechanical structure (i.e. gear box), friction and other disturbances affect how accurately the trajectory is executed, and thus how accurately the actual laser beam direction corresponds to the expected laser beam direction.

The role of the motion controller is to control the elevation and azimuth motors to execute the trajectory with the minimum servo error (difference between the commanded and actual positions) and to mitigate the consequences of the disturbances. This task is handled by the feedback and feedforward controls which work together, and they represent essential elements of the control loop of motion controllers (Figure 4.3).

Based on the input trajectory the feedforward control proactively generates control signals which result in the force to accelerate the rigid mass, and to suppresses the disturbances which arose due to the viscous and Coulomb friction. These disturbances are known disturbances, since their effect on the positioning accuracy of the scanner head can be measured.

The feedback control is used to mitigate the effects of the unknown disturbances. This control generates the control signal only when the servo errors appear, i.e. retroactively. In contrast to the feedforward control that needs only a user-defined trajectory to generate the control signals, the feedback control needs the continuous acquisition of the scanner head position.

However, for both controls, tuning of the parameters that govern the process of the control signal generation is done by measuring the actual position in respect to the commanded position, i.e. relating the input of the control loop

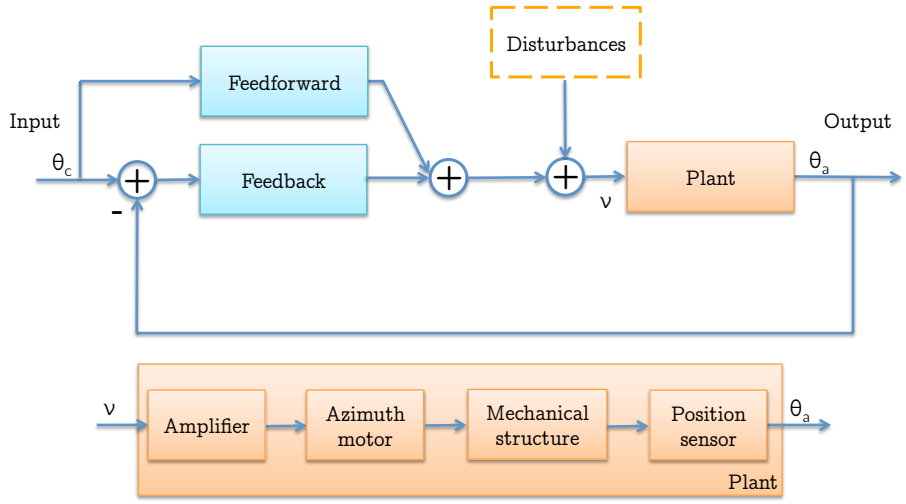

Figure 4.3: Block diagram of the control loop that governs the rotation around the azimuth axis. The input signal θ_c represents the trajectory set points. The output signal θ_a represents the current scanner head position acquired by the azimuth motor encoder.

to its output (Figure 4.3). For example, the parameters of the feedforward control are tuned using the servo error measurements during the execution of the trajectory that consists of three parts: acceleration, constant speed and the motion direction change. In the case of the feedback control, the tuning process is somewhat more complicated and has been described in details in different literature. The following references are recommendable [81, 82].

As was mentioned above, the position measurements are necessary for the proper functioning of the control loop and tuning of the feedback and feedforward parameters. In the WindScanner case, the position measurements are obtained from the rotary encoders attached to the motors' shafts (Figure 4.6). The resolution of these encoders is 0.0001 °. The feedback and feedforward parameters are tuned using the software package PMAC Tuning Pro, which is based on the tuning in the time domain using the analysis of the servo error on the step and trapezoid profile of the speed of the scanner head.

Since the motors drive the gear box that rotates the scanner head, and thus direct the laser beam, the acquisition of the scanner head positions from the motors' encoder does not necessarily correspond to the actual position of the scanner head. This doubt arises due to the complex nature of the interaction between the motors and the gear box and due to imperfections of the gear box itself (e.g. tolerances in manufacturing of the gears, gear worms, etc.). Therefore, tuning of the feedforward and feedback parameters, and also using the position measurements from the motors' encoder to trigger the feedback control, brings an uncertainty in the accuracy of the scanner head positioning

and the control loop performance.

4.2.2 Testing procedure

In order to assess how accurately the scanner head can be positioned, with the above described approach, it is necessary to measure the actual (i.e. true) position of the scanner head with respect to the commanded position. For this type of tests, the secondary set of encoders was installed on the scanner head (reference encoders) Figure 4.4. A rotary encoder with resolution of 0.009° was attached to the bottom of the scanner head, measuring the actual azimuth position of the scanner head. A linear encoder was attached to the upper part of the scanner head, measuring the actual elevation position of the scanner head, by fixing the optical readhead at the upper part of the scanner head that only rotates around the azimuth axis, and wrapping a gold incremental tape around the 'neck' of the scanner head part that rotates around the elevation axis. The linear encoders' readings represent the information about the traveled distance. However, due to the setup of the encoder and the knowledge of the radius of the 'neck', this information can be translated in the 'traveled' angle. This particular sensor setup provides the acquisition of the actual elevation position of the scanner head with the resolution 0.0009°.

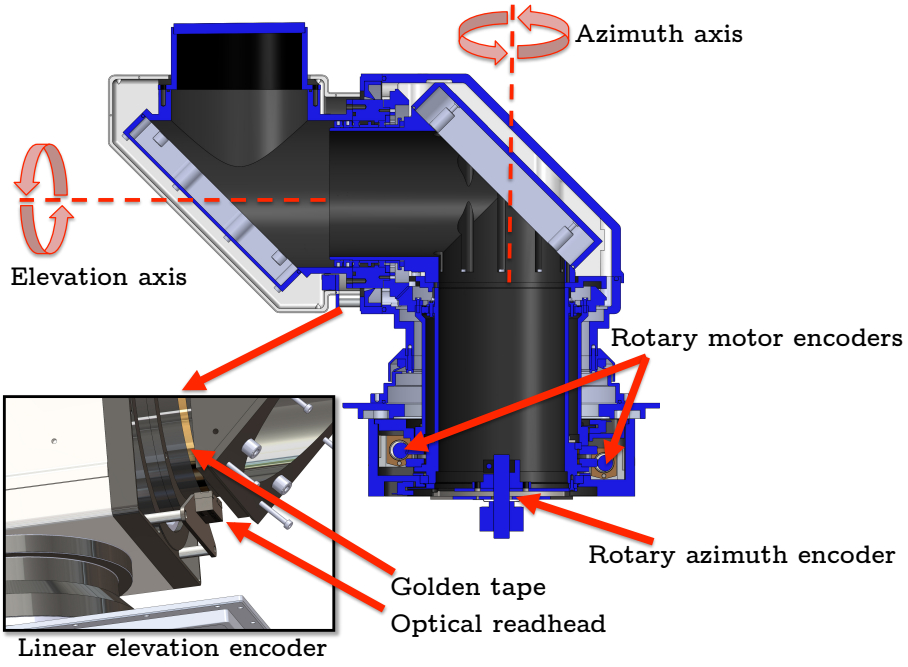

Figure 4.4: Encoders positions

The scanner head positioning accuracy tests consisted of the scanner head

rotation for the full range of positions around the azimuth and elevation axes, where the position readings were acquired from the motors' encoder and reference encoders and related to the commanded position. For the rotation around the azimuth axis, the scanner head was rotated in 10° incremental steps from 0° to 360° clockwise (positive rotation), and anticlockwise (negative rotation) from 360° to 0° with the maximum speed of 50°/s and maximum acceleration of $100°/s^2$ by holding the elevation angle equal to zero. After each incremental step the scanner head position was taken from the motor encoder and the reference encoder, and subtracted from the commanded value. These calculations resulted in the servo errors calculated using the position readings from the motor and reference encoder.

The servo error calculated using the position readings from the motor encoder was close to zero for both clockwise and anticlockwise rotation (Figure 4.5). However, the servo error calculated using the position readings from the reference encoder showed that the error was much larger, and for some domains of the azimuth angles reached the value of 0.1°. This indicated the presence of mechanical imperfections, but also that these imperfections cannot be seen from the position measurements from the motor encoder. Moreover, there are differences between the servo errors calculated for the clockwise and anticlockwise rotation. Differences exist since in the clockwise rotation the backlash is taken out, while in the opposite direction the backlash reemerges.

The same test was carried out for the elevation axis for a range of angles, from 0° to 180°. Similar to the case of the rotation around the azimuth axis, the servo error calculated using position measurements from the motor encoder tended to zero, while the servo error calculated using the elevation encoders indicated that the scanner head was positioned with errors, with the maximum of 0.025° (Figure 4.6). Once again, the following errors in the positive and negative directions differed due to the presence of backlash.

In comparison to the azimuth axis, the servo error for the elevation axis was significantly smaller. Possible explanations for this phenomenon are:

- Lower load on the elevation motor
- Higher precision of the manufactured components that provide the rotation around the elevation axis

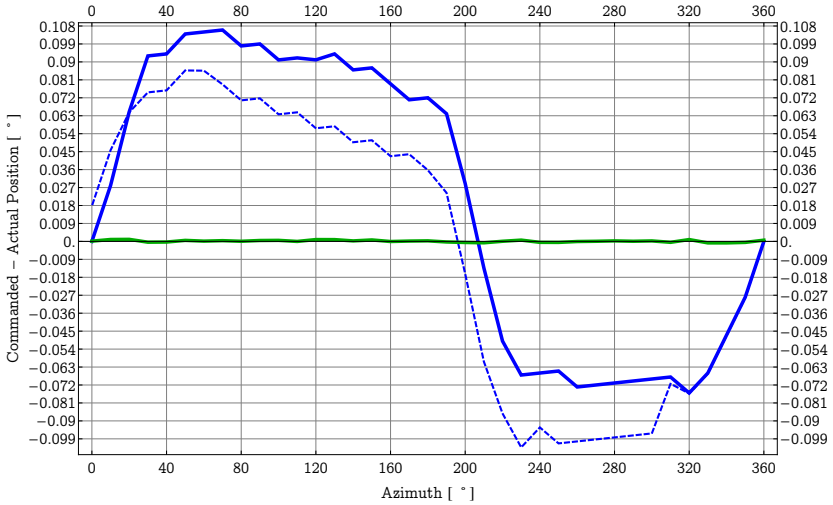

Figure 4.5: Averaged bidirectional servo error for the azimuth axis. **The green line** is the bidirectional servo error calculated using the motor encoder, **the blue solid and dashed lines** are the servo errors acquired using the reference encoder for the clockwise and anticlockwise rotations respectively.

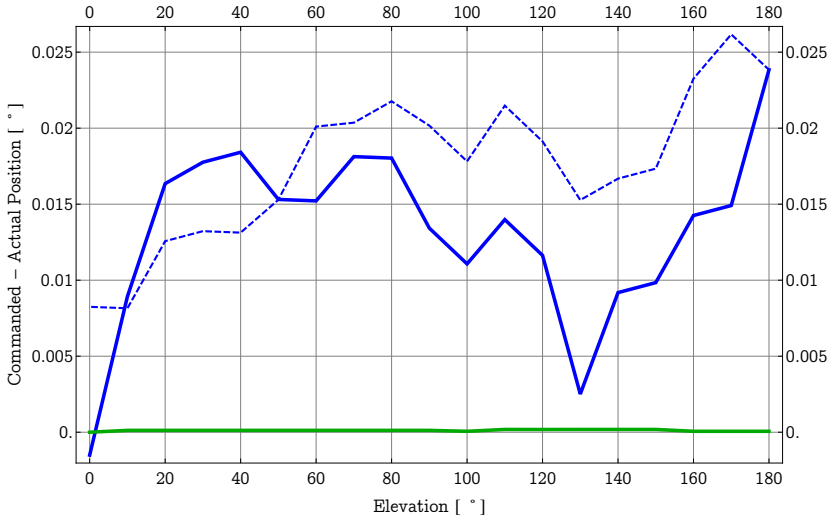

Figure 4.6: Averaged bidirectional servo error for the elevation axis. **The green line** is the bidirectional servo error calculated using the motor encoder, **the blue solid and dashed lines** are the servo errors acquired using the reference encoder for the clockwise and anticlockwise rotation respectively.

4.2.3 Reducing the contribution to the uncertainty

The previous tests showed that the motion controller is unable to compensate for the mechanical imperfections and the backlash since the position readings from the motor encoders do not provide the necessary information. However, the WindScanner motion controller allows the incorporation of compensation tables for mechanical imperfections and backlash. The compensation table for mechanical imperfections is formed by recording the servo error acquired by the position readings from the reference encoder in the backlash-free direction into the motion controller. Similarly, the compensation table for the backlash is formed by recording the difference between the servo error in the clockwise and anticlockwise directions (backlash-free and backlash direction) into the motion controller.

These two compensation tables represent two additional controls in the control loop which, based on the commanded position and the direction of the rotation, either add or subtract the value from the control signal (Figure 4.7). Both controls have to be present in the control loop, since the presence of only the mechanical imperfections control gradually reduces the servo error in the backlash-free direction, while in the opposite direction the servo error is less reduced. This can be observed for the both rotational axes (Figure 4.8 and 4.9).

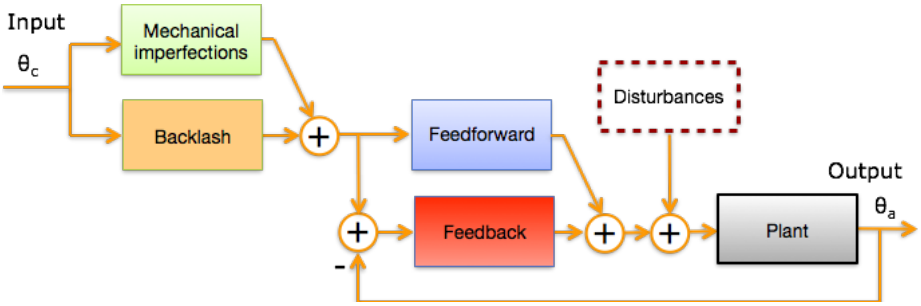

Figure 4.7: Block diagram of the control loop for the azimuth axis extended with the mechanical imperfections and the backlash control

By extending the control loop with the mechanical imperfections and backlash control, the tracking performances are significantly improved, as for some domains of the azimuth angles, the servo error is reduced up to 5 times, i.e. from the servo error of the 0.1° to the servo error of 0.02°. Similarly, after adding the mechanical imperfection and backlash control for the elevation axis, the servo error is reduced up to three times for the whole range of elevation angles.

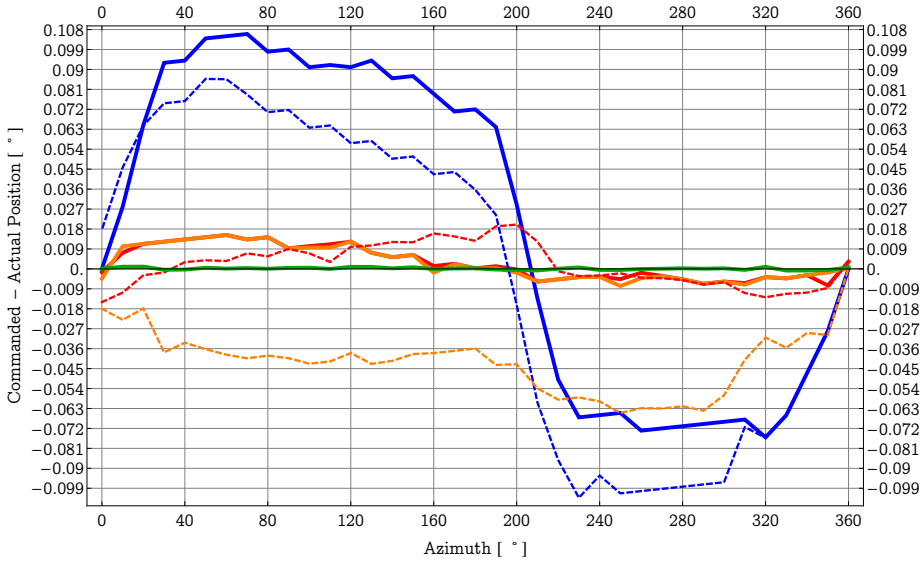

Figure 4.8: Averaged bidirectional servo error for the azimuth axis. **The green line** is the bidirectional servo error calculated using the motor encoder, **the blue solid and dashed lines** are the servo errors acquired using the reference encoder for the clockwise and anticlockwise rotation respectively, **the orange solid and dashed lines** are the servo errors acquired after adding the mechanical imperfection control, and **the red solid and dashed lines** are the servo errors acquired after adding the mechanical imperfection and backlash control.

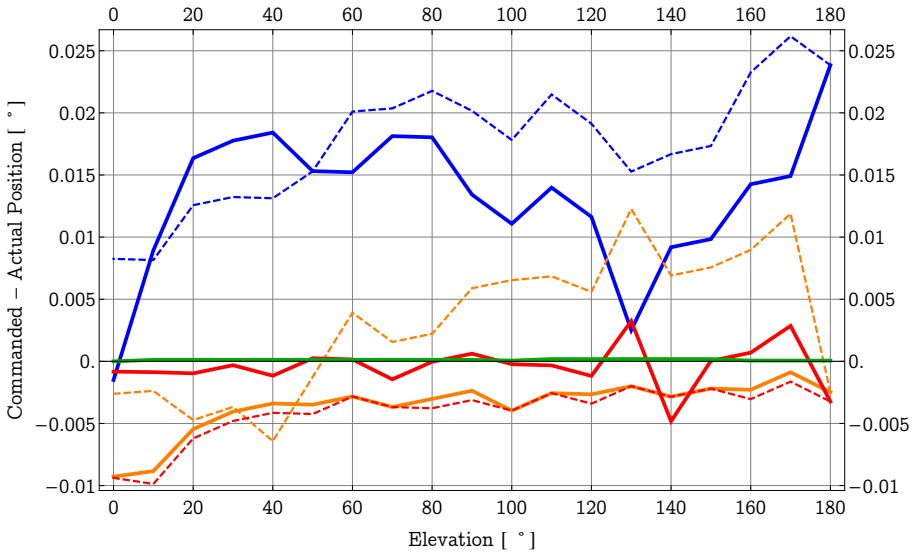

Figure 4.9: Averaged bidirectional servo error for the elevation axis. **The green line** is the bidirectional servo error calculated using the motor encoder, **the blue solid and dashed lines** are the servo errors acquired using the reference encoder for the clockwise and anticlockwise rotation respectively, **the orange solid and dashed lines** are the servo errors acquired after adding the mechanical imperfection control, and **the red solid and dashed lines** are the servo errors acquired after adding the mechanical imperfection and backlash control.

4.3 Scanner head connection with the casing

4.3.1 Spring connection

The scanner head is located on an L-profile rigidly connected to the supportive frame carrying the lidar computer and optical elements (Figure 4.10). One part of the L-profile rests on the frame which carries the motion controller. Both frames are connected with the WindScanner casing, using springs located in the corners of the frames. The only direct connection of the scanner head with the casing is through a metal frame that presses the rubber part of the scanner head to the casing. This part covers the casing hole through which the scanner head is installed on the WindScanner. The spring connection is used to avoid damages of the sensitive internal components during the WindScanner transportation.

Since different positions of the scanner head will have different distribution of mass around the axes of the rotation, this will result in the scanner head position dependent center of gravity. Due to the non-rigid connections of the scanner head and frame with the casing, the center of gravity position change will result in deviations in six degrees of freedom (6DoF) of the actual position of the scanner head and frame from the expected fixed position. These deviations will introduce changes in the expected laser beam direction.

Translation has only a second order effect since the deviations in all three axes are probably within a centimeter range. Deviations in the remaining three degrees of freedom (3DoF) in rotation will introduce the angular displacement in the expected laser beam direction.

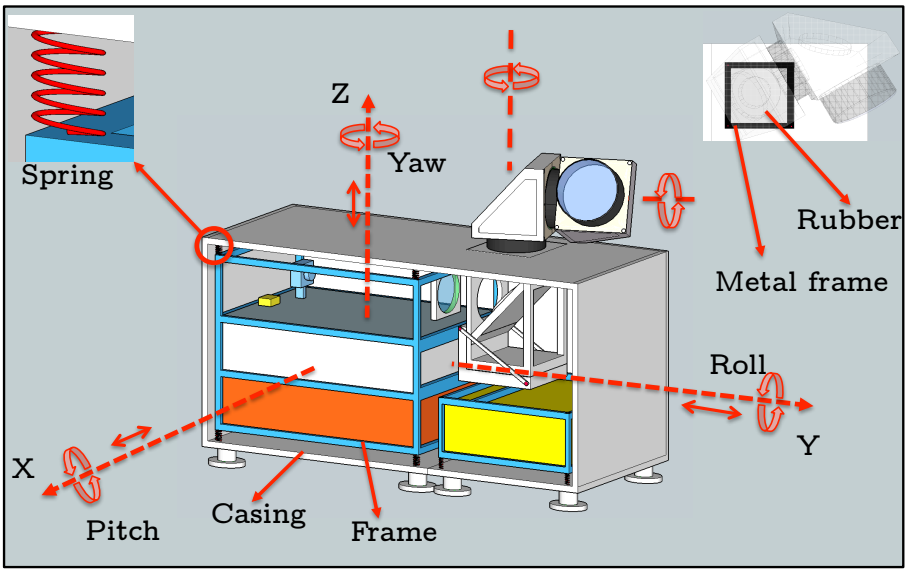

Figure 4.10: The influence of the rotation of the scanner head on the positioning accuracy

4.3.2 Testing procedure

The accuracy of the current WindScanner dual-axis inclinometer and compass is 0.5° with the resolution of 0.1°. These features are poor and prohibit the assessment of the deviations in 3DoF of rotation. Also, the motors and other electronic components create a magnetic field which further decreases the accuracy of the compass. For these reasons, in order to assess the deviations, a visible laser light was emitted from a laser attached to the bottom of the scanner head, and the reflection point of this light was tracked and marked for four different positions of the scanner head on a white board 39 m away from the laser (Figure 4.11, 1). Two different mountings of the laser were used for the assessment. For the first mounting, the laser emitted the light parallel with the longer side of the WindScanner (Figure 4.11, 2), while for the second mounting, the light was emitted perpendicular to the longer side (Figure 4.11, 3).

In order to estimate the deviations of the scanner head and the frame in 3DoF of rotation, it was assumed that the difference in position of the reflection point on the vertical axis of the white board was caused by the rotation of the scanner head and frame around the Z axis (the yaw of the scanner head and frame, Figure 4.10). The difference in position on the horizontal axis of the white board was the result of the rotation of the scanner head and the frame around the X axis (the pitch of the scanner head and frame, Figure 4.10) for the first mounting, and rotation around the Y axis (the roll of the scanner head and frame, Figure 4.10) for the second mounting.

With these interpretations of the differences among positions of the reflection point, it has been calculated that the scanner head and frame yaws for ±0.007°, pitches± 0.033° and rolls ±0.052° taking into account the maximum differences on the horizontal and vertical axes of the white board (Figure 4.12).

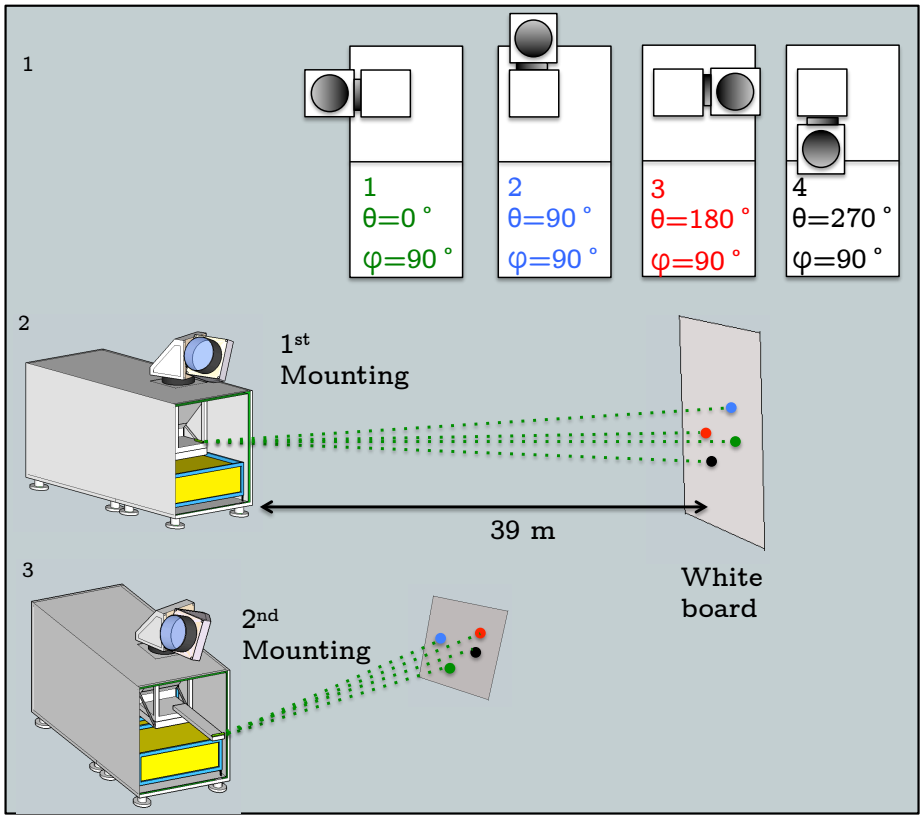

Figure 4.11: 1 - Four different positions of the scanner head. The position of the scanner head around the elevation axis is kept constant to 90°. The scanner head was rotated around the azimuth axis with the incremental steps of 90°. 2 - The first mounting of the laser for which the light was emitted in parallel/parallel to with the longer side of the WindScanner. As the scanner head rotated the reflection point on the white board took different positions. Four different markings on the white board represent the position of the reflection point for four different scanner head positions. 3 - The second mounting of the laser for which the light was emitted perpendicular to the longer side of the WindScanner.

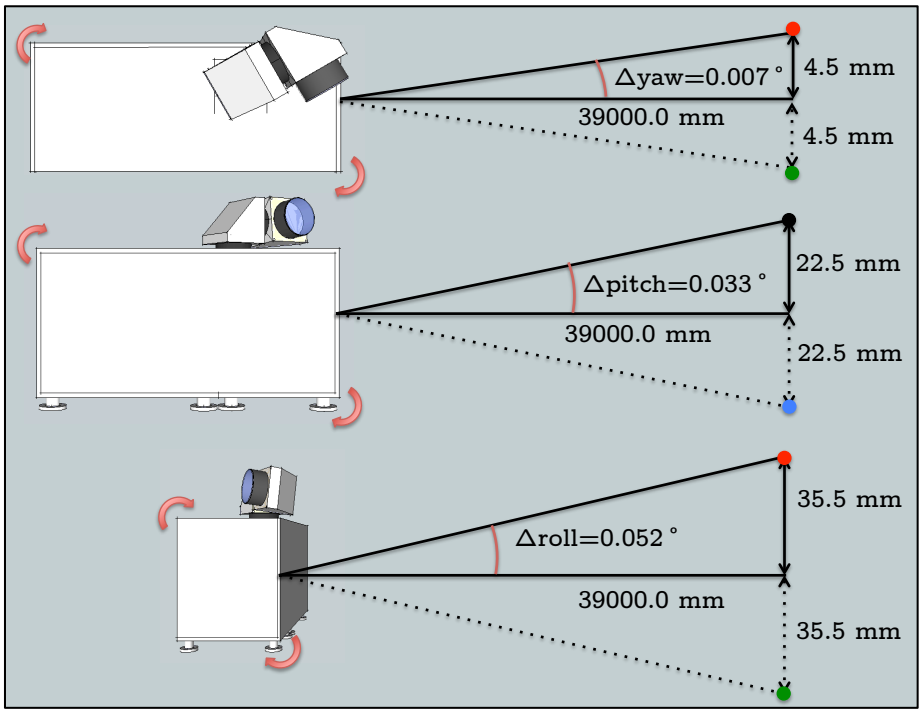

Figure 4.12: The maximum yawing, pitching, and rolling of the scanner head and frame due to the rotation of the scanner head and the scanner head - frame connection to the casing.

4.3.3 Reducing the contribution to the uncertainty

A mechanical locking system should be developed, one that would allow smooth operation of the springs during the WindScanner transportation and a rigid connection of the supportive frame with the casing during the measurements. In order to monitor if the locking system functions properly during the measurements, a dual-axis inclinometer with the accuracy higher than 0.1° and appropriate resolution should be installed at the bottom of the scanner head.

4.4 Home position

4.4.1 Definition of the home position

Home position of the long-range WindScanner represents the starting position of the scanner head rotation. In this position, the scanner head directs the laser beam parallel to the ground and parallel to the South - North line (Figure 4.13), under the assumption of a flat Earth.

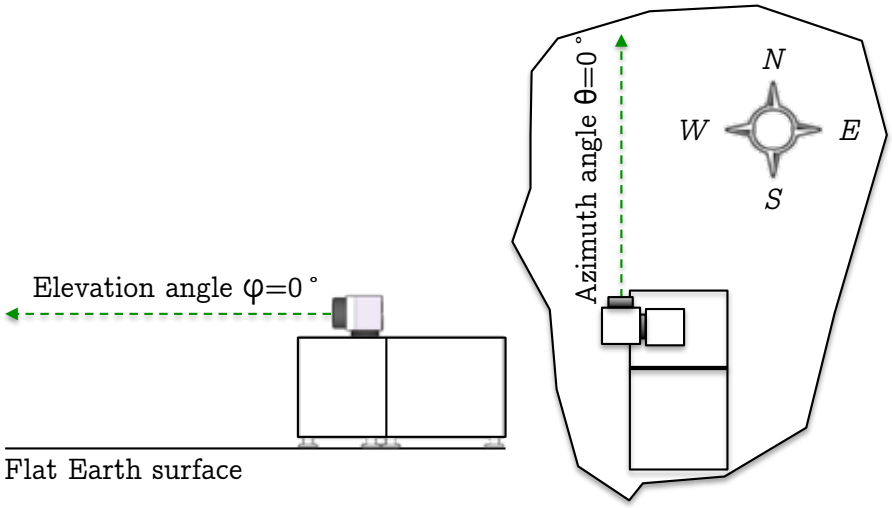

Figure 4.13: Home position of the long-range WindScanner.

The indoor calibration of the home position is done using a handheld laser distancemeter equipped with an inclinometer that has the accuracy of ±0.1° (Figure 4.14). For the optimization of the home position for the elevation axis, the distancemeter is placed on the scanner head part that rotates around it. By rotating the scanner head around the elevation axis, the inclination angle is checked, and once it is equal to zero, the position of the scanner head for the elevation axis is recorded in the motion controller's homing programable logic controller (PLC). This PLC positions the scanner head to the home position. In the case of the azimuth axis, the whole structure of the scanner head is laid on

its side in a way that allows the use of the distancemeter for the home position optimization for the azimuth axis. Similarly, the scanner head position for which the inclination angle is equal to zero is recorded in the homing PLC.

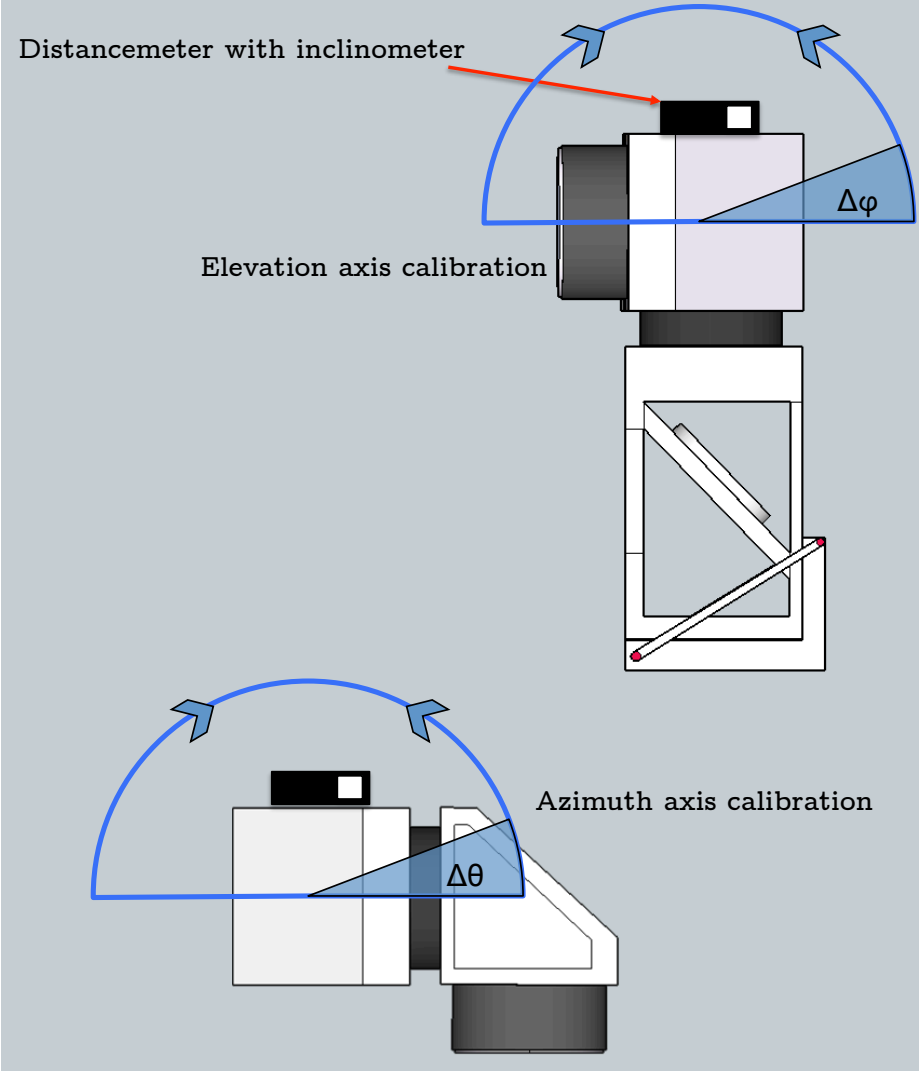

Figure 4.14: Indoor calibration of the home position

4.4.2 Testing procedure

After the WindScanner's installation for a measurement campaign, the actual home position has to be tested, since if this position does not comply with

the definition of the home position, the actual laser beam direction will have a constant angular offset in comparison to the expected laser beam direction. This will compromise the measurements of radial velocity at the expected locations in the atmosphere.

The testing can be done using CNR mapper (see Appendix A). This software forms georeferenced images of the surrounding hard targets (i.e. non-transparent objects), which allow the determination of the hard targets positions in relation to the WindScanner. This information can be used to improve the accuracy of the home position.

The current procedure for the home position testing consists of the following steps:

1. Using a differential GPS, the position of the scanner head top is acquired in the form of X,Y and Z coordinates in the UTM coordinate system (Figure 4.15).

2. One hard target is installed at a typical distance of $D = 100$ m from the WindScanner, or relatively close to the location where the radial velocity measurements will take place. A 5-cm thin surveying stake is used for the hard target. The position of the hard target top is obtained with differential GPS.

3. Using the positions of the scanner head and hard target top, the expected azimuth and elevation angles are calculated for which, if the actual home position comply with the nominal home position, the laser beam of the WindScanner would in turn direct the laser beam to target the hard target top.

4. Using CNR mapper the top is found and the actual azimuth and elevation angles of the scanner head are extracted (Figure 4.16).

5. The expected and actual azimuth and elevation angles are compared, and the offsets for the azimuth and elevation angles are calculated.

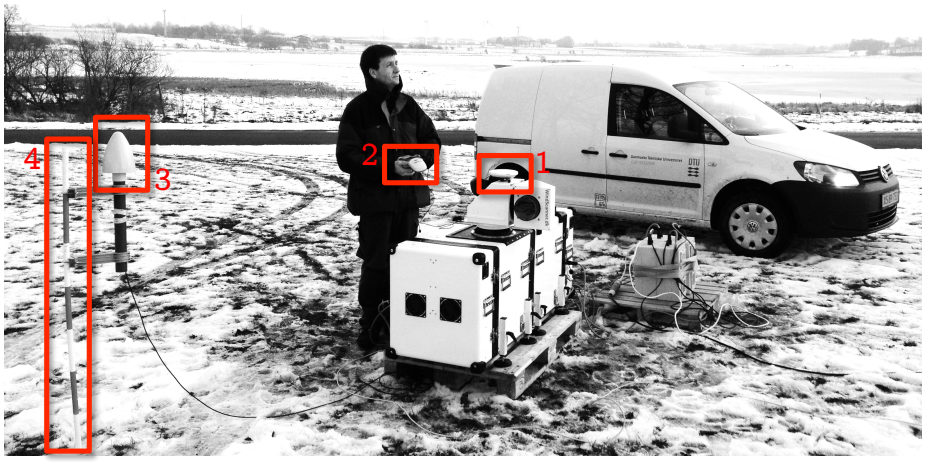

Figure 4.15: 1 - Differential GPS antenna, 2 - Differential GPS, 3 - GPS clock athenna and 4 - Surveying stake

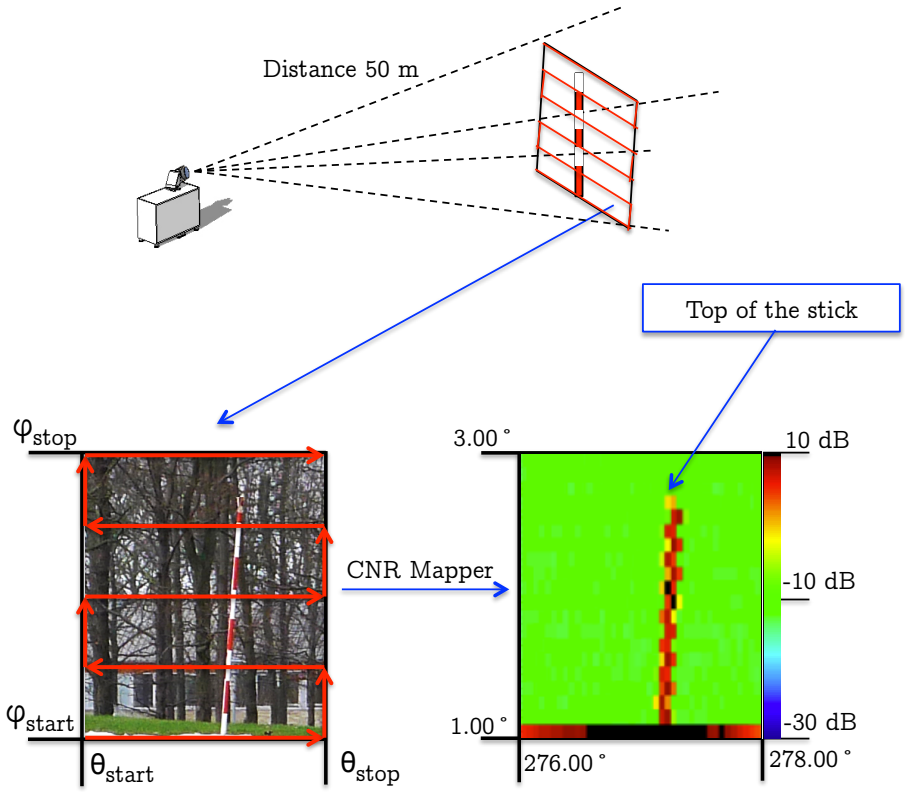

Figure 4.16: Extraction of the azimuth and elevation angles of the hard target top.

4.4.3 Reducing the contribution to the uncertainty

The offsets calculated during the home position testing are introduced in the homing PLC. Introducing the offsets in the homing PLC results in the home position that complies with the above described home position definition.

It should be noted that the calculation of the offset has uncertainties related to the calculation of the expected and actual azimuth and elevation angles. The calculation uncertainty of the expected angles originates from the accuracy of the differential GPS (u_{GPS}=0.02 m for each coordinate), while for the actual angles the uncertainty originates from the CNR mapper's resolution which is $\pm 0.001°$. The combined uncertainty for the calculation of the home position offsets is given as the summation in quadrature of the expected and actual angles uncertainty:

$$\begin{aligned} u_{\theta_{home}} = u_{\varphi_{home}} &= \sqrt{u^2_{expected} + u^2_{actual}} = \\ &= \sqrt{\left(\arcsin \frac{\sqrt{2}u_{GPS}}{\sqrt{2u^2_{GPS} + D^2}}\right)^2 + 0.001^2} = \\ &\approx \arcsin \frac{\sqrt{2}u_{GPS}}{D} \end{aligned} \tag{4.1}$$

The uncertainty is below $\pm 0.01°$ for the distances between the hard target and the WindScanner larger than 200 m.

4.5 Leveling

4.5.1 Testing procedure

Due to poor accuracy and resolution of the internal inclinometer, the leveling of the WindScanner performed using the measurements from this sensor, introduced a large uncertainty in the expected laser beam direction. Until the replacement of the inclinometer, the leveling is done using a handheld laser distance meter equipped with an inclinometer that has the accuracy of $\pm 0.1°$. During the leveling, the distance meter is placed at the bottom of the scanner head, at the position of the optical bench. Once the leveling is done and the homing PLC updated, the leveling is checked using the procedure identical to the home position testing, where a few extra hard targets are installed around the WindScanner. The minimum number of extra targets is two, under the assumption of perfect alignment of optical components.

If the leveling is done properly, the offsets among the targets will be equal and tend to zero. Otherwise, if the leveling is faulty, the offsets among these targets will be different. Again, the calculation of the offsets has the uncertainty identical to the uncertainty of the home position testing.

4.5.2 Reducing the contribution to the uncertainty

In cases of faulty leveling, there are two possible solutions that can reduce the impact on the expected laser beam direction. The first solution includes iterative optimization of the WindScanner leveling, until the offsets calculated in the leveling test show acceptable level defined by the user. The second solution consists of the derivation of a coordinate system for the scanner head positioning, based on the calculated offsets, that compensates for the presence of the faulty leveling

4.6 Mounting of mirrors

4.6.1 Conditions for the perfect laser beam steering

In order to assess only the influence of the mounting of the mirrors on the pointing accuracy, it will be assumed that:

- The axes of the rotation of the scanner head are perpendicular to each other
- The scanner head is positioned without following errors
- The reflection of the laser beam from the mirrors' surface follows the law of reflection

Under these assumptions of precise directing of the laser beam towards the points of interest in the atmosphere using the scanner head, the mounting of the mirrors has to provide an optical path that fulfills the following conditions depicted in Figure 4.17:

1. The part of the laser light path, from the first reflection point on the surface of the first mirror, to the second reflection point on the surface of the second mirror, has to coincide with the azimuth axis of rotation
2. The part of the path of the laser light from the second reflection point to the third reflection point on the surface of the third mirror has to coincide with the elevation axis of rotation
3. The second reflection point coincides with the intersection of the azimuth and elevation axes
4. The part of the path of the laser light from the third reflection point (the origin of the laser beam) towards the atmosphere has to be perpendicular to the elevation axis and to be in a plane formed by the three reflection points

These conditions dictate optimum values for the mounting parameters, i.e. a mirror position and orientation.

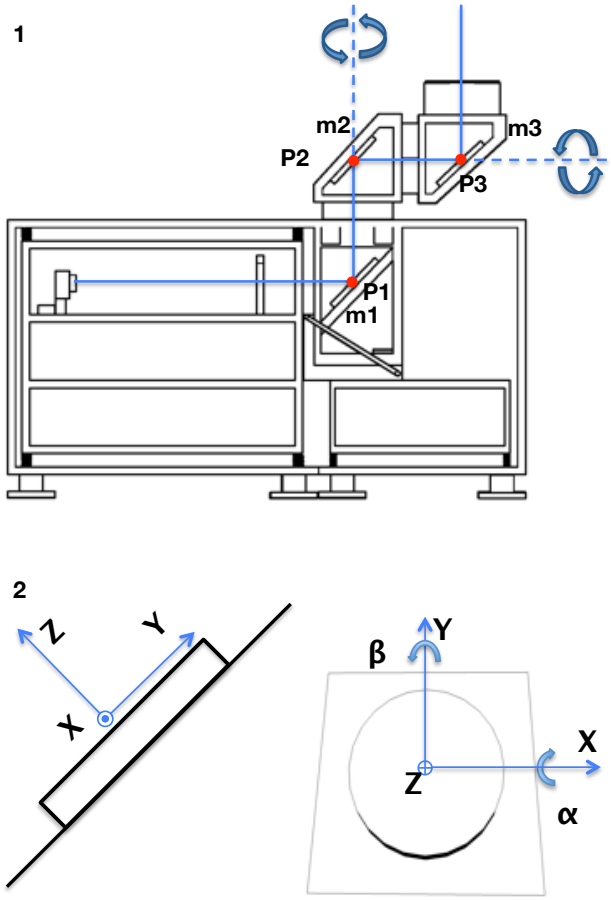

Figure 4.17: 1 - The optical path through the WindScanner towards the atmosphere. The point P_1, P_2 and P_3 are the reflection points at the mirrors m_1, m_2 and m_3. The axes of rotation are perpendicular one respect to the other. 2 - The coordinate system of a mirror. The mirror surface is part of the plane formed by X and Y axes. The Z axis is perpendicular to the mirror surface.

4.6.2 Violation of the conditions

During the mounting of the mirrors, the mirrors' position and orientation can deviate from the optimum values in 6DoF, with respect to the mirror coordinate system (Figure 4.17). However, not all 6DoF have a significant effect on the accuracy of the laser beam direction.

The translation in three perpendicular axes has a second order effect on accuracy, since the actual position of the laser beam at any distance from the scanner head will be offset from the expected position by a few centimeters. This means that there will be no angular displacements in the beam direction. Therefore, the first two conditions for the perfect mounting of the mirrors can be relaxed by ensuring that the parts of the path are parallel with the axes of rotation of the scanner head, and not necessarily coinciding with them.

For the remaining 3DoF in rotation, rotation around the Z axis will introduce neither translation of the beam nor the angular displacement in the beam direction (Figure 4.17, 2). However, the remaining two degrees of freedom in rotation will introduce an angular displacement of the laser beam direction. Consequently, the expected laser beam direction, given with the commanded azimuth and elevation angles of the scanner head, will be changed. The actual azimuth and elevation angles will deviate from the commanded angles as the functions of the angular displacements around the X and Y axes of each mirror and scanner head position (see Appendix B):

$$\begin{aligned}\theta_a = \theta_c &\pm (\cos(\varphi_c)\alpha_3 + \cos(\varphi_c)\cos(\theta_c)(\alpha_2 + \alpha_1)) \\ &\pm \sin(45°)(\sin(\varphi_c)\beta_3 + \sin(\varphi_c)\sin(\theta_c)(\beta_2 + \beta_1))\end{aligned} \tag{4.2}$$

$$\begin{aligned}\varphi_a = \varphi_c &\pm (\sin(\varphi_c)\alpha_3 + \sin(\varphi_c)\sin(\theta_c)(\alpha_2 + \alpha_1)) \\ &\pm \sin(45°)(\cos(\varphi_c)\beta_3 + \cos(\varphi_c)\cos(\theta_c)(\beta_2 + \beta_1))\end{aligned} \tag{4.3}$$

where indices a and c relate to the actual and commanded (i.e. expected) values of the azimuth (θ) and elevation (φ) angles of the laser beam direction.

4.6.3 Testing procedure

In order to estimate the six angular displacements of the mirrors and their influence on the expected laser beam direction, a test identical to the leveling test should be performed, where at least additional six hard targets should be installed. This establishes the minimum number of nine hard targets that cover the home position, leveling and mirror alignment tests (Figure 4.18). The uncertainty of the estimation of angular displacements of the mirrors is equal to the uncertainty of the calculation of the home position offsets and pitching and rolling for the leveling.

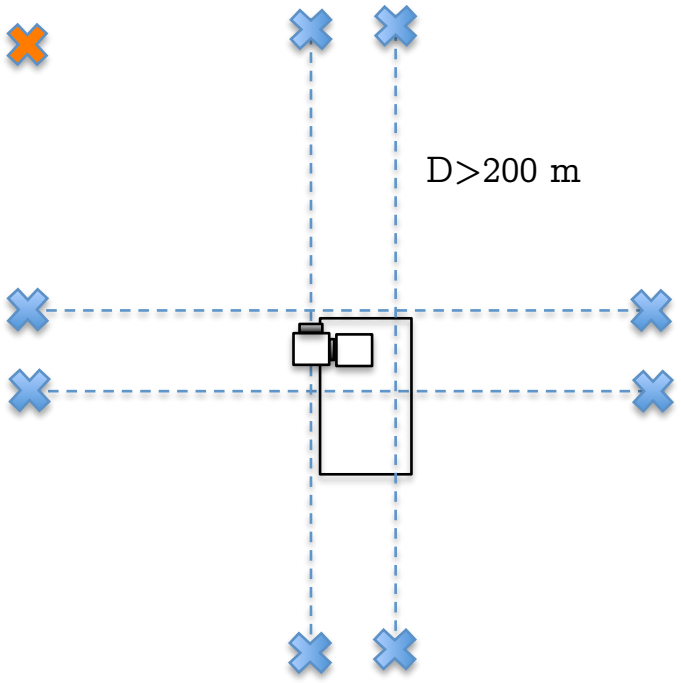

Figure 4.18: A suggestion for locating hard targets around the WindScanner. The orange hard target corresponds to the target according to which the initial home position is optimized. Other eight hard targets are used to test the leveling and alignment of the mirrors.

4.6.4 Reducing the contribution to the uncertainty

The test with nine hard targets provides the means to optimize the home position and compensate for the faulty leveling and angular displacements of the mirrors. The compensation for the faulty leveling and angular displacements of the mirrors implies formation of one joint coordinate system for positioning the scanner head. This would compensate for both issues and provide the means to accurately direct the laser beam.

4.7 Sensing distance

To test the accuracy of the sensing distance, a procedure similar to the home position testing can be applied. In this case, the positions of the scanner head and hard target top should be used to calculate the expected distance between them. The hard target top can be found, and the azimuth and elevation angles of the scanner head extracted by using CNR mapper. After that, the following steps should be taken:

1. The WindScanner should be configured via CNR mapper to steer the laser beam to target the top of the hard target

2. CNR mapper should be configured to acquire CNR from multiple distances distributed along the laser beam, with the center of this distribution located around the calculated distance between the hard target and the scanner head top

3. The distance at which CNR has the maximum value should be extracted from the CNR curve. This represents the actual distance between the scanner head and hard target top (see Appendix A)

4. The difference between the actual and expected distances represent the offset in the sensing range (D_{offset}), which should be used to optimize a measurement scenario and remove the offset of the sensing distance

This proposed approach in deducing the sensing distance offset has the uncertainty linked to the distance acquisition between the scanner head and hard target top using the differential GPS and CNR mapper that can be expressed as the following:

$$\begin{aligned} u_D &= \sqrt{u_{GPS}^2 + u_{CNRmapper}^2} = \\ &= \sqrt{(\sqrt{(0.02m)^2 + (0.02m)^2})^2 + (\frac{0.6m}{2})^2} \approx \frac{0.6m}{2} = 0.3m \end{aligned} \tag{4.4}$$

where value of 0.6 m represents the resolution of CNR mapper (see Appendix A), while the term $\sqrt{(0.02m)^2 + (0.02m)^2}$ arises from the calculation of the distance using the differential GPS.

4.8 Total uncertainty estimation

Magnitudes of each uncertainty contribution and the estimated total uncertainty are given in Table 4.1. The table contains one column set related to the measured or approximated magnitudes (labeled 'without reduction'), and another set that represents the expected magnitudes if the procedures for reducing uncertainty are applied (labeled 'with reduction'). The estimated total uncertainty is calculated as the summation in quadrature of all contributions.

It should be noted that the contribution to the laser beam pointing uncertainty, which originates from the home position for the column set labeled 'without reduction', are set under the assumption of absolutely accurate orientation and leveling of the WindScanner for a measurement campaign. The magnitude of the contribution that originates from the mirror mounting has not been measured yet. However, in order to estimate total uncertainty, it has been assumed that the magnitude can be related to the maximum uncertainty of the laser beam direction of 0.080°, which is reported by Leosphere for

their ground-based vertical profiling lidars [83]. Furthermore, the influence of the spring connection of the scanner head and lidar casing on the laser beam pointing uncertainty has been simplified with the following relations:

$$u_\theta = \Delta yaw = 0.007^\circ \tag{4.5}$$

$$u_\varphi = Max(\Delta pitch, \Delta roll) = 0.052^\circ \tag{4.6}$$

Finally, the range of values for the sensing distance uncertainty in the column set labeled 'without reduction' is based on the sensing distance tests that have been performed during the Swinging Musketeer experiment.

	Without reduction			With reduction		
	$u_\theta[^\circ]$	$u_\varphi[^\circ]$	u_D[m]	$u_\theta[^\circ]$	$u_\varphi[^\circ]$	u_D[m]
Position readings	0.108	0.025	≈ 0	0.018	0.010	≈ 0
Spring connection	0.007	0.052	≈ 0	≈ 0	≈ 0	≈ 0
Home position	0.100	0.100	≈ 0	0.010	0.010	≈ 0
Leveling	0.500	0.500	≈ 0	0.010	0.010	≈ 0
Mirror mounting	0.080	0.080	≈ 0	0.010	0.010	≈ 0
Time of flight	0	0	5-12	0	0	0.3
Total	0.520	0.510	5-12	0.025	0.025	0.3

Table 4.1: Total uncertainty estimation

4.9 Probability cube

Previously estimated total uncertainty in the laser beam pointing can be used to define the probability cube, the dimensions of which define the volume of the atmosphere within which, for a given laser beam direction and a particular distance along the laser beam, we expect the acquisition of radial velocity with a 68 % probability. Let us consider that we are acquiring radial velocity from a distance of D=5 km along some laser beam direction. If the procedures for reducing the uncertainty are not applied, the dimensions of the probability cube are:

$$\begin{aligned} \Delta X &= D \sin u_\theta \approx 46\ m \\ \Delta Z &= D \sin u_\varphi \approx 46\ m \\ \Delta Y &= u_D = 5 - 12\ m \end{aligned} \tag{4.7}$$

If the procedures for reducing the uncertainties are applied, the dimensions of the probability cube are significantly reduced:

$$\begin{aligned} \Delta X &= D \sin u_\theta \approx 2\ m \\ \Delta Z &= D \sin u_\varphi \approx 2\ m \\ \Delta Y &= u_D = 0.3\ m \end{aligned} \tag{4.8}$$

4.10 Discussion

To the best of the author's knowledge, the study of the coherent Doppler scanning lidar laser beam pointing accuracy presented in this chapter is the most comprehensive work regarding this topic. The study proposed the tests for each studied source to uncertainty, procedures to reduce each source of uncertainty contributions, and it provided an estimation of total uncertainty.

However, the work regarding the laser beam pointing accuracy is still in its early stages. Not all the listed sources of uncertainty have been studied. Total uncertainty is roughly estimated, with a few assumptions, the one regarding the contribution of the mirror mounting probably being the most questionable.

A part of the future work should be focused on estimating the magnitude of the contribution of the mirror mounting to the total uncertainty. This would include the determination of the exact function that describes the influence of the angular displacements and scanner head position on the expected laser beam direction and the application of the proposed testing procedure. If the proposed testing procedure provides satisfying results, a complex coordinate system, which compensates for the presence of the angular displacements of the mirrors, should be formed and verified with the same testing procedure.

Regarding the positioning accuracy of the scanner head, the proposed tests should be extended by taking into account the kinematic coupling, and thus the interaction between the azimuth and elevation axes. This means that instead of treating the scanner head as a Single-Input-Single-Output (SISO) motion system, the scanner head should be treated as a Multiple-Input-Multiple-Output (MIMO) motion system. Also, it should be tested to what extent the reference sensor mounting affects the reference measurements of the scanner head position. In relation to this, it should be tested if the mechanical imperfections and backlash controls improve the positioning accuracy of the scanner head using the same testing procedure as the one proposed for the mirror alignment. If the obtained accuracy is not satisfactory, a design of the scanner head based on a direct drive solution should be considered. The direct drive solution would eliminate the gear box, improve the positioning accuracy of the scanner head and the control loop would be closed by the position readings from the load side. Moreover, the location where the motion is actuated and resulting position measured will be the same.

Furthermore, the scanner head and the frame should be connected rigidly with the casing of the WindScanner. The proposed dual-axis inclinometer should be installed at the bottom of the scanner head in order to measure angular displacements.

Finally, other sources of uncertainty, listed at the beginning of this chapter, should be studied, and their impact on the laser beam pointing accuracy determined.

Chapter 5

Swinging musketeer experiment

5.1 Introduction

In the Musketeer Experiment, using three spatially separated pulsed coherent Doppler lidars in a staring mode, the feasibility of the measurements of the fluctuating atmospheric wind velocity at one point was demonstrated for the first time [58]. The installation and the configuration of the three lidars allowed the intersection of their laser beams at a single point 78 m above the ground level, close to a sonic anemometer. The time series of the wind velocity made with the sonic anemometer and the three lidars show generally very good correlation [59]. This experiment represented the starting point of the realization of both the short-range and the long-range WindScanner systems, which are able to perform the same measurements as the three lidars from the Musketeer Experiments, though at many points in the atmosphere.

The Swinging Musketeer experiment was done in order to demonstrate the completion of the development of the long-range WindScanner system and this Ph.D. project. The Swinging Musketeer Experiment was the first measurement experiment with the long-range WindScanner system, for which three WindScanners were used. The experiment took place at DTU Risø campus in late February 2013. The ambitions for this experiment were to test how well the long-range WindScanner system operates in an outdoor environment, and also to demonstrate the system's ability to measure the wind velocity at multiple points in the atmosphere using three synchronized WindScanners.

The plan was to measure the wind velocity close to three sonic anemometers installed on a 125-meter mast and to compare the long-range WindScanner system with the sonic anemometers measurements. At that time, but also at the time of writing this thesis, there was no published material that reported about an experiment in which three coherent Doppler lidars were used to synchronously measure the wind velocity at more than one point in the atmosphere.

Also, the Swinging Musketeer Experiment demonstrated the first synchronized multiple scanning Doppler lidar system in the world at that time.

5.2 Layout of the campaign

DTU Risø campus is located 5 km north of Roskilde, which lies on the island of Zealand, Denmark (Figure 5.1). Within the campus facilities, there is a 125-meter tall meteorological mast. The mast is equipped with various sensors that are attached to booms at different heights and directions. In this particular instance, for the Swinging Musketeer Experiment, measurements from the sonic anemometers that were attached to booms oriented to a direction of 345° at heights of 76, 94 and 118 m were used.

The mast is located on a hillock of a small peninsula. Tall trees and buildings dominate the surroundings of the mast, with water-coast transitions from North, West and South. Irrespective of wind directions, the site is inhomogeneous and can be considered as quite complex. Therefore, the location was not ideal for the wind speed calibration of lidars. But was still chosen for the first measurement campaign since it is in the vicinity of the laboratory in which a major part of the development of the long-range WindScanner system took place, and since the main idea of the experiment was to demonstrate the completion of the system (Figure 5.1).

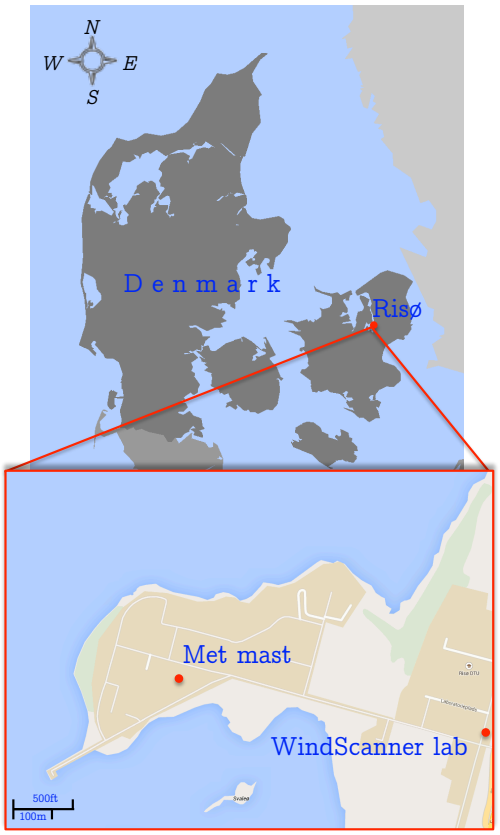

Figure 5.1: Location of the Swinging Musketeer Experiment.

Two factors limited the layout of the experiment. The first was the available space around the mast, and the second factor was the length of Ethernet cables, which were 100 m long. This is the maximum length of Ethernet cables for which the network signal amplifiers are unnecessary. With such restrictions the layout of the experiment shown in Figure 5.2 was proposed and used.

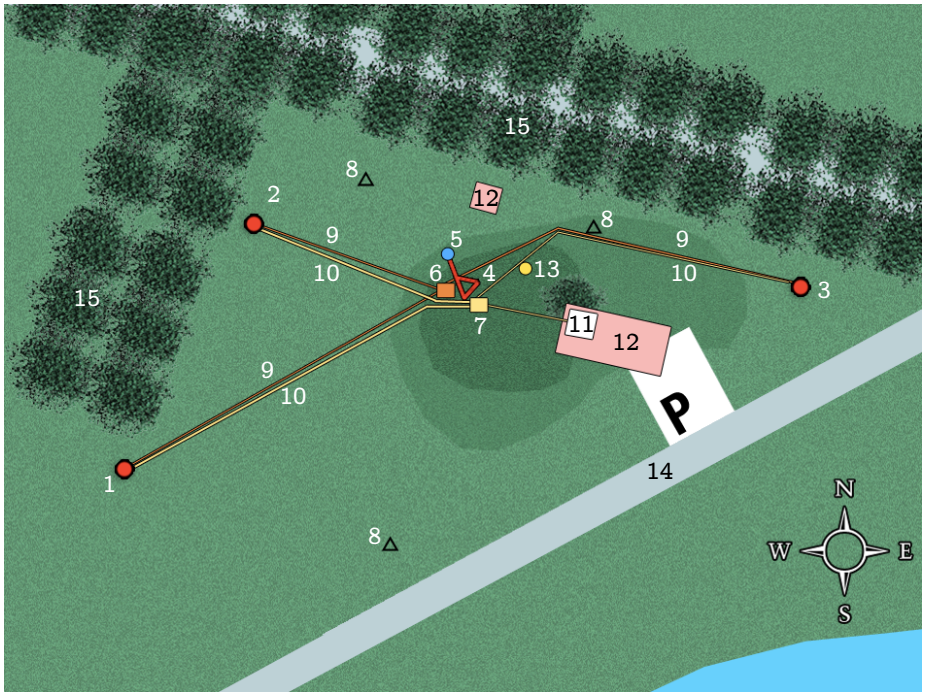

Figure 5.2: Layout of the experiment: 1 - WindScanner_1 , 2 - WindScanner_2, 3 - WindScanner_3, 4 - Base of the mast, 5 - Booms at 345° (projection on the ground level), 6 - Power socket, 7 - Ethernet switch, 8 - Mast's anchors, 9 - Power cables, 10 - Ethernet cables, 11 - Master computer, 12 - Laboratory buildings, 13 - Hard target (wooden stick), 14 - Access road, 15 - 20 m tall trees

5.3 Finding the sonic anemometers positions

Since the exact positions of the three sonic anemometers were unknown, the angles of the scanner heads for directing the laser beams, and the distances at which radial velocities should be measured were obtained through the following steps:

- The home position of each WindScanner was calibrated using the hard target located near the base of the mast and by following the procedure explained in Subsection 4.5.
- Georeferenced images of the upper part of the mast were made with each WindScanner, using CNR mapper (Figure 5.3).
- These images were used to determine the scanner heads positions which would in turn direct the laser beams approximately 20 cm above each sonic anemometer used in the experiment (Figure 5.3). This formed the measuring positions.

- Also, the georeferenced images were used to determine the scanner heads positions which would in turn direct the laser beams to target each sonic anemometer (Figure 5.3). This formed the hard target positions.
- Using the hard target positions and the procedure for the sensing distance calibration (Subsection 4.8), the distances between the sonic anemometers and the WindScanners were extracted (Figure 5.4).

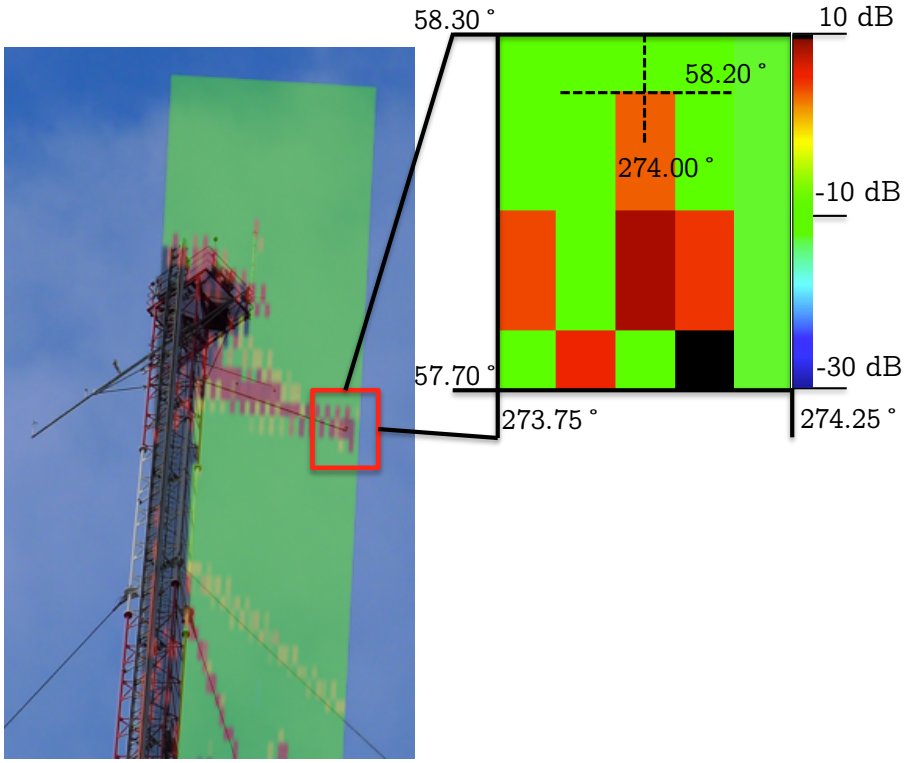

Figure 5.3: Finding the position of the sonic anemometer at 118 m height from the perspective of WindScanner_3 using CNR mapper.

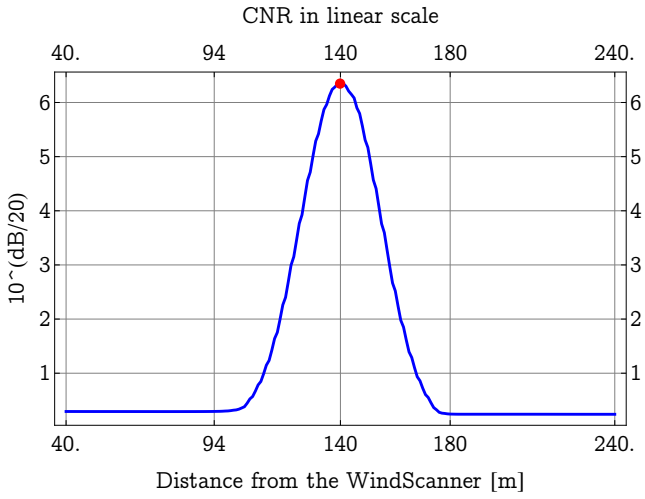

Figure 5.4: Finding the distance between the sonic anemometer at 118 m and WindScanner_3 using CNR mapper. The maximum value of CNR corresponds to the distance.

5.4 Measurement scenarios

In order to intersect beams at three points, three measurement scenarios were formed using the TeslaBlackBox subprogram of the WindScanner client software. The measuring positions and the distances were the necessary input parameters for the TeslaBlackBox subprogram. From these parameters the subprogram generated three synchronized CTD scenarios, where each scenario consisted of the motion program and the range gate file. The details about the scenarios are explained in the following text.

The initial part of the measurement scenarios, before entering the loop over the three points of the laser beams intersection, comprised the motions of the three scanner heads from their home positions to the positions where the three laser beams intersected 20 cm above the sonic anemometer at 118 m height (Figure 5.5). In order to keep the WindScanners synchronized, these motions were programmed to last 10 s for each WindScanner. Once the scanner heads reached the desired azimuth and elevation angles, the scanner heads would come to a standstill for one second. During this period laser pulses where emitted into the atmosphere and corresponding backscatter signals were acquired and processed, yielding the radial velocities for the point where the laser beams intersected 20 cm above the sonic anemometer at 118 m.

Following these radial velocity measurements, the scanner heads were rotated to the positions which would allow the laser beams to intersect at the point 20 cm above the sonic anemometer at 94 m (Figure 5.5). The rotations were programmed to last 0.5 s, taking into account the maximum speed and acceleration of the scanner heads of 50 $^\circ/s$ and 100 $^\circ/s^2$ respectively. Afterwards,

the emission and acquisition where performed while the scanner heads were at standstill over the course of one second, yielding the radial velocities for the second laser beams intersection point. The same steps were performed for the point 20 cm above the sonic anemometer at 76 m. The rotations of the scanner heads to the positions that will allow the laser beams to intersect were programmed to last 0.6 s, and radial velocities were acquired during the one second period. Following the third intersection point the scanner heads were rotated to the first point, where the programmed time was 0.7 s (Figure 5.5). Afterwards, the measurement scenarios continued to loop over the measurements of the radial velocities, at the points where the three laser beams intersected 20 cm above the three sonic anemometers, several hours.

The pulse type for this experiment was set to 'Long', which defines the laser pulses with the temporal length of 400 ns and the corresponding pulse shape and energy content. The pulses were emitted with the rate of 10 kHz, and the acquired backscatter signal was processed using the FFT size of 128 points.

The choice for the acquisition time of one second per intersection point and the 'Long' pulse type was made due to technical difficulties with one of the WindScanners.

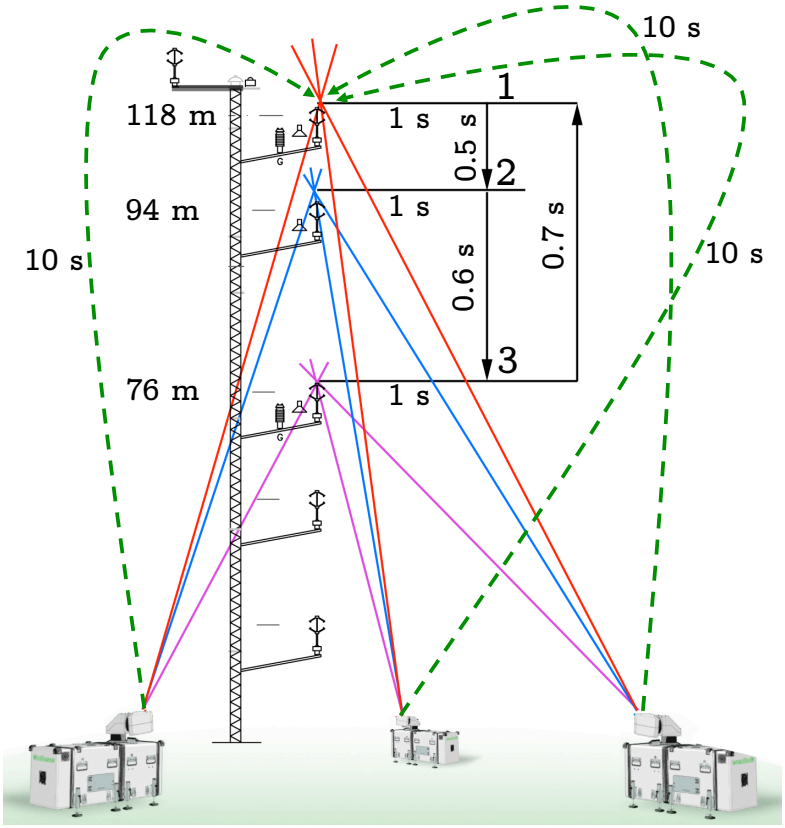

Figure 5.5: Swinging Musketeer experiment with three long-range WindScanners.

5.5 Analysis

5.5.1 WindScanners weighted average wind velocity vector

The radial velocities measured by the WindScanners, at the points where the laser beams were intersecting next to the three sonic anemometers, were used to derive weighted average components of the wind velocity, horizontal wind velocity and the wind direction, and to compare them with those measured by the three sonic anemometers. In the following text, details on the derivation process will be explained.

Firstly, it is assumed that the radial velocity V_r, measured by a coherent Doppler lidar at a certain distance d, can be expressed by an integration along the laser beam of the projected wind field u on the beam direction n:

$$V_r(d) = \int_{-\infty}^{+\infty} \Psi(s)\mathbf{n} \cdot \mathbf{u}(s\mathbf{n} + d\mathbf{n})ds \tag{5.1}$$

where $\mathbf{n}$ is a unit vector in the direction of the laser beam, and $\Psi(s)$ is the weighting function, normalized to a unit integral. The simplest way to determine the weighting function is by the convolution of the laser pulse shape and the time window profile.

In order to simplify the determining of the weighting function for the WindScanners, let us consider that they emit rectangular laser pulses with the spatial half length l equal to:

$$l = \frac{1}{2}\,\frac{c\,T_{pulse}}{2} = \frac{0.3\ 10^9 \frac{m}{s}\ 400\ 10^{-9} s}{4} = 60\ m \tag{5.2}$$

where c is the speed of light, and T_{pulse} is the temporal pulse length. For this particular experiment the temporal pulse length was set by the measurement scenarios to 400 ns.

It is assumed that no window function, such as the Hamming window, is applied on the time window samples. Therefore, the time window is not tapered, and thus the time window profile is rectangular. Based on the scenarios settings, the time window has the spatial length that matches the spatial length of the laser pulse, since the FFT size was set to 128 points, which corresponds to 512 ns, and approximately 154 m. With the assumptions and settings described above, the convolution of the pulse shape and the time window profile yields the weighting function that can be expressed as a triangular function:

$$\Psi(s) = \begin{cases} \frac{(l-|s|)}{l^2}, & \text{for } |s| < l, \\ 0, & \text{otherwise.} \end{cases} \tag{5.3}$$

Since the weighting function is equal to zero for the distance outside of $\pm\ l$ range, the integral from Equation 5.1 can be rewritten:

$$V_r(d) = \int_{-60\ m}^{+60\ m} \Psi(s)\mathbf{n} \cdot \mathbf{u}(s\mathbf{n} + d\mathbf{n})ds \tag{5.4}$$

This integral approximates the measurement process of the radial velocities by the WindScanners in the Swinging Musketeer experiment. It can be concluded that the measured radial velocity at certain distance d represents the average weighted sum of the radial velocities from a range of distances, centered at the distance d, which occupy the total probe length of 120 m. Therefore, the WindScanner and generally any pulsed coherent Doppler lidar, do not measure radial velocity at a point, but over the probe length defined by the laser pulse and time window characteristics.

Let us simplify the integral from Equation 5.4:

$$\begin{aligned} V_r(d) &= \mathbf{n} \cdot \int_{-60\ m}^{+60\ m} \Psi(s)\mathbf{u}(s\mathbf{n}+d\mathbf{n})ds = \\ &= \begin{bmatrix} -\sin\theta\cos\varphi \\ -\cos\theta\cos\varphi \\ \sin\varphi \end{bmatrix} \cdot \int_{-60\ m}^{+60\ m} \Psi(s) \begin{bmatrix} U(s\mathbf{n}+d\mathbf{n}) \\ V(s\mathbf{n}+d\mathbf{n}) \\ W(s\mathbf{n}+d\mathbf{n}) \end{bmatrix} ds = \\ &= \begin{bmatrix} -\sin\theta\cos\varphi \\ -\cos\theta\cos\varphi \\ \sin\varphi \end{bmatrix} \cdot \begin{bmatrix} U_{wa} \\ V_{wa} \\ W_{wa} \end{bmatrix} = \\ &= -\sin\theta\cos\varphi U_{wa} - \cos\theta\cos\varphi V_{wa} + \sin\varphi W_{wa} \end{aligned} \tag{5.5}$$

where θ and φ are the azimuth and elevation angles of the scanner head respectively, which defined the laser beam direction; U_{wa}, V_{wa} and W_{wa} are the weighted average components of the wind velocities that enter the probe length.

U_{wa} is the horizontal component towards East, while V_{wa} is the horizontal component towards North, and W_{wa} is the vertical component towards the sky. This definition of the components complies with the meteorological convention.

In the Swinging Musketeer experiment three independent radial velocities were measured at three points where the laser beams intersected. For those three intersection points the U_{wa}, V_{wa} and W_{wa} components can be calculated, if we assume that the wind field that enters the probe lengths is the same:

$$\begin{bmatrix} U_{wa} \\ V_{wa} \\ W_{wa} \end{bmatrix} = \begin{bmatrix} -\sin\theta_1\cos\varphi_1 & -\cos\theta_1\cos\varphi_1 & \sin\varphi_1 \\ -\sin\theta_2\cos\varphi_2 & -\cos\theta_2\cos\varphi_2 & \sin\varphi_2 \\ -\sin\theta_3\cos\varphi_3 & -\cos\theta_3\cos\varphi_3 & \sin\varphi_3 \end{bmatrix}^{-1} \cdot \begin{bmatrix} V_{r1} \\ V_{r2} \\ V_{r3} \end{bmatrix} \tag{5.6}$$

where, V_{r1} , V_{r2}, and V_{r3} are the radial velocities measured by WindScanner_1, WindScanner_2 and WindScanner_3 respectively at a point where the laser beams intersected, θ_1,θ_2 and θ_3 are the azimuth angles, and φ_1,φ_2 and φ_3 are the elevation angles of the WindScanner_1, WindScanner_2 and WindScanner_3 scanner heads used to steer three laser beams to intersect.

By calculating the U_{wa}, V_{wa} and W_{wa} components, the weighted average wind velocity for one intersection point has been described. The components U_{wa} and V_{wa} can be further used to derive the weighted average horizontal wind velocity $V_{h_{wa}}$ and the meteorological wind direction Θ_{wa}:

$$V_{h_{wa}} = \sqrt{(U_{wa})^2 + (V_{wa})^2} \tag{5.7}$$

$$\Theta_{wa} = mod(90^\circ - \arctan\frac{V_{wa}}{U_{wa}}, 360^\circ) \tag{5.8}$$

5.5.2 Sonic anemometer wind velocity

In comparison to pulsed Doppler lidars, a sonic anemometer measures all three components of the wind velocity, and the probe length of a sonic anemometer is approximately 0.2 m. This essentially means that the sonic anemometer measures in a point.

Due to the orientation of the sonic anemometers used in this experiment, the measured components of the wind velocity describe a slightly different coordinate system than the one defined by the U, V and W components. The sonic anemometers measure the horizontal component X of the wind velocity towards the azimuthal direction of 345°, the horizontal component Y component, perpendicular to the X component and towards East, and vertical component Z, identical to the component W.

For the purpose of comparison of the components of the wind velocities calculated using the radial velocities measured by the WindScanners, with those measured by the sonic anemometers, the components X, Y and Z are transformed to the U, V and W components:

$$\begin{bmatrix} U \\ V \\ W \end{bmatrix} = \begin{bmatrix} \sin\theta_s & \cos\theta_s & 0 \\ \cos\theta_s & -\sin\theta_s & 0 \\ 0 & 0 & 1 \end{bmatrix} \cdot \begin{bmatrix} X \\ Y \\ Z \end{bmatrix} \tag{5.9}$$

where, θ_s is equal to 345°. Also, these components are used to calculate the horizontal wind velocity V_h and the meteorological wind direction Θ using the same relations described by Equationv 5.7 and 5.8.

5.5.3 Measurement results

The Swinging Musketeer experiment ran for the last few days of February 2013 including March 1^{st}. During this period, around 20 hours of radial velocities data were collected using the WindScanners. In this section data collected in the last run of the measurement scenarios, which started on 1^{st} of March, are analyzed and compared with the sonic anemometers measurements for the same period.

This run lasted 6 hours, from 02:00 to 08:00. During this period the three WindScanners were synchronized in the steering of the laser beams and the radial velocity measurements. The maximum lag, or the time difference between the fastest and the slowest WindScanner, was 10 ms. The average lag was around 4 ms.

Using the previously described relations between the radial velocities and the weighted average wind velocity, the time series of the radial velocities collected in the last run were transformed to the time series of the weighted average wind velocity components, horizontal wind velocity and the wind direction for the three intersection points. The time series were then block averaged over one-minute periods.

Similarly, the time series of the wind velocity components measured by the three sonic anemometers were transformed to comply with the meteorological

convention, and the horizontal wind velocity and the wind direction were calculated using these new components. Once again the three sets of the time series were block averaged over one-minute periods.

The three sets of the time series of the wind velocity components U, V and W, horizontal wind velocity and the wind direction acquired with the WindScanners and the corresponding sonic anemometers are compared in Figure 5.6,5.7 and 5.8. The mean values of the U, V and W components, horizontal wind velocity and the wind direction for the 6-hour period measured by the WindScanners and the sonic anemometers for each height are given in Table 5.1, 5.2 and 5.3. Also, the mean differences between the WindScanners and the sonic anemometers values and the standard deviations of differences for the 6-hour period are shown in the same tables.

From Figure 5.6 - 5.8 it can be seen that the wind velocity components and the corresponding horizontal wind velocities along with the wind directions calculated on the basis of the WindScanners radial velocities, follow the trend of those calculated using the sonic anemometers measurements for the three intersection points. The standard deviation is lowest for the measurements at 76 meters height. As the height increases, the standard deviation also increases. Similar trend can be observed for the scatter of the linear regression plots, the scatter increases with height. A possible explanation for the increase in the standard deviation and scatter could be the difference in the measurement principles of sonic anemometers and lidars in relation to the experienced wind conditions.

If the mean values given in Table 5.1 - 5.3 are closely inspected it can be noticed that during the 6-hour period there was a presence of a high vertical wind shear and wind veer (i.e. directional change of the horizontal wind velocity with height). The difference in the horizontal wind velocity measured by the sonic anemometers at 76 and 118 m was about 1.5 ms^{-1}, while the difference in the wind direction for these two heights was 13°.

As the height of the measuring point increased, the laser beams became more vertical, and the shear induced difference in wind velocities within the probe lengths became greater.

	WindScanners	Sonic anemometer	Mean difference	Standard deviation of difference (σ)
U [m s^{-1}]	-5.58	-5.56	-0.02	0.11
V [m s^{-1}]	3.08	3.11	-0.03	0.14
W [m s^{-1}]	-0.19	-0.16	-0.03	0.07
V_h [m s^{-1}]	6.42	6.42	0.	0.15
Θ [°]	299.09	299.39	-0.3	0.98

Table 5.1: Mean values for the U, V and W components of the wind velocity, horizontal wind velocity V_H and the wind direction for the point of the laser beams intersection located 20 cm above the sonic anemometer at 76 m height.

	WindScanners	Sonic anemometer	Mean difference	Standard deviation of difference (σ)
U [m s^{-1}]	-5.64	-5.74	0.1	0.13
V [m s^{-1}]	3.96	4.12	-0.16	0.24
W [m s^{-1}]	-0.31	-0.22	-0.09	0.11
V_h [m s^{-1}]	6.95	7.11	-0.16	0.22
Θ [$^\circ$]	305.09	305.84	-0.75	1.24

Table 5.2: Mean values for the U, V and W components of the wind velocity, horizontal wind velocity V_H and the wind direction for the point of the laser beams intersection located 20 cm above the sonic anemometer at 94 m height.

	WindScanners	Sonic anemometer	Mean difference	Standard deviation of difference (σ)
U [m s^{-1}]	-5.93	-5.9	-0.03	0.15
V [m s^{-1}]	5.34	5.29	0.05	0.45
W [m s^{-1}]	-0.38	-0.38	0.	0.18
V_h [m s^{-1}]	8.04	7.96	0.08	0.37
Θ [$^\circ$]	311.87	311.9	-0.03	2.12

Table 5.3: Mean values for the U, V and W components of the wind velocity, horizontal wind velocity V_H and wind direction for the point of the laser beams intersection located 20 cm above the sonic anemometer at 118 m height.

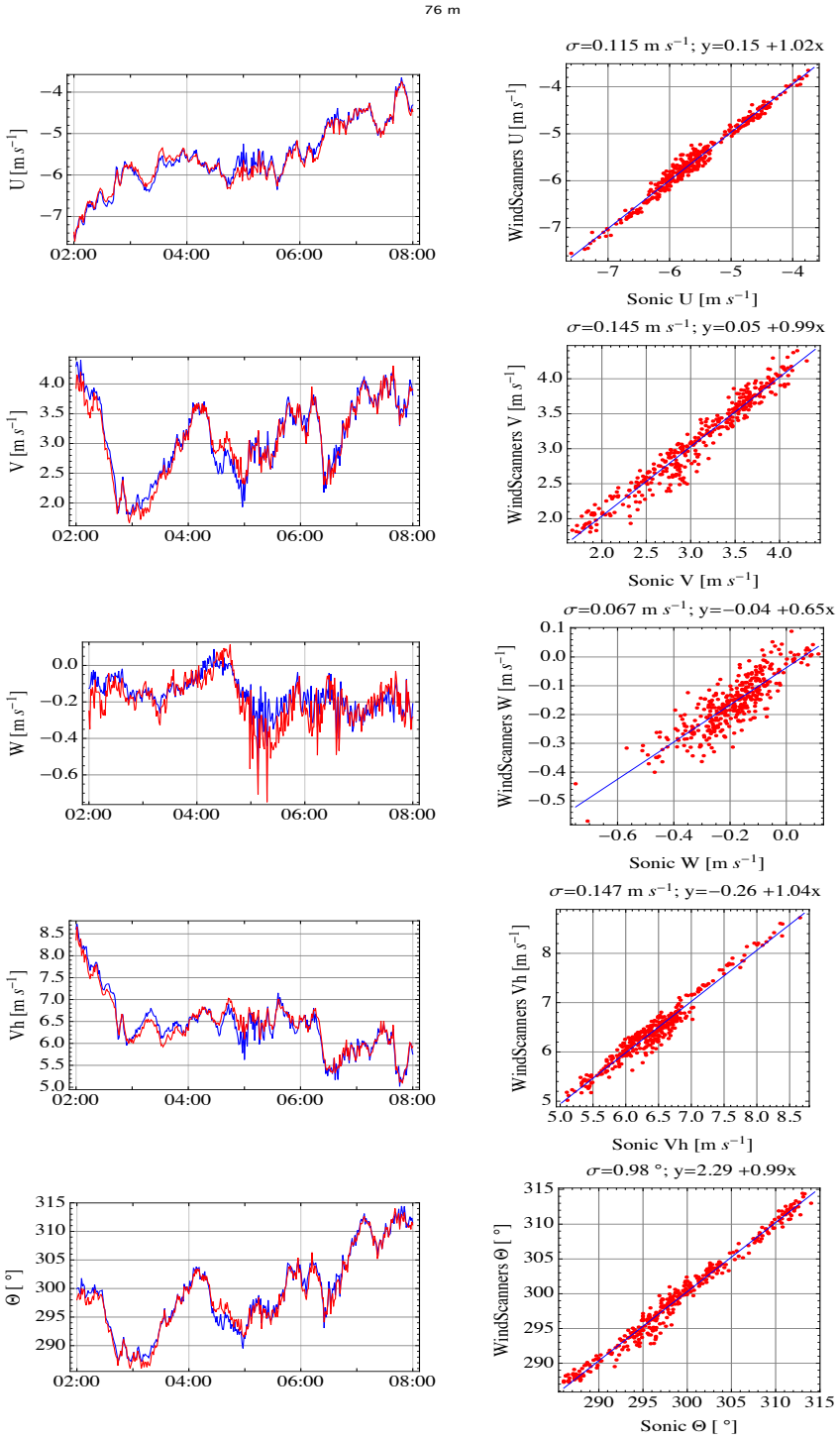

Figure 5.6: Measurements at 76 m. The blue curves are one-minute block averaged sonic anemometer measurements, while the red curves are one-minute block averaged measurements of the long-range WindScanner system.

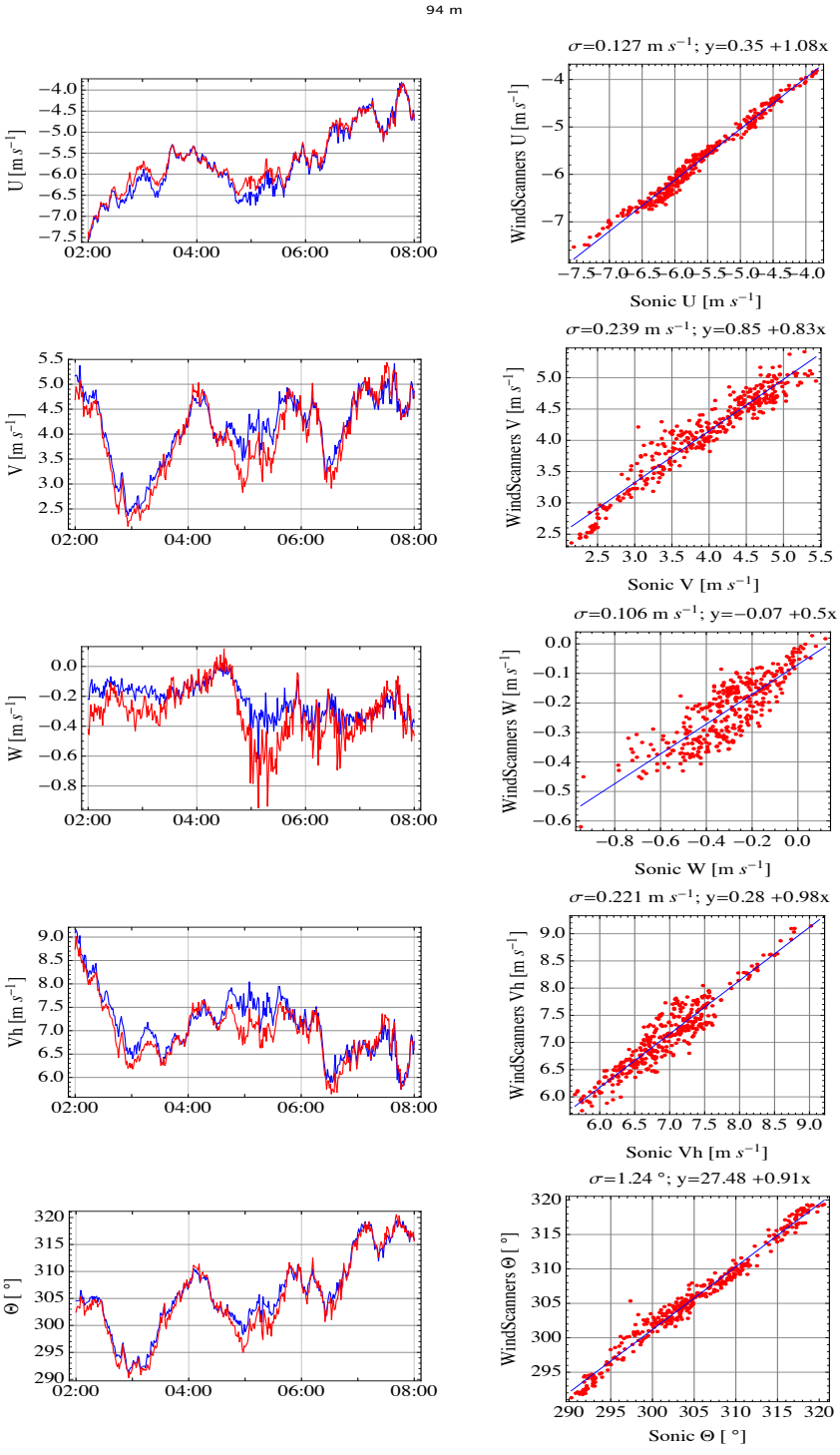

Figure 5.7: Measurements at 94 m. The blue curves are one-minute block averaged sonic anemometer measurements, while the red curves are one-minute block averaged measurements of the long-range WindScanner system.

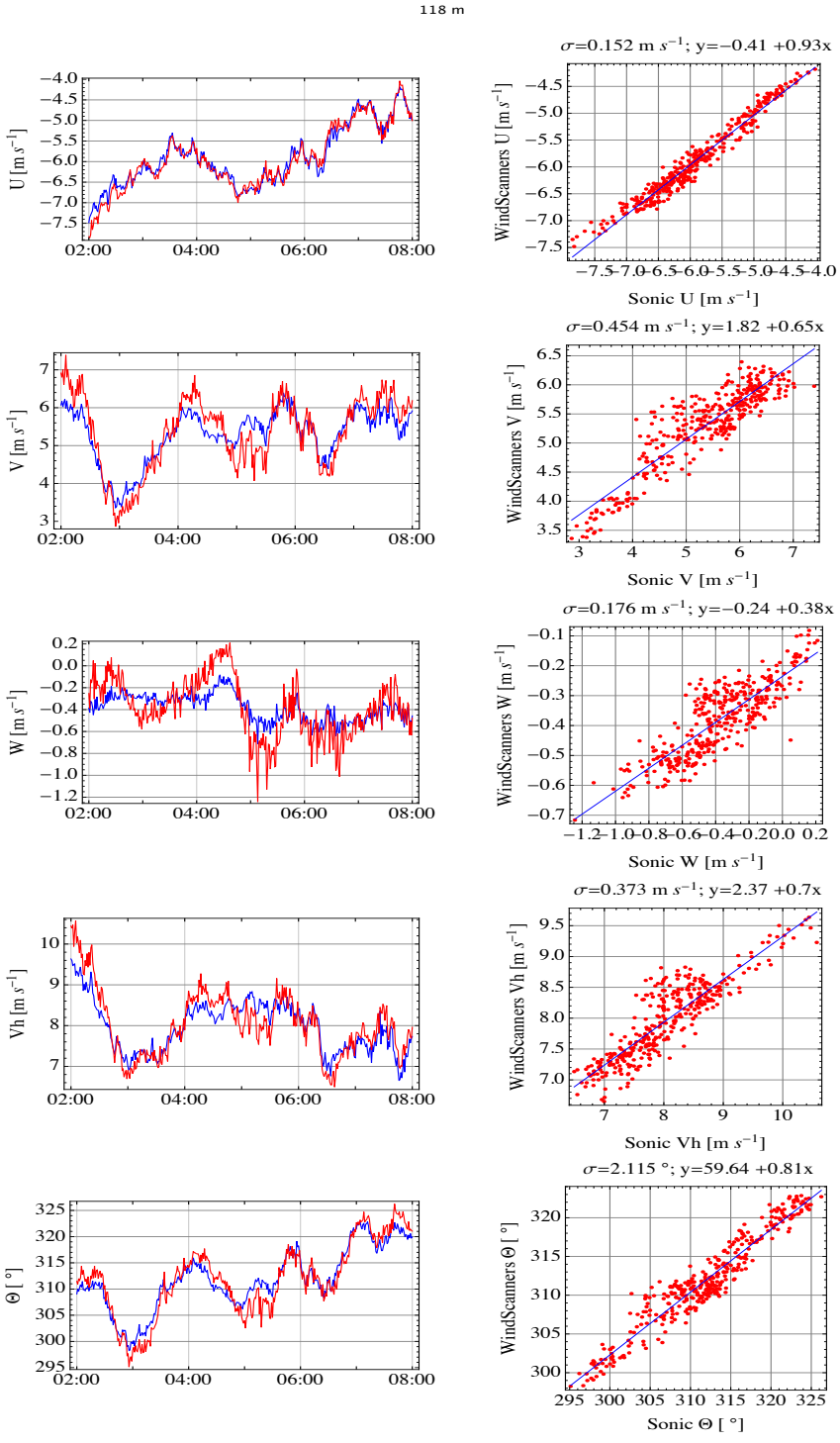

Figure 5.8: Measurements at 118 m. The blue curves are one-minute block averaged sonic anemometer measurements, while the red curves are one-minute block averaged measurements of the long-range WindScanner system.

5.5.4 Simulation results

In order to test if the grounds for the previous statement regarding the increase of the standard deviation and the scatter in the linear regression plots are correct, measurements of the WindScanners in the observed wind conditions have been simulated using a WindScanner simulator [84]. A time-varying 3D wind field has been generated using the block averaged one-minute time series of the horizontal wind velocity, wind direction and vertical component W from three sonic anemometers.

It has been assumed that the 3D wind field is horizontally homogeneous, and that the time-varying vertical profile of the horizontal wind velocity follows the wind profile power law:

$$\begin{aligned} V_h(z,t) &= V_{hs}(118,t)\left(\frac{z}{118}\right)^{\alpha(t)} \\ \alpha(t) &= \frac{\log\left(\frac{V_{hs}(118,t)}{V_{hs}(76,t)}\right)}{\log\left(\frac{118}{76}\right)} \end{aligned} \tag{5.10}$$

where, $V_h(z,t)$ is the horizontal wind velocity at the height z, $V_{hs}(118,t)$ is the horizontal wind velocity measured by the sonic anemometer at 118 m height, $\alpha(t)$ is the power law exponent calculated using the horizontal wind velocities measured by the sonic anemometers at 118 m height, $V_{hs}(118,t)$, and 76 m height, $V_{hs}(76,t)$.

The time-varying vertical profile of the vertical wind velocity was modeled by the linear fit of the sonic anemometers measurements of the vertical wind velocities at 76, 94 and 118 m:

$$W(z,t) = a_w(t) + b_w(t)z \tag{5.11}$$

where, a_w and b_w are the result of the linear fit.

Similarly, the time-varying vertical profile of the wind direction was modeled by the linear fit of the calculated wind directions at 76, 94 and 118 m using the sonic anemometers measurements of the horizontal wind velocity components:

$$\Theta(z,t) = a_\Theta(t) + b_\Theta(t)z \tag{5.12}$$

where, a_Θ and b_Θ are the result of the linear fit.

Using Equation 5.10 and 5.12, the horizontal wind velocity was decomposed into U and V components of the 3D wind field:

$$U(z,t) = V_h(z,t)\sin\Theta(z,t) \tag{5.13}$$

$$V(x,t) = V_h(z,t)\cos\Theta(z,t) \tag{5.14}$$

With Equation 5.11, 5.13 and 5.14 the time-varying 3D wind field has been described. On the other hand the WindScanners measurements process has been modeled using Equation5.3 and 5.5.

In the simulation, the half length l has been set to the value given in Equation 5.2, which is 60 m. The results of the simulation are shown in Figure 5.9, 5.10 and 5.11 and Table 5.4, 5.5 and 5.6. The increase in the standard deviation and the scatter in the linear regression plots can be observed from the figures and the tables, which is consistent with the results from the measurements . Therefore, the simulation results support the statement from the previous subsection.

	WindScanners simulated	Sonic anemometer	Mean difference	Standard deviation of the difference (σ)
U [m s^{-1}]	-5.53	-5.56	0.03	0.03
V [m s^{-1}]	2.97	3.11	-0.14	0.21
W [m s^{-1}]	-0.07	-0.16	0.09	0.02
Vh [m s^{-1}]	6.35	6.42	-0.07	0.09
Θ [$^\circ$]	298.38	299.39	-1.01	1.75

Table 5.4: Mean values for the U, V and W components of the wind velocity, horizontal wind velocity V_H and wind direction for the point of the laser beams intersection located 20 cm above the sonic anemometer at 76 m height.

	WindScanners simulated	Sonic anemometer	Mean difference	Standard deviation of the difference (σ)
U [m s^{-1}]	-5.81	-5.74	-0.07	0.05
V [m s^{-1}]	3.96	4.12	-0.16	0.21
W [m s^{-1}]	-0.13	-0.22	0.09	0.03
Vh [m s^{-1}]	7.1	7.11	-0.01	0.13
Θ [$^\circ$]	304.3	305.84	-1.54	1.32

Table 5.5: Mean values for the U, V and W components of the wind velocity, horizontal wind velocity V_H and wind direction for the point of the laser beams intersection located 20 cm above the sonic anemometer at 94 m height.

	WindScanners simulated	Sonic anemometer	Mean difference	Standard deviation of the difference (σ)
U [m s^{-1}]	-5.91	-5.9	-0.01	0.04
V [m s^{-1}]	5.44	5.29	0.15	0.29
W [m s^{-1}]	-0.21	-0.38	0.17	0.02
Vh [m s^{-1}]	8.1	7.96	0.14	0.19
Θ [$^\circ$]	312.43	311.9	0.53	1.66

Table 5.6: Mean values for the U, V and W components of the wind velocity, horizontal wind velocity V_H and wind direction for the point of the laser beams intersection located 20 cm above the sonic anemometer at 118 m height.

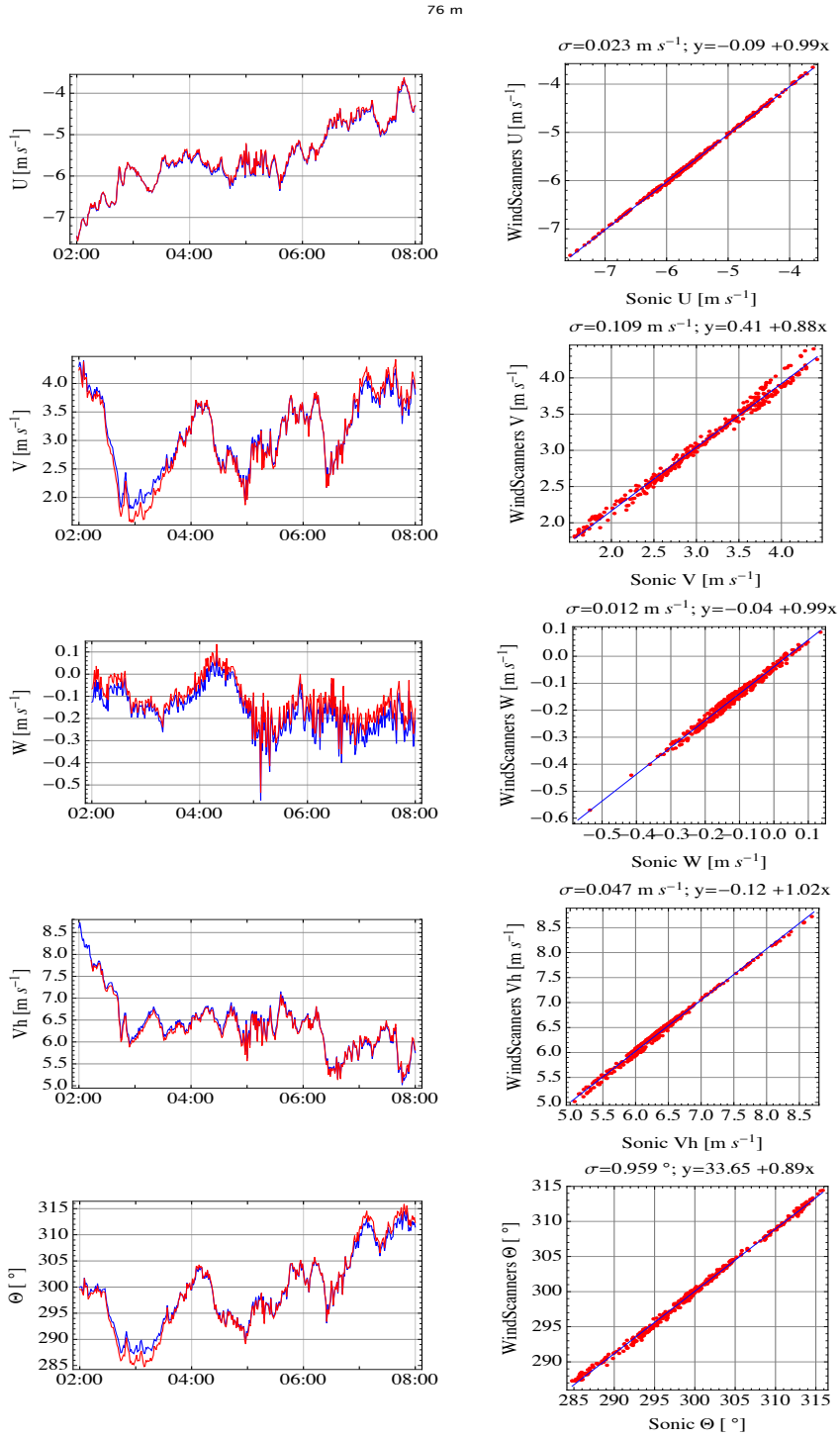

Figure 5.9: Measurements at 76 m. The blue curves are one-minute block averaged sonic anemometer measurements, while the red curves are simulated one-minute block averaged measurements of the long-range WindScanner system.

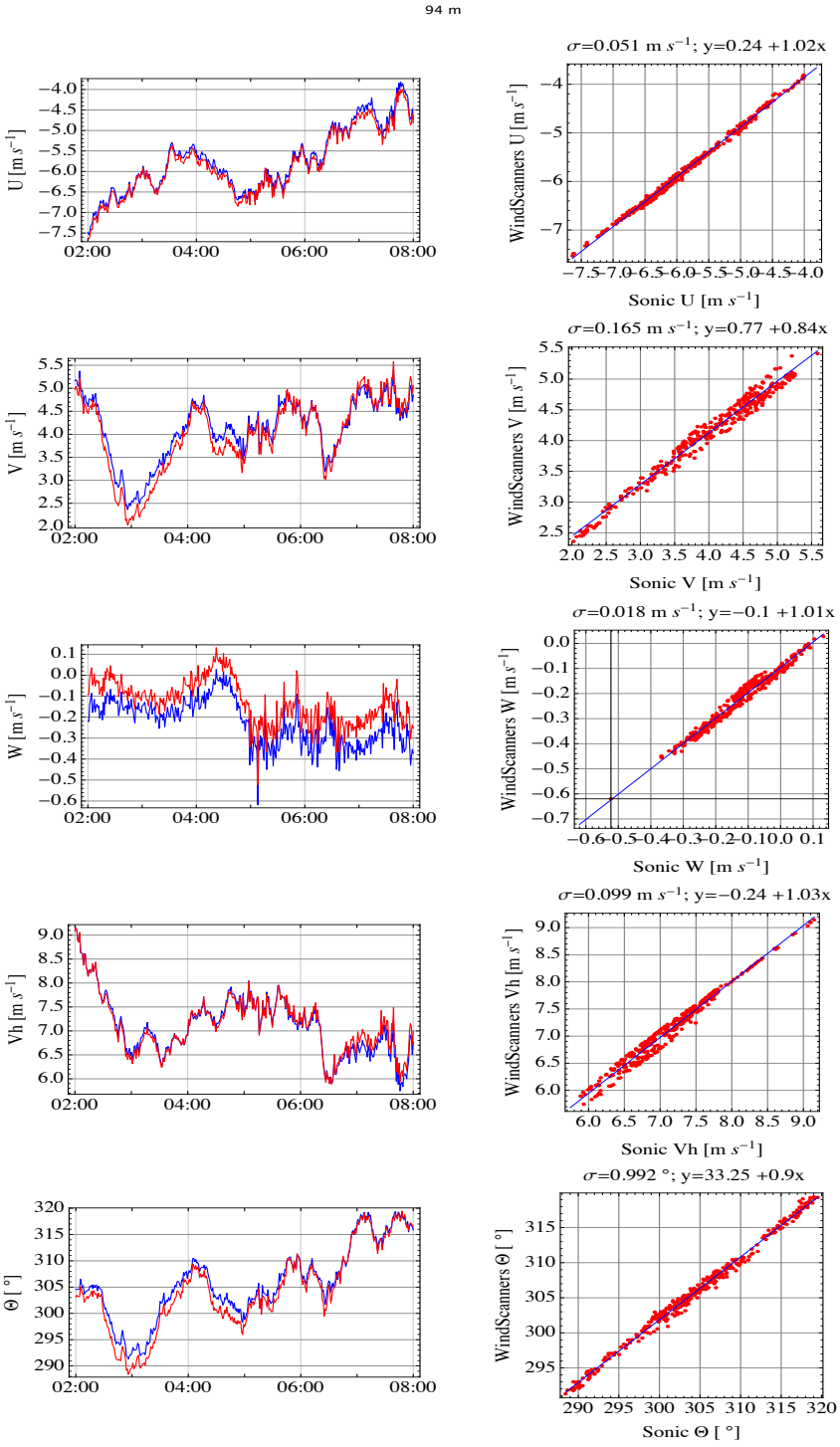

Figure 5.10: Measurements at 94 m. The blue curves are one-minute block averaged sonic anemometer measurements, while the red curves are simulated one-minute block averaged measurements of the long-range WindScanner system.

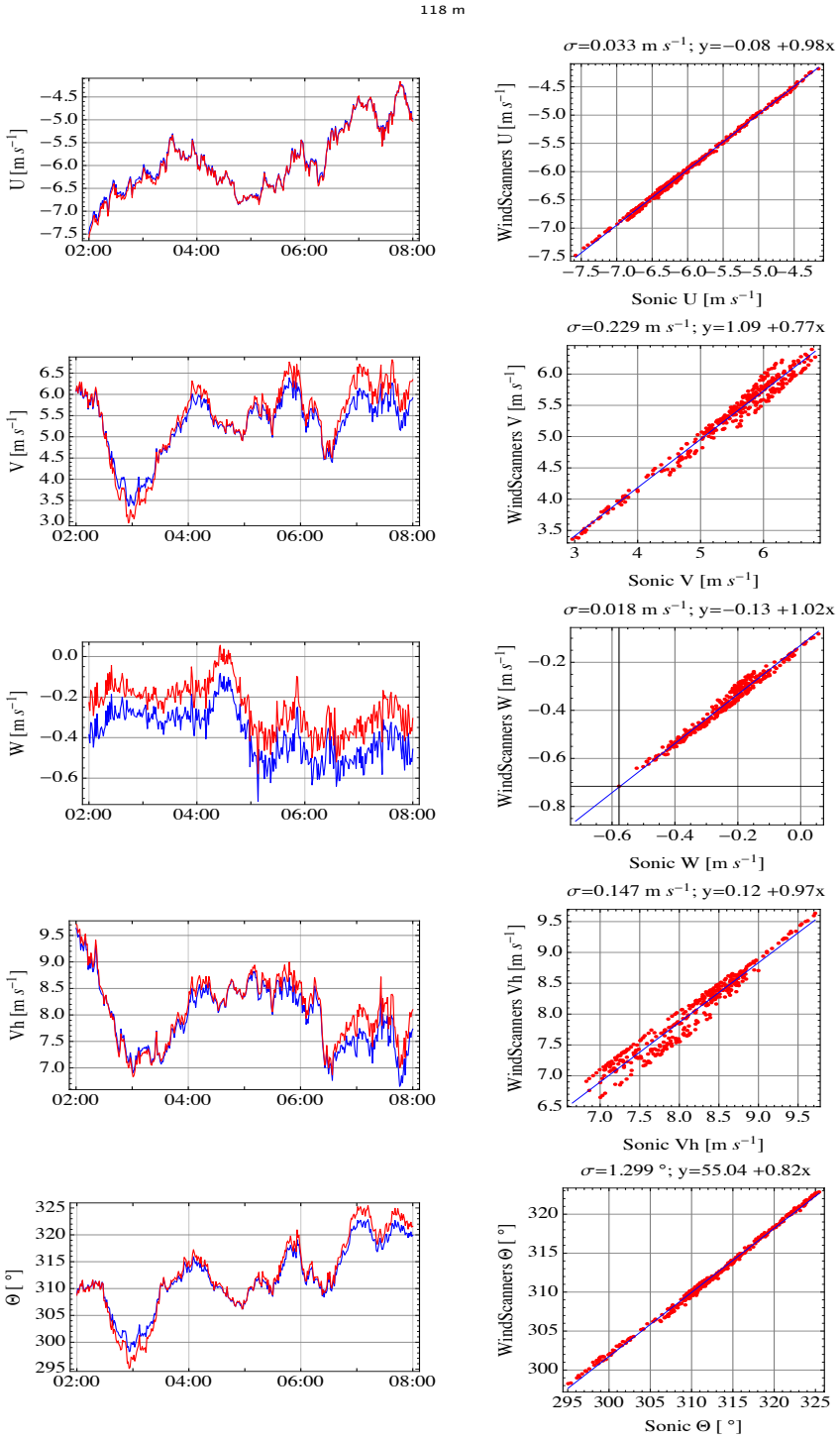

Figure 5.11: Measurements at 118 m. The blue curves are one-minute block averaged sonic anemometer measurements, while the red curves are simulated one-minute block averaged measurements of the long-range WindScanner system.

5.6 Discussion

The Swinging Musketeer Experiment was the first experiment with the long-range WindScanner system. For the first time the system of three scanning Doppler lidars has been demonstrated. It has also shown the system's capability to measure synchronously the three components of the wind velocity in multiple points in the atmosphere.

Time series of the WindScanners and the sonic anemometers measurements of the wind velocities have shown good correlation. It has been found that the standard deviation of the error and thus the scatter in the linear regression plots increase with height. The reason for this is the difference in the measurement principles of a sonic anemometer and Doppler lidar in relation to the encountered high complexity of the flow. To a certain extent this has been shown with the simulation of the WindScanners measurements in the observed wind conditions. It is anticipated that similar results would be achieved in complex terrain or in urban canopy with the long-range WindScanner system configured to emit long pulses.

Probably the results of the comparisons of the system with the sonic anemometers would be better if the WindScanners laser pulses and the radial velocity acquisition time were lower. By shortening the laser pulses it is expected that the standard deviation would be lower for all heights. A high measurement rate would allow more sampling points in the averaging periods and the comparison of the components of the wind velocity over shorter averaging periods. Since the shorter pulse length and the higher measurement rate were not possible in this experiment, it would be interesting to repeat the Swinging Musketeer Experiment. In the succeeding Swinging Musketeer experiments the WindScanners should be configured to emit 200 ns laser pulses, and to acquire radial velocity measurements with the rate of 10 Hz.

Even with the proposed improvements in the WindScanner configuration it is unreasonable to expect an absolute correlation between the long-range WindScanner system and the sonic anemometers measurements of the components of the wind velocities. The long-range WindScanner system measures wind velocities within a volume and not just at a point, like sonic anemometers. It is of great interest to identify and characterize all the central effects arising from the volumetric measurements of the long-range WindScanner system - ranging from the bias induced by the sheared flows to the filtering effects on the turbulence. Another important issue is to fully understand the implications of the intersecting beam volumes. These fundamental topics should be a part of the future work.

Another topic that should be addressed in the following Swinging Musketeer experiments is the laser beam positioning accuracy. Since the exact positions of the sonic anemometers in the Swinging Musketeer experiment were unknown, they were found using the WindScanners laser beams. In the forthcoming experiments with the WindScanners, it would be reasonable to expect that the intersection points in the atmosphere will not be close to hard targets, which could be used to accurately position the laser beams to intersect. Therefore, for

the following Swinging Musketeer experiments it would be interesting to acquire the exact positions of the sonic anemometers by geodetic survey and to compare those positions with the positions acquired by the WindScanners laser beams. This would allow the laser beam positioning accuracy testing.

However, even though the location of the Swinging Musketeer Experiment has its advantages, such as the proximity to the WindScanner lab and the existing infrastructure, the disadvantages limit the use of the location. The available space and the complexity of the flow do not allow the wind velocity calibration of Doppler lidars with long probe lengths. For this particular type of tests it is advisable to consider other locations in which the flow is not complex, such as the test station for large wind turbines Høvsøre [41].

Finally, it should be emphasized that the first experiment with the long-range WindScanner system was used to validate, in an outdoor environment, the concepts and software solutions of the long-range WindScanner system, which were described in the previous chapters. Over the course of the experiment the WindScanner client software and the master computer software were stable. During the initial steps, prior to measurements, CNR mapper proved to be a useful tool for the home position calibration and the calculation of the angles and the distances necessary for the setup of the measurement scenarios. The master computer did not lose the connection with the WindScanners, which allowed the maximum lag to be kept below 10 ms.

Chapter 6

IBL WiSH experiment

6.1 Introduction

The experiment "**I**nternal **B**oundary **L**ayer, **Wi**nd**S**canners at **H**øvsøre" (IBL WiSH) took place at the test station for large wind turbines Høvsøre, during the month of June 2013. The goal with this experiment was to create a unique wind velocity measurements dataset with the long-range WindScanner system and mast mounted sonic anemometers for the investigation of changes of sea-land IBL. This was the first experiment in which the long-range WindScanner system was used as an instrumentation for scientific studies.

6.2 Layout of the campaign

The test station is located in western Jutland, Denmark (Figure 6.1). Agricultural flat lands surrounds the test station, with a sea-coast transition from West. In general, terrain orography and roughness are far simpler than the orography and roughness of the site from the Swinging musketeer experiment. Apart from a 10-meter sand dune, which follows the costal line, there are no other objects that can disturb westerly winds. Therefore, away from the dune it is justified to consider the flow not complex over the scale of the WindScanner probe length, and in most cases horizontally homogeneous.

Apart from being used for the power performance tests of wind turbines, the test station has also been extensively used for the wind velocity calibration of commercially available lidars [41]. It is heavily instrumented with quite good power and network infrastructure. It consists of a line of five test stands for multi-megawatt wind turbines, which are oriented north-south parallel with the coast (Figure 6.1). Each stand has its dedicated meteorological mast for wind velocity measurements of westerly winds. Beside these five meteorological masts, there are additionally a 116-meter tall meteorological mast, south of the line of five test stands, and a 80-meter mast west from the test stand three (Figure 6.1).

In addition to the existing meteorological masts, for the IBL WiSH 2013 campaign masts BM1, BM2 and BM3 have been installed, along with three long-range WindScanners. The masts BM1 and BM2 are 15 meters tall, while the mast BM3 is 18 m tall. At each mast there are sonic anemometers at three heights, 2 and 5 m above the ground level and one on the top, and also temperature and pressure sensors.

The position of the additional instrumentation was primarily chosen to provide dense measurements of the westerly winds in multiple points at the area where the changes of the sea-coast IBL are expected to be found (area of interest at Figure 6.1).

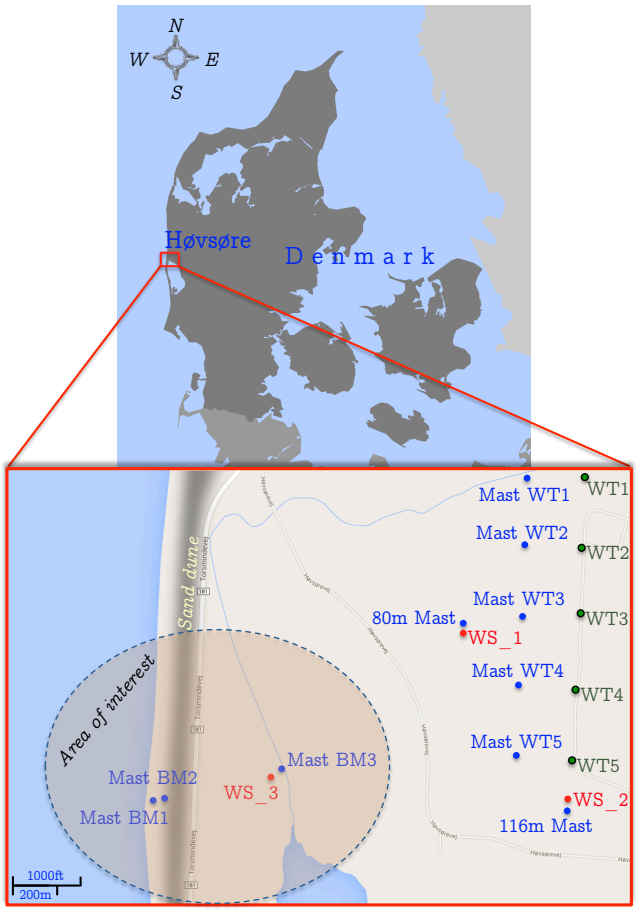

Figure 6.1: Instrumentation at Høvsøre. Abbreviations 'WT' and 'WS' represent 'Wind Turbine' and 'WindScanner' respectively.

6.3 Intial measurement scenarios

After the installation, leveling was performed using a handheld dual-axis inclinometer having an accuracy of 0.01°. Afterwards, the WindScanners home positions were calibrated using a sonic anemometer, attached at the top of the mast BM3, as a hard target. Also, this 'hard target' was used for the sensing distance calibration.

Afterwards, the WindScanners were configured to run PPI scenarios in a 'surveillance mode' (full 360°) at elevation angles around 4° with the azimuth speeds of $1°/s$. The pulse type used for the WindScanners measurements was 'Middle', with FFT size equal to 64, pulse repetition frequency of 20 kHz and the accumulation time of one second. The maximum range was set to 5 km, where the range gates were positioned every 50 m. The goal of these measurement scenarios was to check the stability of the WindScanners and availability of the measurements during a three-day period.

The WindScanners did not fail during this period, and data availability is 100%. Figure 6.2 shows one full PPI scan made with WindScanner_1, superimposed on the Google Earth image of the surroundings of the test station. Due to the low elevation angle used in the scenario, the wakes of four wind turbines, installed at the test stands, can be clearly seen.

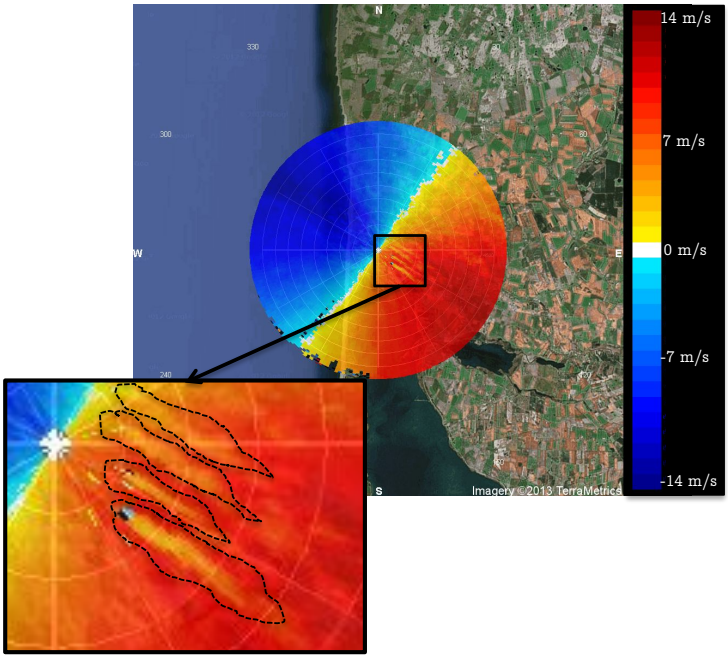

Figure 6.2: A snapshot of the flow around the test station taken on June 7^{th} with WindScanner_1. Wakes of four wind turbines can be well distinguished in the entire flow.

After the PPI scenarios, the RHI scenario was run on WindScanner_2,for a short period of time, at the azimuth angle of 30° for the range of the elevation angles from 0° to 180°, with the elevation speed of $1°/s$. The maximum range was set to 2.5 km, with range gates positioned every 25 m. The pulse settings and the accumulation time were identical to the previous measurement scenarios.

The aim with this scenario was to check if it is possible to deduce the depth of the ABL from the radial velocity data. From Figure 6.3 it is clear that the depth can be deduced, since above the top of ABL there are far less particles, and consequently a much lower CNR as indicated by many missing radial velocity estimates. An interesting flow phenomenon of a low-level jet, a bit below the top of ABL, was captured while performing this scenario.

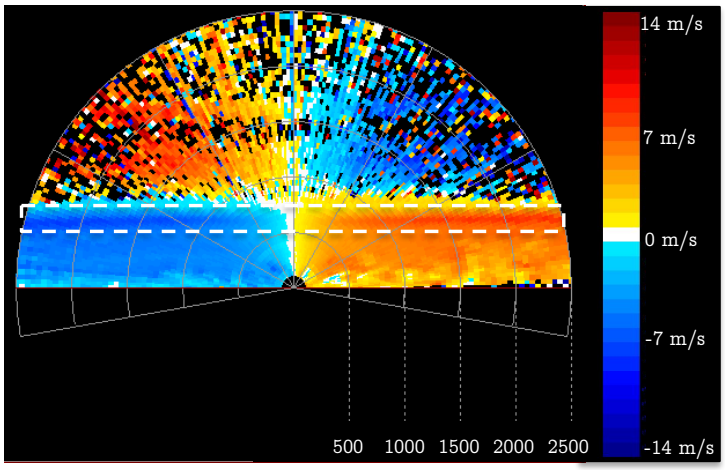

Figure 6.3: A low-level jet at 800 m above the ground level (marked with the dashed line).

The last step before starting the intended measurements for this campaign, was to check how well the WindScanners measure radial velocity. For this purpose, three laser beams from three WindScanners were intersected above the sonic anemometer at the top of the mast BM3 for a 9-hour period. The pulse type used for the WindScanners measurements was 'Middle', with the FFT size equal to 64, pulse repetition frequency of 20 kHz and the accumulation time of 500 ms (measurement rate of 2 Hz).

Radial velocities measured by the WindScanners were compared with the measured wind velocities from the anemometer projected to each laser beam direction. From the results in Figure 6.4, it can be seen that the radial velocity measurements are well correlated with the wind velocities measured with the sonic anemometer, projected to the laser beams directions for all three WindScanners.

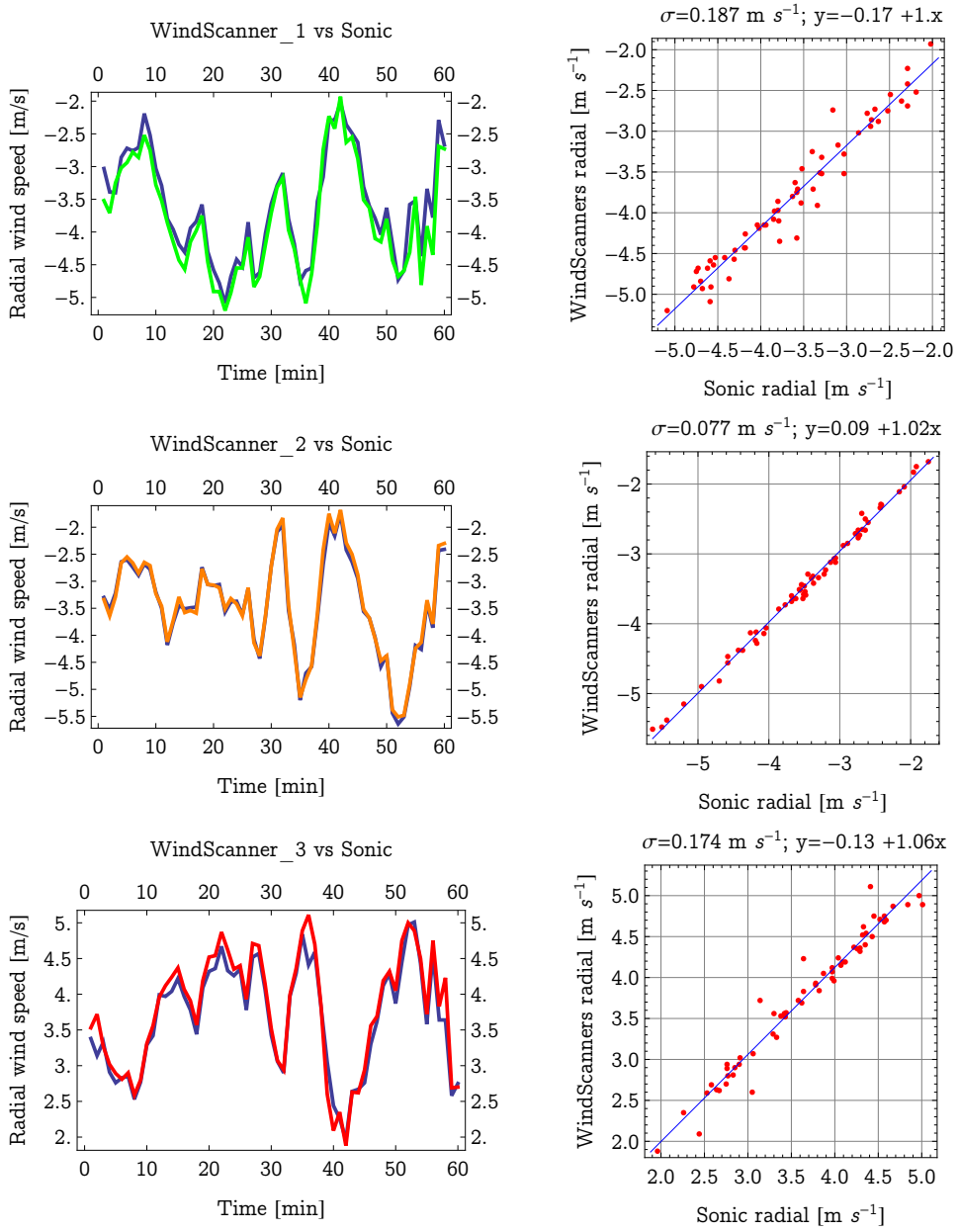

Figure 6.4: A one-hour period (June 11^{th}, 22:00 - 23:00) of one-minute averages of the radial velocities acquired with the WindScanners (green, orange and red curves) and the sonic anemometer wind velocities projected to the beam direction of each WindScanner (blue curves).

6.4 IBL WiSH measurement scenario

The main ambition with the three long-range WindScanners was to measure the wind field in a large number of measurement points in the volume of the atmosphere around the coast (Figure 6.1). The centre of attention was the vertical plane $ABCD$ parallel with the dune at 300 m distance from it, towards east (Figure 6.5). The dimensions of the plane are one kilometer in length and 160 meters in height. The mast BM3 is located in the centre of the side CD. At the plane, five traverses at 20, 40, 60, 116 and 160 m above the ground level were chosen as the position of points in the atmosphere at which the WindScanners measurements should be taken. It was anticipated that the traverses will 'slice' through the different fetch of the coastal IBL for a range of westerly winds, since the vertical plane is parallel with the coast.

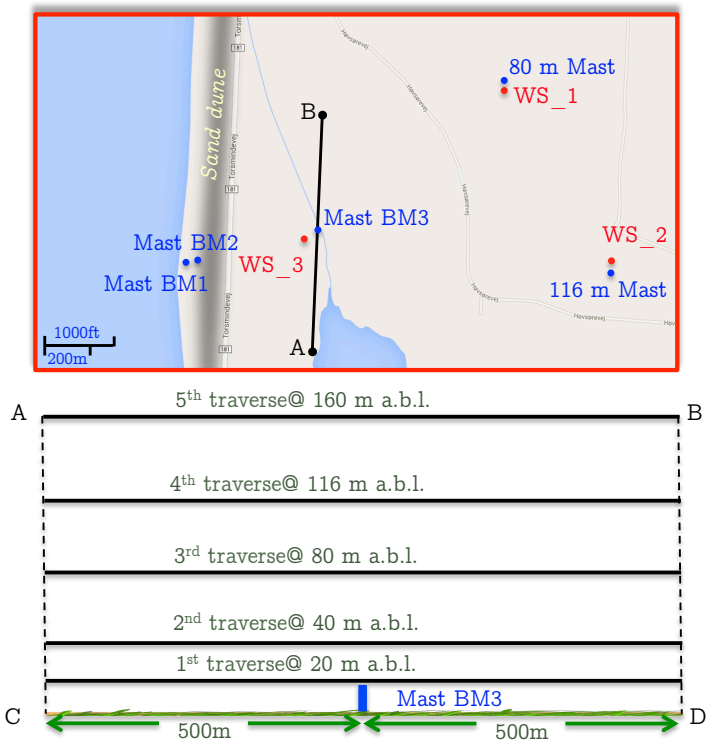

Figure 6.5: Five traverses along which the WindScanners measurements were taken.

The WindScanners were configured with three sets of measurement scenarios. In the first set of scenarios, all three WindScanners were optimized to synchronously move the point of intersection of the laser beams along the traverses. One iteration of the first scenarios set, and thereby one snapshot of the vertical plane of interest, took about two minutes. The motion programs of

these scenarios were coded manually. Under two minutes' time was not possible, since WindScanner_3 had already reached its kinematic limits. It was decided that the sampling time of two minutes will not provide the necessary amount of data for the analysis of the IBL, and the execution of the first set of measurement scenarios was stopped after a few hours.

In the second set of measurement scenarios the sampling time of the vertical plane was reduced to roughly one minute. However, in this scenario set only WindScanner_1 and WindScanner_2 were intersecting their beams along the traverses (Figure 6.6), where their measurement scenarios had the following features:

- Completion of a traverse at one height took 12 s
- The azimuth speed was kept constant along the traverse, and equal for each height
- The elevation speed was varying in order to keep the laser beam constantly at the same height along the traverse
- The laser pulse type was set to 'Middle' (i.e. 200 ns temporal pulse length), with the FFT size equal to 64 and a pulse repetition frequency of 20 kHz
- The laser pulses were constantly emitted along the traverse which, with the accumulation time of 200 milliseconds, resulted in the measurement rate of 5 Hz and thus 24 LOS measurements along each traverse
- Ranges at which the radial velocities were extracted along one LOS were changing from one LOS measurement to another, in order to provide measurements of the radial velocity in the points of the traverses, and also before and after
- The number of ranges was set to 25, with the maximum range of 2400 m.

With these parameters, WindScanner_1 and WindScanner_2 each acquired 3000 radial velocities measurements during one iteration of the measurement scenarios. Once again the motion programs for these scenarios were coded manually.

While WindScanner_1 and WindScanner_2 performed the synchronous radial velocity measurements on the vertical plane, WindScanner_3 performed five RHI scans at azimuth angles of 54°, 63°, 95°, 127° and 136°. The elevation speed was set to 1°, the maximum range to 1430 m, and number of ranges, which were more densely packed close to WindScanner_3, to 30 (Figure 6.7, b). The motion program for this measurement scenario was generated automatically using the TeslaBlackBox subprogram. This scenarios' set was executed for two days.

In the third set of measurement scenarios WindScanner_1 and WindScanner_2 performed the synchronous radial velocity measurements on the vertical plane, while WindScanner_3 crossed the same points on the vertical plane, however in different time frames (Figure 6.7, c). The third set of the scenarios was executed during the last two weeks of June 2013.

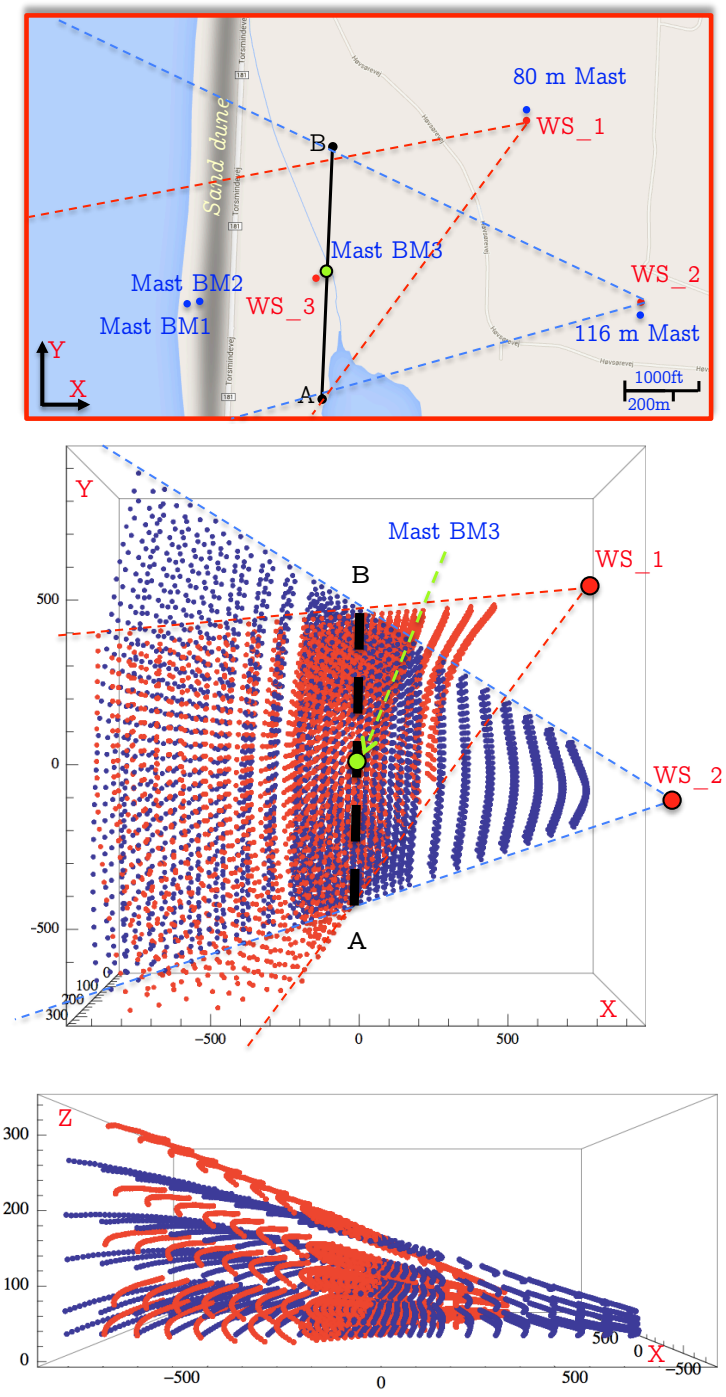

Figure 6.6: Position of the measurement points of WindScanner_1 and WindScanner_2 in relation to the vertical plane and the sand dune.

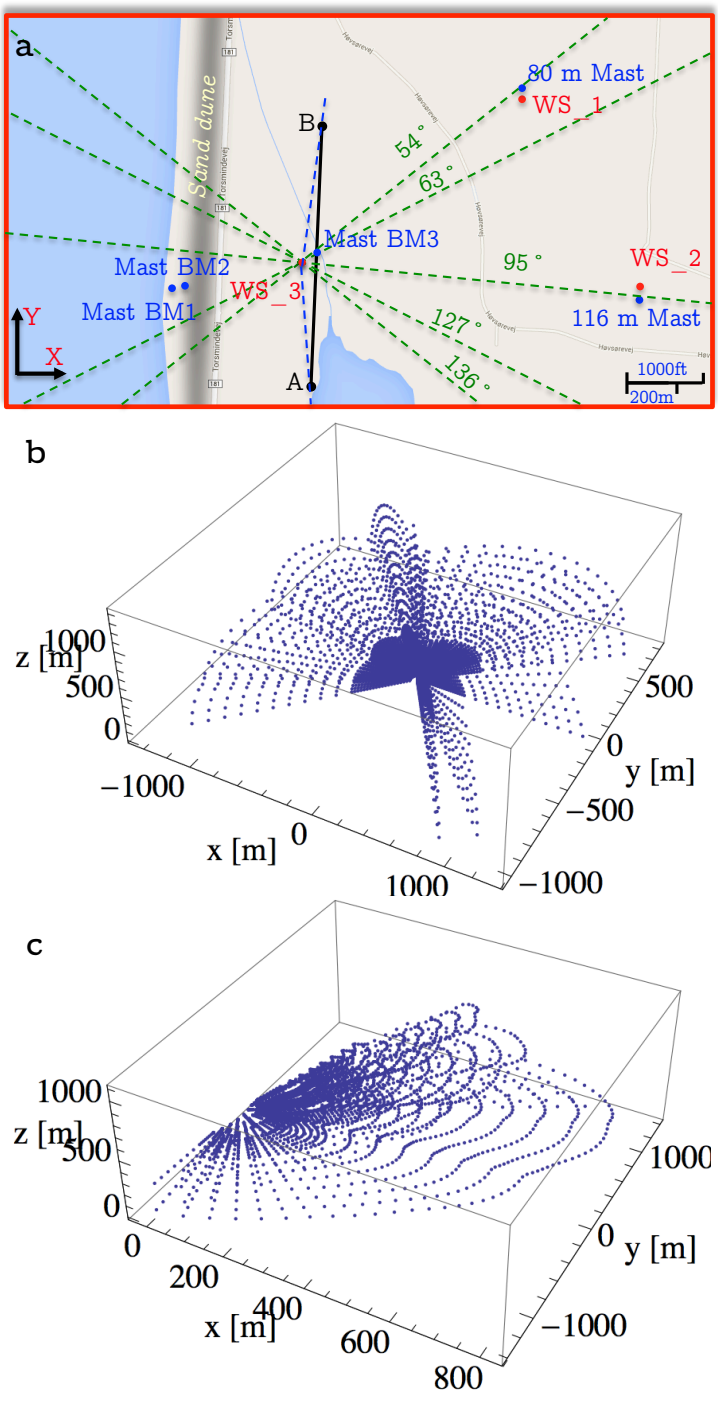

Figure 6.7: Different measurements scenarios performed by WindScanner_3.

With the second set of measurement scenarios it was anticipated that WindScanner_1 and WindScanner_2 will provide dataset of radial velocities, which would allow good reconstruction of 2D (horizontal) wind field at the vertical plane. On the other hand WindScanner_3 was configured to provide information about the vertical component of the wind field around the centre of the vertical plane together with the information of the ABL depth over the large volume of the atmosphere. Also, by combining the information of the wind direction from the masts and two other WindScanners, the radial velocities acquired with WindScanner_3 could be used to calculate the horizontal wind velocity. With the third set of measurement scenarios it was anticipated that all three WindScanners will provide dataset of radial velocities, which would allow good reconstruction of the mean 2D (horizontal) wind field at the vertical plane.

Common to all three scenarios sets is that they were configured to provide at least one measurement point of the radial velocity close to one of the masts during each iteration of the measurement scenarios. In this way, the quality of datasets of the radial velocities could be validated by the comparison with the wind velocity measurements from the masts.

6.5 Results

The analysis of the acquired dataset is ongoing, and in this thesis the preliminary snapshots of a 10-minute mean distribution of the horizontal velocity on the vertical plane of interest (Figure 6.5) made during the execution of the third scenarios' set are shown in Figure 6.8.

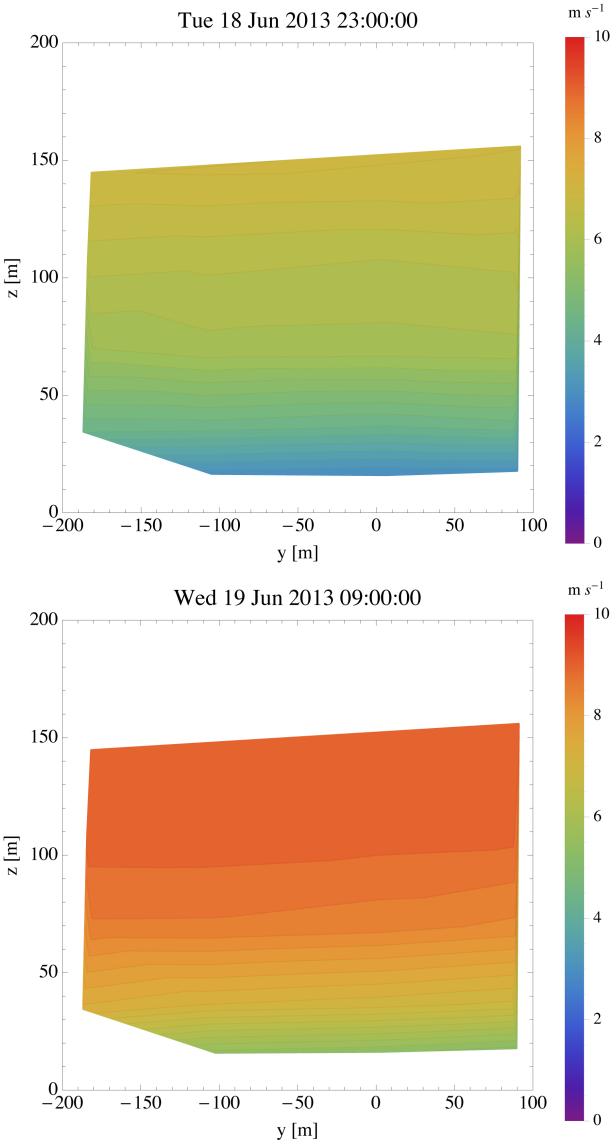

Figure 6.8: Distribution of the horizontal velocity on the vertical plane from Figure 6.5 for different hours during June 18^{th} and 19^{th}

6.6 Discussion

The IBL WiSH experiment was the first experiment in which the long-range WindScanner system has been used as a tool for scientific research. This experiment created a unique wind velocity measurements dataset with the long-range WindScanner system and the mast mounted sonic anemometers. The amount of data is large, and is still being analyzed. It is expected that this data will provide a detailed investigation of changes of the sea-land IBL. Moreover, since the large number of measurement points were acquired close to the mast BM3 it is anticipated that this dataset will provide good insights in to the investigation of the volumetric averaging of the WindScanners. However, recent experience has shown that analysis of a large amount of data is difficult, and that for future experiments it needs to be planned thoroughly.

The IBL WiSH experiment showed that the long-range WindScanner system is able to measure wind velocity in a large volume of the atmosphere. This was the first time that multiple scanning lidars performed synchronous complex measurements scenarios, in which they moved the laser beams intersection over a large area of interest. In the first measurement scenarios a complete 3D flow was measured with the three synchronized WindScanners. In the second measurements scenarios the horizontal components of the 3D wind flow were measured with two synchronized WindScanners, while the information about the vertical component was provided by the third WindScanner that performed multiple RHI scans.

As in the case of the data analysis, planning of measurement scenarios needs lots of thought. Without any doubts, planning but particularly coding of the complex and synchronized measurement scenarios needs to be done in advance since it is laborious. In order to decrease the work load it is advisable to extend the capabilities of the TeslaBlackBox and automate the generation of the complex and synchronized trajectories such as those used in this experiment. This calls for coding and integration of the second order kinematic model of the scanner head in the TeslaBlackBox, which should be part of the future work.

In the IBL WiSH experiment, due to technical reasons, only the procedures for the homing and the sensing distance calibration were followed from the whole set of procedures regarding the mitigation of the impacts of different contributions of the laser beam pointing uncertainty explained in Chapter 4. For future experiments, it is advisable to follow all procedures, and it would be necessary to install and use multiple hard targets. Also, one or more hard targets should be incorporated in measurement scenarios in such a way that in each iteration of the scenarios, WindScanners 'hit' the hard targets with the laser beams at specific scanner head positions. By doing this it would be possible to perform analysis of the repeatability of the scanning trajectory, and to monitor how accurately WindScanners steer the laser beams over the course of the experiment.

It is advisable to deploy a small meteorological mast as one of the targets. In this way one of the hard targets can also be used for a continual comparison of the wind velocity measurements made with the WindScanners with those

acquired by a mast-mounted sonic or cup anemometer. This comparison can be an indicator of the WindScanners wind velocity data quality.

Chapter 7

Conclusion

The possibility of 3D wind velocity measurements in a great many points of interest in the atmosphere, by the time-space synchronization of coherent Doppler scanning lidars, has been investigated. These measurements have particular significance in solving the lack of wind velocity fields measurements at full scale, thus providing the basis for the advancement of our understanding of the flows in the ABL, relating to wind energy in particular.

A new three coherent Doppler scanning lidars (long-range WindScanners) have been developed using the original operational principles, which provide strict synchronization of laser pulses emission, laser pulses steering, and acquisition of the backscattered light and the accurate time control over these processes.

The devised lidar software architecture, based on these principles, provides great flexibility in terms of the motion of the scanner head and configurability of the wind velocity measurements.

It has been shown that with the novel approach in the formation of a unified measurement system of multiple lidars, in which the master computer simultaneously coordinates the distant lidars through a UDP/IP and TCP/IP network, time synchronization of the lidars has been achieved. Also, this novel approach allows the flexibility of the lidars deployment, since the master computer and lidars can be connected using a wireless, 3G or satellite network connection. For the purpose of the lidars coordination, a new application layer communication protocol for remote sensing instruments (RSComPro) has been developed.

The laser beam pointing uncertainty has been studied, uncertainty sources identified, tests for each studied uncertainty study have been proposed, together with the procedures to reduce the uncertainty contribution of each uncertainty source, and the total laser beam pointing uncertainty has been estimated. The software tool, CNR mapper, has been developed to support many of the tests. With this software 3D imaging of objects can be achieved using a pulsed coherent Doppler scanning lidar.

The Swinging Musketeer Experiment was the first outdoor experiment with the long-range WindScanner system that has been performed to validate the

application of concepts and software solutions for wind measurements. For the first time the system of three coherent Doppler scanning lidars has been demonstrated. It has also shown the system's capability to measure synchronously the three components of the wind velocity in multiple points in the atmosphere. The comparison between the measurements, made with the long-range WindScanner system and those acquired by the sonic anemometers from the co-located mast, have shown good correlation.

During the second experiment with the long-range WindScanner system a unique wind velocity measurements dataset with synchronous data from the long-range WindScanner system and mast mounted sonic anemometers was created. In this experiment for the first time multiple scanning lidars have been used to perform synchronous complex measurements scenarios, in which they moved the laser beams intersection over a large area of interest. It has been shown that the long-range WindScanner system is able to measure the wind velocity in a large volume of the atmosphere and that the system potentially represents a new tool for wind energy research.

Bibliography

[1] IEC. Wind turbines, Part 12-1: Power performance measurements of electricity producing wind turbines. Technical report, nternational Standard 61400-12-1, International Electrotechnical Commission, 2005.

[2] Rozenn Wagner, Ioannis Antoniou, Søren M. Pedersen, Michael S. Courtney, and Hans E. Jørgensen. The influence of the wind speed profile on wind turbine performance measurements. *Wind Energy*, 12(4):348–362, May 2009.

[3] Rozenn Wagner, Michael Courtney, Julie Gottschall, and Per Jonas Petter Lindelöw. Accounting for the speed shear in wind turbine power performance measurement. *Wind Energy*, 14(8):993–1004, November 2011.

[4] European Wind Energy Association. *Wind Energy - The Facts: a guide to the technology, economics and future of wind power*. Earthscan, London; Sterling, VA, July 2009.

[5] Yelena L. Pichugina, Robert M. Banta, W. Alan Brewer, Scott P. Sandberg, and R. Michael Hardesty. Doppler Lidar–Based Wind-Profile Measurement System for Offshore Wind-Energy and Other Marine Boundary Layer Applications. *Journal of Applied Meteorology and Climatology*, 51(2):327–349, February 2012.

[6] Niels G. Mortensen, Duncan N. Heathfield, Lisbeth Myllerup, Lars Landberg, and Ole Rathmann. Getting Started with WAsP 9. Technical Report June, RisøNational Laboratory Technical University of Denmark, Roskilde, Denmark, 2007.

[7] P. A. Taylor and H. W. Teunissen. The Askervein Hill project: overview and background data. *Boundary-Layer Meteorology*, 39(1-2):15–39, 1987.

[8] F. A. Castro, J. M. L. M Palma, and A. S. Lopes. Simulation of the Askervein Flow. Part 1: Reynolds Averaged Navier–Stokes Equations (k Turbulence Model). *Boundary-Layer Meteorology*, 107(1996):501–530, 2003.

[9] A. Silva Lopes, J. M. L. M. Palma, and F. a. Castro. Simulation of the Askervein flow. Part 2: Large-eddy simulations. *Boundary-Layer Meteorology*, 125(1):85–108, 2007.

[10] Jean-Christophe Golaz, James D. Doyle, and Shouping Wang. One-way nested large-eddy simulation over the Askervein Hill. *Journal of Advances in Modeling Earth Systems*, 2(6):6, July 2009.

[11] M. F. Gobbi and R. P. Dorweiler. Simulation of Wind Over a Relatively Complex Topography: Application to the Askervein Hill. *JOURNAL OF THE BRAZILIAN SOCIETY OF MECHANICAL SCIENCES AND ENGINEERING*, 34(4):492–500, 2012.

[12] Andreas Bechmann et all. The Bolund Experiment: Overview and Background. Technical Report Risø-R-1658(EN), RisøDTU, Roskilde, Denmark, July 2007.

[13] J. Berg, J. Mann, a. Bechmann, M. S. Courtney, and H. E. Jørgensen. The Bolund Experiment, Part I: Flow Over a Steep, Three-Dimensional Hill. *Boundary-Layer Meteorology*, 141(2):219–243, July 2011.

[14] A. Bechmann, N. N. Sørensen, J. Berg, J. Mann, and P.-E. Réthoré. The Bolund Experiment, Part II: Blind Comparison of Microscale Flow Models. *Boundary-Layer Meteorology*, 141(2):245–271, August 2011.

[15] Marc Diebold, Chad Higgins, Jiannong Fang, Andreas Bechmann, and Marc B. Parlange. Flow over Hills: A Large-Eddy Simulation of the Bolund Case. *Boundary-Layer Meteorology*, 148(1):177–194, February 2013.

[16] S. Emeis, M. Harris, and R. M. Banta. Boundary-layer anemometry by optical remote sensing for Wind energy applications. *Meteorologische Zeitschrift*, 16(4):337–347, 2007.

[17] K. A. Browning and R Wexler. The Determination of Kinematic Properties of a Wind Field Using Doppler Radar. *Journal of Applied Meteorology*, 7(1):105–113, February 1968.

[18] R. G. Strauch, B. L. Weber, A. S. Frisch, C. G. Little, D. A. Merritt, K. P. Moran, and D. C. Welsh. The Precision and Relative Accuracy of Profiler Wind Measurements. *Journal of Atmospheric and Oceanic Technology*, 4(4):563–571, December 1987.

[19] Xudong Liang. An Integrating Velocity–Azimuth Process Single-Doppler Radar Wind Retrieval Method. *Journal of Atmospheric and Oceanic Technology*, 24(4):658–665, April 2007.

[20] Rogier Floors, Claire Louise Vincent, Sven-Erik Gryning, Alfredo Peña Diaz, and Ekaterina Batchvarova. The wind profile in the coastal boundary layer: Wind lidar measurements and numerical modelling. *Boundary-Layer Meteorology*, 147:469–491, 2013.

[21] R. Krishnamurthy, A. Choukulkar, R. Calhoun, J. Fine, A. Oliver, and K.S. Barr. Coherent Doppler lidar for wind farm characterization. *Wind Energy*, 16(2):189–206, March 2013.

[22] J.C. Owens. OPTICAL DOPPLER MEASUREMENT OF MICROSCALE WIND VELOCITY. *PROCEEDINGS OF THE IEEE*, 57(4):530–536, 1969.

[23] A. J. Hughes, J. O'Shaughnessy, E. R. Pike, A. McPherson, C. Spavins, and T. H. Clifton. Long range anemometry using a co2 laser. *Opto-electronics*, 4(4):379–384, 1972.

[24] R. M. Hardesty, T. R. Lawrence, R. A. Richter, M. J. Post, F. F. Jr. Hall, and R. M. Huffaker. GROUND-BASED COHERENT LIDAR MEASUREMENT OF TROPOSPHERIC AND STRATOSPHERIC PARAMETERS. *Proceedings of SPIE - the International Society for Optical Engineering*, 415:85–91, 1983.

[25] G D Emmitt. *NASA/MSFC GROUND-BASED DOPPLER LIDAR NOCTURNAL BOUNDARY LAYER EXPERIMENT (NOBLEX)*. NASA Contractor Reports. National Aeronautics and Space Administration, Scientific and Technical Information Office, 1984.

[26] L. Danielsson and E. R. Pike. LONG-RANGE LASER ANEMOMETRY - A COMPARATIVE REVIEW. *JOURNAL OF PHYSICS AND SCIENTIFIC INSTRUMENTS*, 16(2):107–118, 1983.

[27] Sammy W. Henderson and Stephen M. Hannon. Advanced coherent lidar system for wind measurements. In *Lidar Remote Sensing for Environmental Monitoring VI*, volume 5887, pages 58870I–58870I–10, San Diego, California, USA, September 2005.

[28] Michael Courtney and Rozenn Wagner. Standardised and diversified lidars. *International Sustainable Energy Review Digital*, 6(3: Lidars supplement):2–6, 2012.

[29] Per Jonas Petter Lindelöw, Niels Mortensen, and Michael Courtney. Are Lidars Good Enough for Resource Assessments? – Accuracy of AEP predictions in flat terrain generated from measurements by conically scanning lidars. In *EWEC 2009*, page 9, Marseilles, France, March 2009.

[30] M Wächter, J Gottschall, A Rettenmeier, and J Peinke. Power curve estimation using LIDAR measurements. In *EWEC 2009*, page 5, Marseilles, France, March 2009.

[31] A. Rettenmeier, D. Schlipf, I. Würth, P.W. Cheng, A. Wright, P. Fleming, A. Scholbrock, and P. Veers. Power Performance Measurements of the NREL CART-2-Wind Turbine Using a nacelle-based Lidar scanner. In *ISARS 2012*, page 4, Boulder/Colorado, USA, June 2012.

[32] R. Wagner, T.F. Pedersen, M. Courtney, I. Antoniou, S. Davoust, and R.L. Rivera. Power curve measurement with a nacelle mounted lidar. *Wind Energy*, pages n/a–n/a, June 2013.

[33] B. Canadillas and T. Neumann. First test of a nacelle-based "2-beam" wind lidar system under offshore conditions. In *DEWI Magazin no. 39*, pages 26–33, August 2011.

[34] M Harris, M Hand, and A Wright. Lidar for Turbine Control Lidar for Turbine Control. Technical report, NREL National Renewable Energy Laboratory, January 2005.

[35] Michael Harris, David J. Bryce, Adrian S. Coffey, David A. Smith, Jochen Birkemeyer, and Ullrich Knopf. Advance measurement of gusts by laser anemometry. *JOURNAL OF WIND ENGINEERING AND INDUSTRIAL AERODYNAMICS*, 95(12):1637–1647, 2007.

[36] David Schlipf and Paul Fleming. Field testing of feedforward collective pitch control on the CART2 using a nacelle-based lidar scanner. In *The Science of Making Torque from Wind*, volume 2, Oldenburg, Germnay, 2012. IOP Conference Series.

[37] Ferhat Bingol, Jakob Mann, and Gunner C. Larsen. Light detection and ranging measurements of wake dynamics part i: one-dimensional scanning. *Wind Energy*, 13(1):51–61, 2010.

[38] Juan-José Trujillo, Ferhat Bingöl, Gunner C. Larsen, Jakob Mann, and Martin Kühn. Light detection and ranging measurements of wake dynamics. part ii: two-dimensional scanning. *Wind Energy*, 14(1):61–75, 2011.

[39] Yvonne Kasler, Stephan Rahm, Rudolf Simmet, and Martin K˘hn. Wake Measurements of a Multi-MW Wind Turbine with Coherent Long-Range Pulsed Doppler Wind Lidar. *Journal of Atmospheric and Oceanic Technology*, 27(9):1529–1532, September 2010.

[40] Stephen Hannon, Keith Barr, John Novotny, Andrew Oliver, Jeremy Bass, and Mike Anderson. Large Scale Wind Resource Mapping Using a State-of-the-Art 3D Scanning Lidar. In *WINDPOWER -PROCEEDINGS-; 1; 284-290 American Wind Energy Association Annual conference and exhibition, American Wind Energy Association*, pages 1–7, Huston, USA, June 2008. American Wind Energy Association , Washington.

[41] Michael Courtney, Rozenn Wagner, and Per Jonas Petter Lindelöw. Testing and comparison of lidars for profile and turbulence measurements in wind energy. *IOP Conference Series: Earth and Environmental Science*, 1:U172–U185, 2008.

[42] Alfredo Peña Diaz, Charlotte Bay Hasager, Sven-Erik Gryning, Michael Courtney, Ioannis Antoniou, and Torben Mikkelsen. Offshore wind profiling

using light detection and ranging measurements. *Wind Energy*, 12(2):105–124, 2009.

[43] Ferhat Bingol, Jakob Mann, and Dimitri Foussekis. Conically scanning lidar error in complex terrain. *Meteorologische Zeitschrift*, 18(2):189–195, April 2009.

[44] Stuart Bradley, Yvette Perrott, Paul Behrens, and Andy Oldroyd. Corrections for Wind-Speed Errors from Sodar and Lidar in Complex Terrain. *Boundary-Layer Meteorology*, 143(1):37–48, February 2012.

[45] Matthieu Boquet, A Albergel, Rémy Parmentier, Laurent Sauvage, and Jean-Pierre Cariou. Combination of Wind Lidar with CFD tools for improving measurements in complex terrain Lidar wind vector retrieval principle. In *25th International Laser Radar Conference - ILRC 25*, page 4, St. Petersburg, Russia, 2010.

[46] John McCarthy, James W. Wilson, and T. Theodore Fujita. The Joint Airport Weather Studies Project. *Bulletin of the American Meteorological Society*, 63(1):15–15, January 1982.

[47] Jeffry Rothermel, Cathy Kessinger, and Darien L. Davis. Dual-Doppler Lidar Measurement of Winds in the JAWS Experiment. *Journal of Atmospheric and Oceanic Technology*, 2(2):138–147, June 1985.

[48] KJ Allwine and JE Flaherty. *Joint Urban 2003: Study overview and instrument locations*. Number August. 2006.

[49] Rob Newsom, Ron Calhoun, David Ligon, and Jerry Allwine. Linearly organized turbulence structures observed over a suburban area by dual-doppler lidar. *BOUNDARY-LAYER METEOROLOGY*, 127(1):111–130, 2008.

[50] Rob K. Newsom, David Ligon, Ron Calhoun, Rob Heap, Edward Cregan, and Marko Princevac. Retrieval of Microscale Wind and Temperature Fields from Single- and Dual-Doppler Lidar Data. *Journal of Applied Meteorology*, 44(9):1324–1345, September 2005.

[51] R Calhoun, R Heap, M. Princevac, R. Newsom, H. Fernando, and D. Ligon. Virtual Towers Using Coherent Doppler Lidar during the Joint Urban 2003 Dispersion Experiment. *Journal of Applied Meteorology and Climatology*, 45(8):1116–1126, August 2006.

[52] Chris G. Collier, Fay Davies, Karen E. Bozier, Anthony R. Holt, Doug R. Middleton, Guy N. Pearson, Stephan Siemen, Dave V. Willetts, Graham J. G. Upton, and Rob I. Young. Dual-Doppler Lidar Measurements for Improving Dispersion Models. *Bulletin of the American Meteorological Society*, 86(6):825–838, June 2005.

[53] Vanda Grubisic, James D. Doyle, Joachim Kuettner, Stephen Mobbs, Ronald B. Smith, C. David Whiteman, Richard Dirks, Stanley Czyzyk, Stephen A. Cohn, Simon Vosper, Martin Weissmann, Samuel Haimov, Stephan F. J. De Wekker, Laura L. Pan, and Fotni Katopodes Chow. The terrain-induced rotor experiment a field campaign overview including observational highlights. *BULLETIN OF THE AMERICAN METEOROLOGICAL SOCIETY*, 89(10):1513–+, 2008.

[54] Michael Hill, Ron Calhoun, H. J. S. Fernando, Andreas Wieser, Andreas Dörnbrack, Martin Weissmann, Georg Mayr, and Robert Newsom. Coplanar Doppler Lidar Retrieval of Rotors from T-REX. *Journal of the Atmospheric Sciences*, 67(3):713–729, March 2010.

[55] Susanne Drechsel, Michel Chong, Georg J. Mayr, Martin Weissmann, Ronald Calhoun, and Andreas Doernbrack. Three-dimensional wind retrieval: Application of muscat to dual-doppler lidar. *JOURNAL OF ATMOSPHERIC AND OCEANIC TECHNOLOGY*, 26(3):635–646, 2009.

[56] Susanne Drechsel, Georg J. Mayr, Michel Chong, and Fotini K. Chow. Volume Scanning Strategies for 3D Wind Retrieval from Dual-Doppler Lidar Measurements. *Journal of Atmospheric and Oceanic Technology*, 27(11):1881–1892, November 2010.

[57] Giacomo Valerio Iungo, Yu Ting Wu, and Fernando Porté-Agel. Field measurements of wind turbine wakes with lidars. *Journal of Atmospheric and Oceanic Technology*, 30(2):274–287, 2013.

[58] Torben Mikkelsen, Jakob Mann, and Michael Courtney. Wind Scanner: A full-scale Laser Facility for Wind and Turbulence Measurements around large Wind Turbines. In *EWEC*, Brussels, Belgium, 2008.

[59] Jakob Mann, Jean-Pierre Cariou, Michael S. Courtney, Rèmy Parmentier, Torben Mikkelsen, Rozenn Wagner, Petter Lindelöw, Mikael Sjöholm, and Karen Enevoldsen. Comparison of 3D turbulence measurements using three staring wind lidars and a sonic anemometer. *Meteorologische Zeitschrift*, 18(2):135–140, April 2009.

[60] Torben Mikkelsen, Jakob Mann, and Morten Nielsen. Rotating prism scanning device and method for scanning, 2012.

[61] Mikael Sjöholm, Nikolas Angelou, Kasper Hjorth Hansen, Jakob Mann, and Torben Mikkelsen. First measurements by the DTU Wind Energy short-range WindScanner. In *EWEA*, Copenhagen, Denmark, 2012.

[62] Jakob Mann, Nikolas Angelou, Mikael Sjöholm, and Torben Mikkelsen. Laser scanning of a recirculation zone on the Bolund escarpment. In *16th International Symposium of the Advancement of Boundary-Layer Remote Sensing*, Boulder, Colorado, 2012.

[63] Mikael Sjöholm, Nikolas Angelou, Per Hansen, Kasper Hjorth Hansen, and Torben Mikkelsen. Helicopter downwash measured by continuous-wave Doppler lidars with agile beam steering Analysis procedure. In *16th International Symposium of the Advancement of Boundary-Layer Remote Sensing*, Boulder, Colorado, 2012.

[64] Leosphere. Lidar news weather & climate, January 2011.

[65] Jean-Pierre Cariou, Laurent Sauvage, Ludovic Thobois, Guillaume Gorju, Mehdi Machta, Guillaume Lea, and Marie Duboue. Long range scanning pulsed Coherent Lidar for real time wind monitoring in the Planetary Boundary Layer. In *16th Coherent Laser Radar Conference 2011*, pages 148–152, Long Beach, California, USA, 2011. Universities Space Research Association.

[66] Sophie Loaec, Ludovic Thobois, Jean-Pierre Cariou, Agnes Dolfi-Bouteyre, and Didier Goular. MONITORING WAKE VORTICES WITH A SCANNING DOPPLER LIDAR. In *16th International Symposium of the Advancement of Boundary-Layer Remote Sensing*, Boulder, Colorado, 2012.

[67] Laurent Sauvage and Ludovic Thobois. Doppler Does It. *Air Traffic Technology International Showcase*, pages 126–127, 2012.

[68] Laurent Sauvage and Ludovic Thobois. CLEAR FOR TAKE-OFF Second-generation LiDAR meets new ATM requirements. *Meteorological technology international*, pages 56–58, September 2011.

[69] Chris Hill and Micheal Harris. QinetiQ Lidar Measurement Report. Technical report, UpWind, 2010.

[70] R. Frehlich, S. M. Hannon, and S. W. Henderson. Performance of a 2-coherent doppler lidar for wind measurements. *JOURNAL OF ATMOSPHERIC AND OCEANIC TECHNOLOGY*, 11(6):1517–1528, 1994.

[71] R. Frehlich. Estimation of velocity error for doppler lidar measurements. *Journal of Atmospheric and Oceanic Technology*, 18(10):1628–1639, 2001.

[72] G. N. Pearson and C. G. Collier. A pulsed coherent co2 lidar for boundary-layer meteorology. *QUARTERLY JOURNAL OF THE ROYAL METEOROLOGICAL SOCIETY*, 125(559):2703–2721, 1999.

[73] P. Drobinski, A. M. Dabas, and P. H. Flamant. Remote measurement of turbulent wind spectra by heterodyne doppler lidar technique. *JOURNAL OF APPLIED METEOROLOGY*, 39(12):2434–2451, 2000.

[74] Philippe Salamitou, Alain Dabas, and Pierre H. Flamant. Simulation in the time domain for heterodyne coherent laser radar. *Applied Optics*, 34(3):499–506, Jan 1995.

[75] Christian J. Grund, Robert M. Banta, Joanne L. George, James N. Howell, Madison J. Post, Ronald a. Richter, and Ann M. Weickmann. High-Resolution Doppler Lidar for Boundary Layer and Cloud Research. *Journal of Atmospheric and Oceanic Technology*, 18(3):376–393, March 2001.

[76] Jeroen De Boeij, Maarten Haazen, Peter Smulders, and Elena Lomonova. Low-latency wireless data transfer for motion control. *Journal of Control Science and Engineering*, 2009:3:1–3:11, January 2009.

[77] N.J. Ploplys, P.A. Kawka, and A.G. Alleyne. Closed-loop control over wireless networks. *Control Systems, IEEE*, 24(3):58–71, 2004.

[78] Johan Eker, Cervin Anton, and Andreas Hörjel. Distributed Wireless Control Using Bluetooth. In *IFAC Conference on New Technologies for Computer Control*, Hong Kong, November 2001.

[79] Nikola Vasiljevic, Guillaume Lea, Michael Courtney, Jörge Schneemann, Davide Trabucchi, Juan-José Trujillo, Robert Unguran, and Juan-Pablo Villa. *The application layer protocol: Remote Sensing Communication Protocol (RSComPro).* DTU Wind Energy E 0017 (EN). DTU Wind Energy, 2013.

[80] Michael Courtney. *Calibrating nacelle lidars.* DTU Wind Energy E 0020. DTU Wind Energy, 2013.

[81] Gene F. Franklin, J. David Powell, and Abbas Emami-Naeini. *Feedback Control of Dynamic Systems.* Pearson Prentice Hall, sixth edition, 2010.

[82] R. Munnig Schmidt, G. Schitter, and J. Van Eijk. *The Design of High Performance Mechatronics.* Delft University Press, 2011.

[83] Jean-Pierre Cariou and Matthieu Boquet. LEOSPHERE Pulsed Lidar Principles - Contribution to UpWind WP6 on Remote Sensing Devices. Technical report, UpWind, 2011.

[84] Nikola Vasiljevic, Michael Courtney, Rozenn Wagner, Jakob Mann, and Torben Mikkelsen. A windscanner simulator. In *EWEC 2011*, February 2011.

Appendix A

CNR Mapper

CNR of the backscatter signal from a hard target (i.e. a non-transparent object) has value which is a few times higher in comparison to CNR of the backscatter signal from aerosols in the atmosphere. This can be seen from the WindScanner CNR curve plotted at multiple distances (Figure A.1) along LOS of the laser beam, which was directed to hit the top of a meteorological mast (Figure A.2). From the curve we can see that the distance at which CNR is highest corresponds to the distance between the WindScanner and the top of the mast.

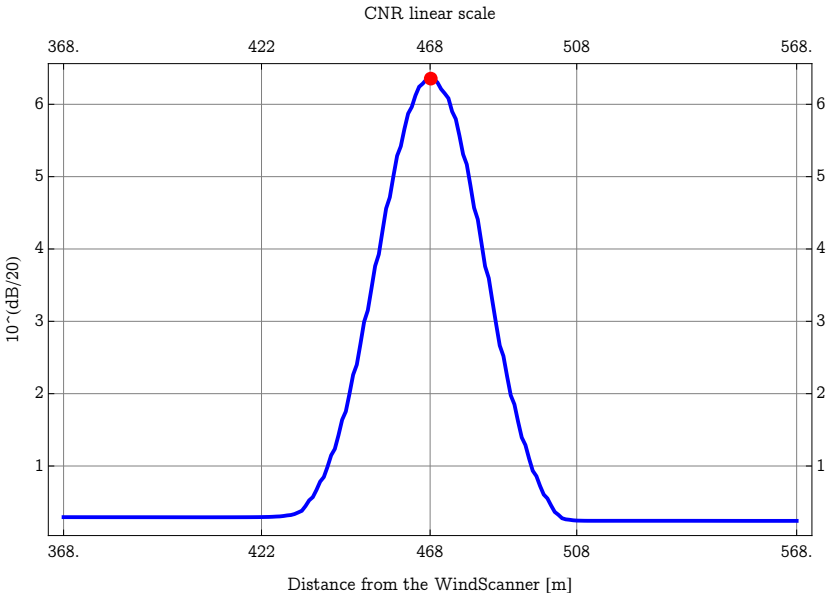

Figure A.1: The distribution of CNR around the top of a meteorological mast. The maximum value is at 468 m.

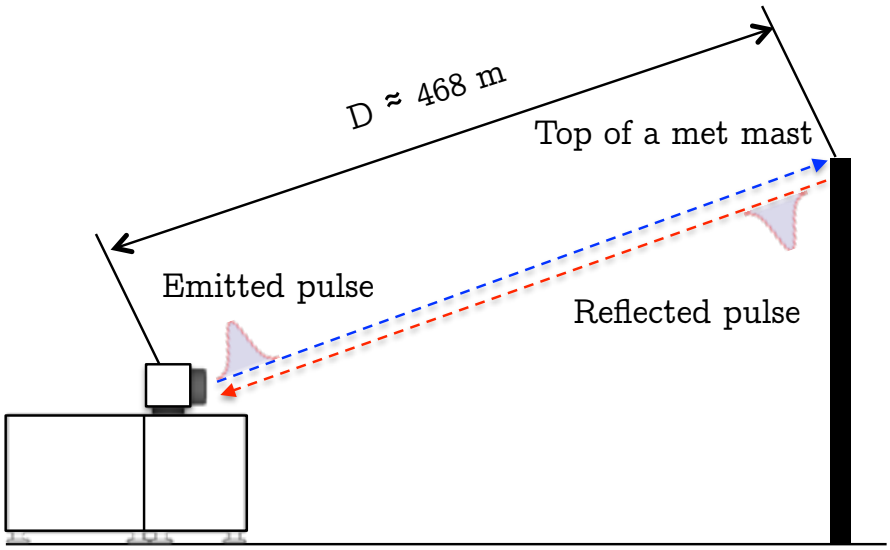

Figure A.2: The laser light is directed to hit the top of a meteorological mast, where the top is aproximatelly located at the distance of 468 m from the WindScanner

Besides the information about CNR at multiple distances, the WindScanner provides the information about the scanner head positions at which CNR has been acquired. This information can be used to perform 3D imaging of surrounding hard targets (trees, meteorological masts, etc.). 3D imaging is useful since it allows the determination of the hard targets positions in relation to the WindScanner, which can be used to further assist different activities such as:

Leveling of the WindScanner

Home position testing

Sensing distance testing

Testing of the mirrors' alignment

Testing of the mechanical system backlash

Optimization and improvement of the measurement scenarios

For the purpose of 3D imaging with WindScanners, a software tool 'CNR mapper' has been developed. This tool plots CNR from preselected distances and preselected scanner head positions.

CNR mapper resides on the master computer where it is linked to the master computer software through which it setups the WindScanner software on a distant WindScanner to perform 3D imaging of surrounding hard targets. Setting up the following parameters of the software:

- Start azimuth angle, θ_{start}

- Stop azimuth angle, φ_{start}
- Start elevation angle, θ_{stop}
- Stop elevation angle, φ_{stop}
- Elevation step, $\Delta\theta$, or Azimuth step, $\Delta\varphi$
- Speed of the rotation around the azimuth or elevation axis
- Accumulation time
- Distance(s)

forms the 3D imaging scenario which consists of multiple PPI or RHI measurement scenarios that guide the scanner head to direct the laser beam and acquire the backscattered light from a hard target(s) (Figure A.3). Once the scenario is started, the master computer receives data from the WindScanner consisting of CNR, azimuth angle (θ), elevation angle (φ) and distance from which the backscattered light was acquired. This information is forwarded to CNR mapper that forms a 2D image of CNR for each distance, where the values of CNR are georeferenced at the 2D plane of the image, having the coordinates of the corresponding scanner head positions. In this way, CNR mapper forms multiple 2D georeferenced images which if composed properly can create a 3D image of hard targets around the WindScanner. An example of the hard target 3D imaging using multiple PPI scenarios and the formation of the georeferenced image from a single distance is given in Figure A.4.

From this same figure we can see that the resolution of the georeferenced image depends on parameters used to set the 3D imaging scenario. The maximum resolution of the 2D images is defined with the lowest pixel dimensions. Since the lowest tested speed of rotation is $0.01°/s$, the minimum accumulation time is $100 milliseconds$, and the lowest tested elevation step is $0.001°$ the lowest dimensions of a pixel are $0.001°$ for the azimuth and elevation dimensions. On the other hand, the 2D images from two consecutive distances have a lowest separation of 0.6 m due to 250 MHz sampling frequency of the backscattered light.

With these inherent properties of the WindScanner, CNR mapper is able to form the georeferenced images which allow determination of hard targets' positions in respect to the WindScanner, with the accuracy of $0.001°$ for the azimuth and elevation angles, and 0.6 m for the distance.

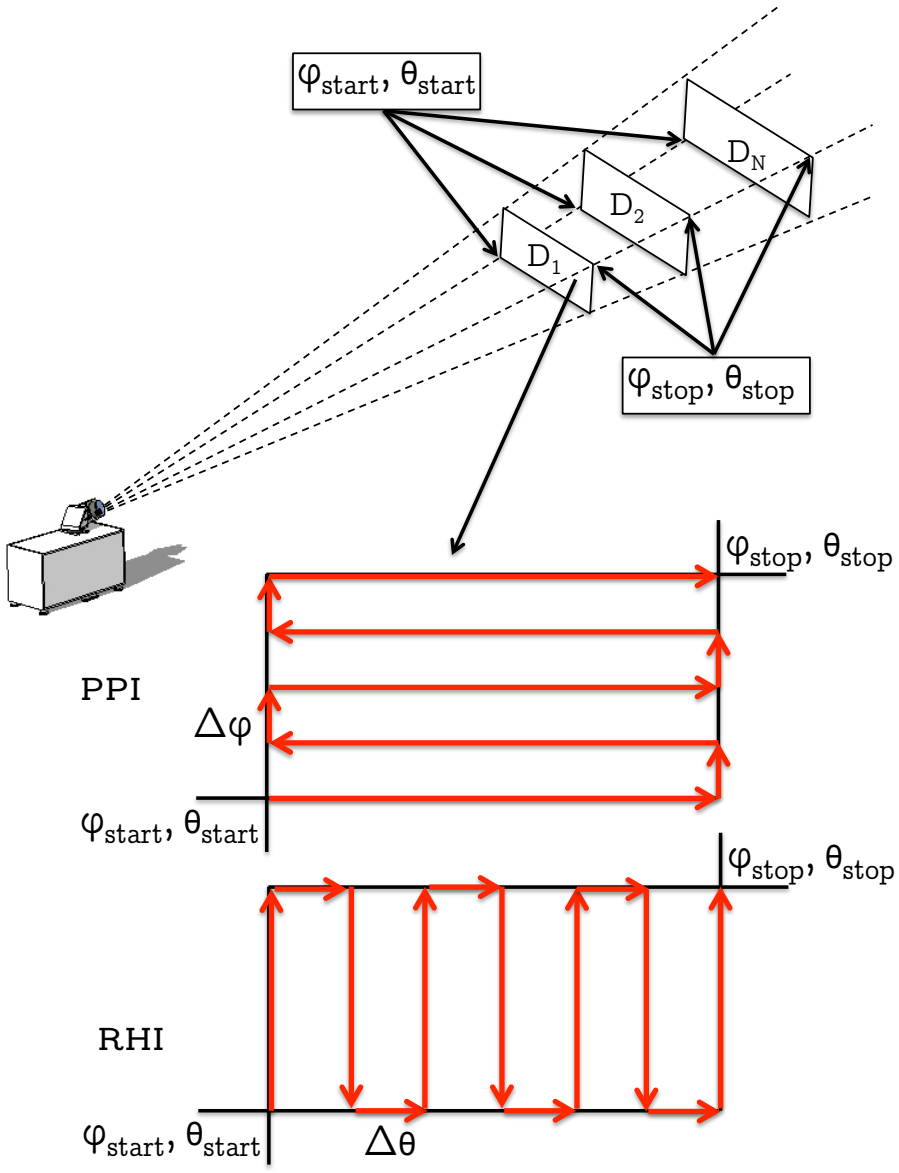

Figure A.3: 3D imaging scenario usually comprises acquisition of CNR from multiple distances within a frame bounded by the start and stop azimuth and elevaiton angles. It can be performed either using multiple PPI or RHI scenarios.

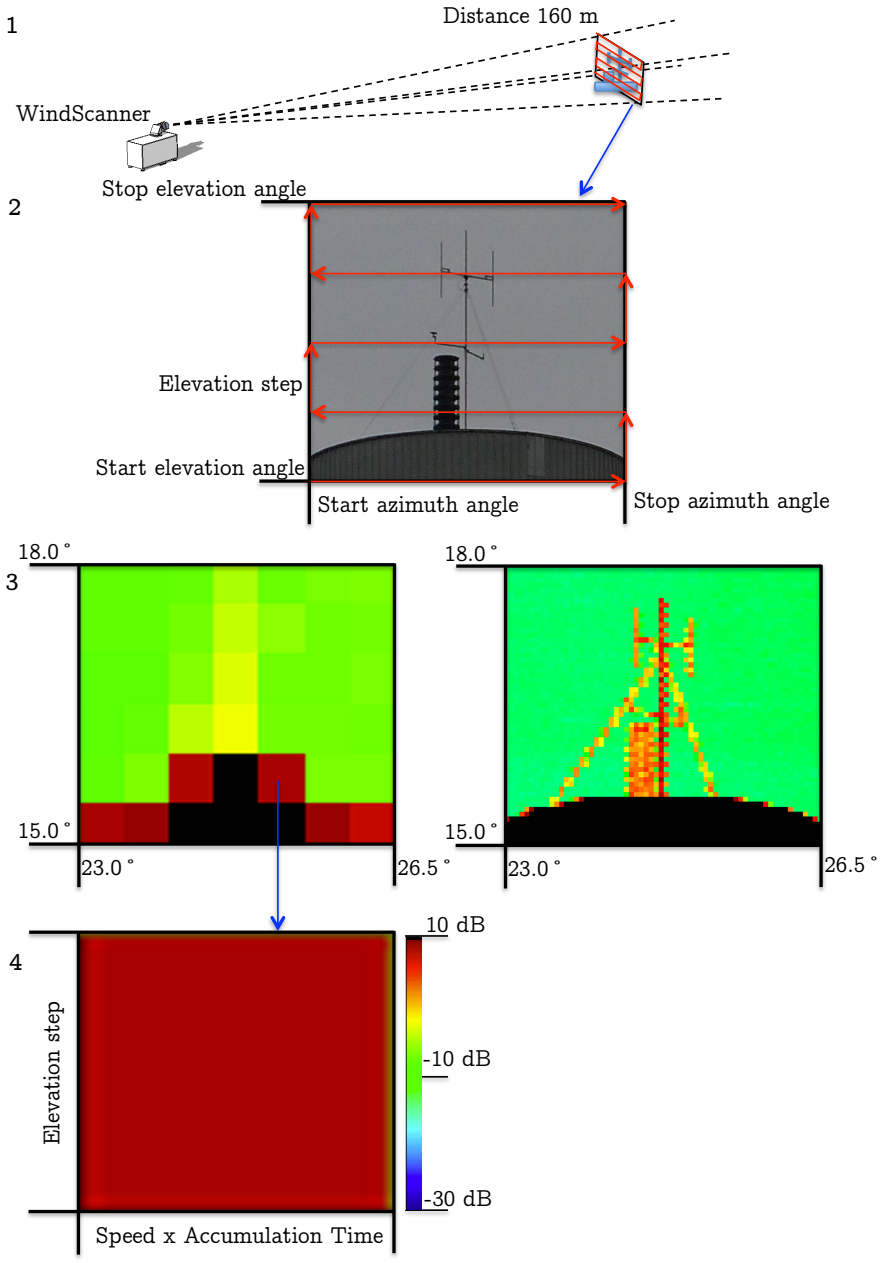

Figure A.4: 1 - Directing the laser beam to scan the top of the water tower at 160 m from the WindScanner. 2 - Configuration of the 3D imaging scenario, consisting of multiple PPI scenarios. 3 - Georeferenced images of the water tower top in the coarse resolution (left) and high resolution (right). 4 - Pixel dimensions.

Appendix B

Approximation of the mirrors influence

Let us consider that only mirror 3 is rotated around the X axis of the mirror 3 coordinate system for the angle α_3 (Figure B.1). Due to this angular displacement, the expected laser beam direction, given the command azimuth and elevation angles of the scanner head, will be displaced for this angle. If the same mirror is rotated around the Y axis of the mirror 3 coordinate system for the angle β_3 (Figure B.2), this angular displacement will cause the displacement of the expected laser beam direction for the angle ξ_3. Based on Figure B.3, it can be shown that the value of this angle is equal to:

$$\xi_3 = \beta_3 \sin(45^\circ) \tag{B.1}$$

In order to simplify the derivation of the influence of these angular displacements on the change of the expected laser beam direction, we will assume that the laser beam origin P_3, the rotation axes intersection P_2 and the first reflection point P_1 coincide (**??**). This assumption is justified for the radial velocity acquisitions from points of interests which are some tens of meters away from a WindScanner. Also, let us consider that the scanner head is in the home position (i.e. the commanded azimuth and elevation angles equal to 0°).

Under these two assumptions, the angular displacement α_3 will cause the change of the azimuth angle of the expected laser beam direction for the same value (Figure B.5, 1). Similarly, the angular displacement ξ_3 will displace the expected laser beam direction around the elevation angle for the value equal to ξ_3 (Figure B.5, 2). If both displacements occurs, the expected laser beam direction azimuth and elevation angles will be changed for α_3 and ξ_3, respectively (Figure B.5, 3).

Following the same logic, if all three mirrors are rotated around the X and Y axes of their coordinate systems, these deviations will produce a combined effect on the expected laser beam direction given with the following equations:

$$\theta_a = \theta_c \pm (\alpha_3 + \alpha_2 + \alpha_1) \tag{B.2}$$

$$\varphi_a = \varphi_c \pm (\beta_3 + \beta_2 + \beta_1)\sin(45°) \tag{B.3}$$

where indices a and c relate to the actual and commanded values of the azimuth and elevation angles of the laser beam direction.

Now let us consider that the points P_1, P_2 and P_3 do not coincide and that the scanner head rotates. It is likely that the changes of the azimuth and elevation angles of the expected laser beam direction will depend on both the angular displacements β_1, β_2, β_3, α_1, α_2 and α_3, as well as the scanner head position.

The exact functions that describe the impact of angular displacements and scanner head position on the azimuth and elevation angles of the expected laser beam direction have not been derived yet. Therefore, if we consider the graphical representation of the impact of the angular displacements α_1,α_2 and α_3 and the scanner head position on the expected laser beam direction (Figure B.6 - B.8), it is possible to approximate these functions as the following:

$$\theta_a = \theta_c \pm (\cos(\varphi_c)\alpha_3 + \cos(\varphi_c)\cos(\theta_c)(\alpha_2 + \alpha_1)) \tag{B.4}$$

$$\varphi_a = \varphi_c \pm (\sin(\varphi_c)\alpha_3 + \sin(\varphi_c)\sin(\theta_c)(\alpha_2 + \alpha_1)) \tag{B.5}$$

If we anticipate a corresponding impact of the angular displacements β_3,β_2 and β_1 and the scanner head position on the expected laser beam direction, we can extend the previous set of relations with terms related to the angular displacements β_3,β_2 and β_1 :

$$\begin{aligned}\theta_a = \theta_c &\pm (\cos(\varphi_c)\alpha_3 + \cos(\varphi_c)\cos(\theta_c)(\alpha_2 + \alpha_1)) \\ &\pm (\sin(\varphi_c)\beta_3 + \sin(\varphi_c)\sin(\theta_c)(\beta_2 + \beta_1))\sin(45°)\end{aligned} \tag{B.6}$$

$$\begin{aligned}\varphi_a = \varphi_c &\pm (\sin(\varphi_c)\alpha_3 + \sin(\varphi_c)\sin(\theta_c)(\alpha_2 + \alpha_1)) \\ &\pm (\cos(\varphi_c)\beta_3 + \cos(\varphi_c)\cos(\theta_c)(\beta_2 + \beta_1))\sin(45°)\end{aligned} \tag{B.7}$$

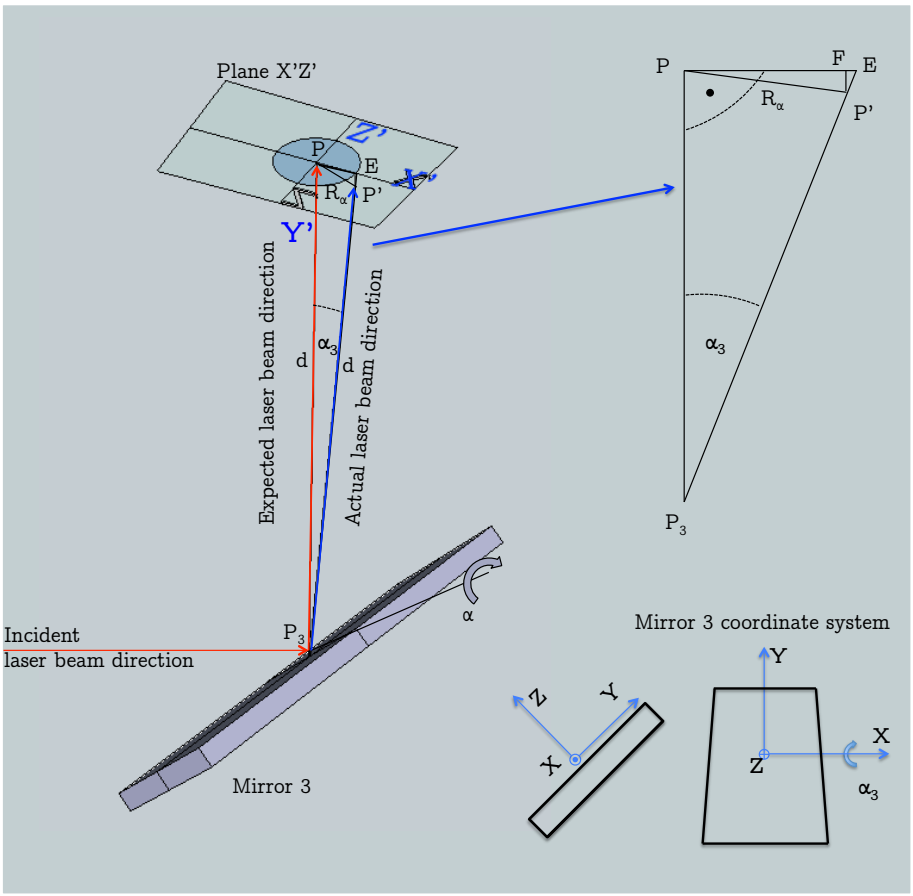

Figure B.1: The reflection of the incident laser beam on the surface of mirror 3 and the position of the laser beam at a distance d in the atmosphere. Point P_3 represents the point of reflection, red arrow lines are the incident laser beam direction and the expected (reflected) laser beam direction. The plane $X'Z'$ is perpendicular to the expected laser beam direction, the center of which P represents the expected laser beam position at the distance d in the atmosphere. Point E lies on the Z' axis.

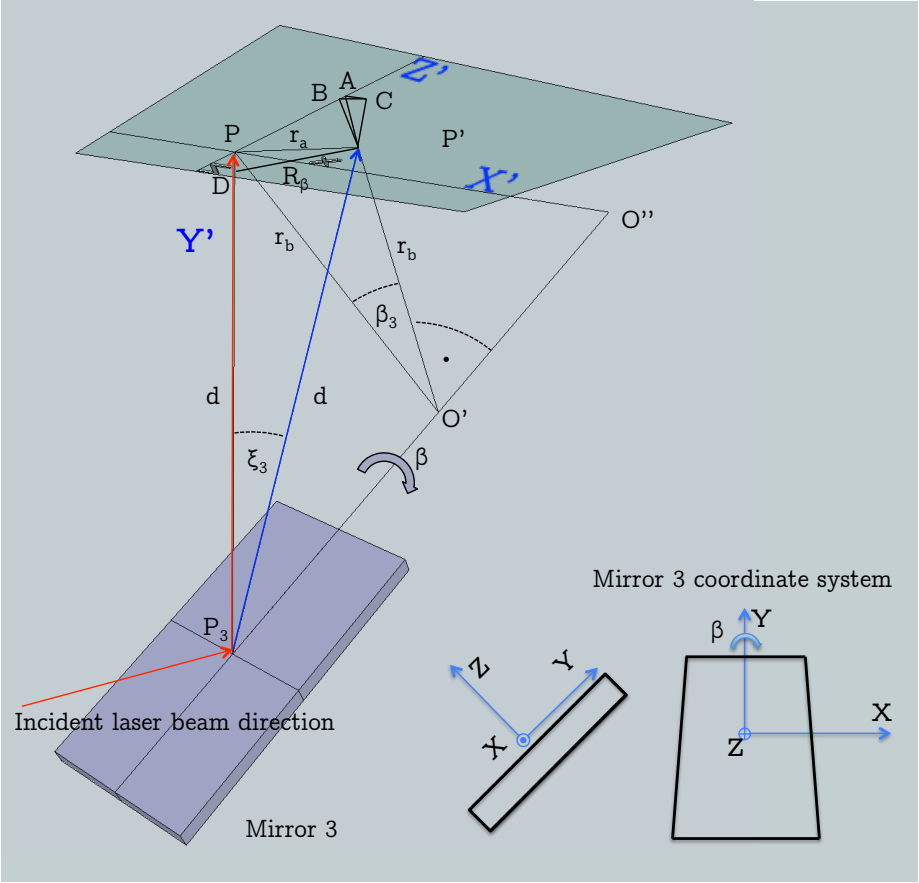

Figure B.2: The reflection of the incident laser beam on the surface of the mirror 3 and the position of the laser beam at a distance d in the atmosphere. The point P_3 represents the point of the reflection, red arrow lines are the incident laser beam direction and the expected (reflected) laser beam direction. The plane $X'Z'$ is perpendicular to the expected laser beam direction, which center P represents the expected laser beam position at the distance d in the atmosphere. Points A and B lay on the Z' axis.

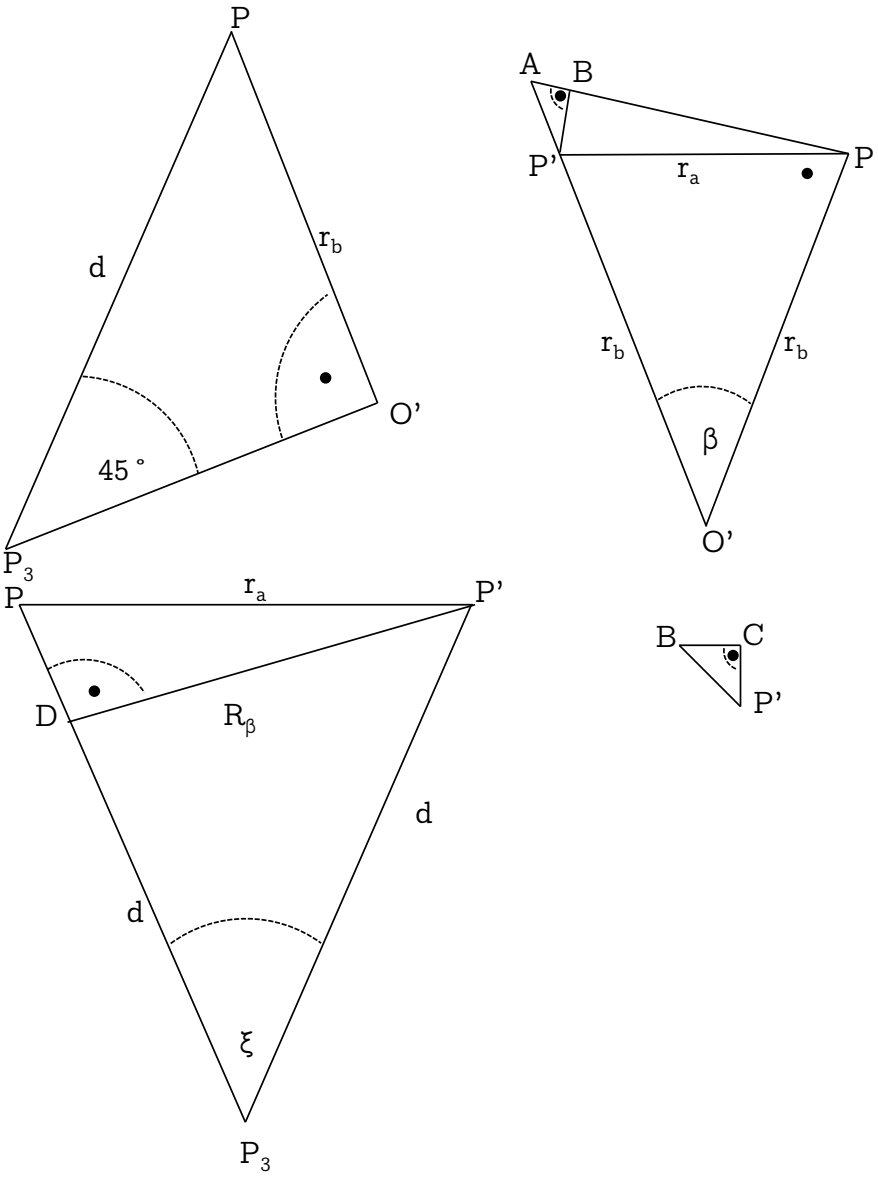

Figure B.3: Decomposing three-dimensional problem showed in Figure B.2 to two-dimensional problem.

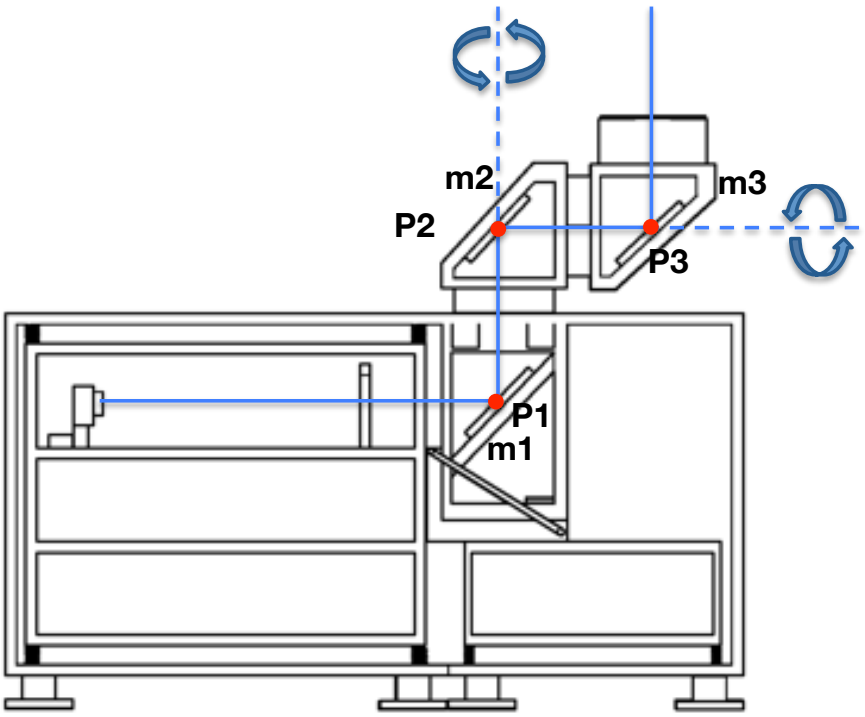

Figure B.4: Position of the reflection points P_1, P_2 and P_3 in respect to the axes of the rotation. The distances P_1P_2 and P_2P_3 are approximately 20 centimeters.

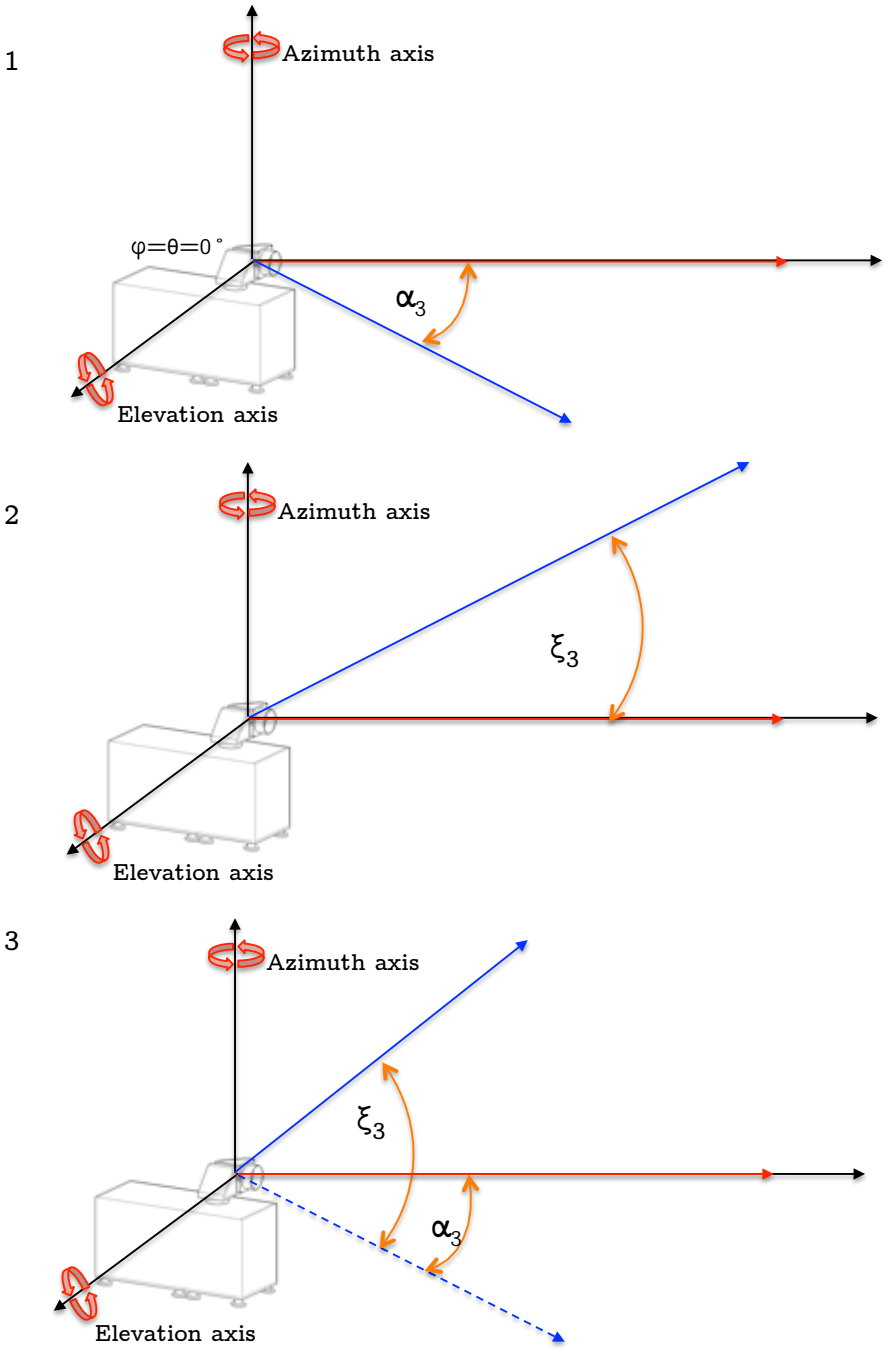

Figure B.5: The scanner head position is fixed to the azimuth θ and elevation φ angles equal to 0°. The red arrow lines represent the expected laser beam direction, while the blue arrow lines are the actual laser beam direction. 1 - Influence of the angular displacement ξ_3 of the mirror 3 on the expected beam position. 2 - Influence of the angular displacement α_3 of the mirror 3 on the expected beam position. 4 - Influence of the angular displacement ξ_3 and $alpha_3$ of the mirror 3 on the expected beam position.

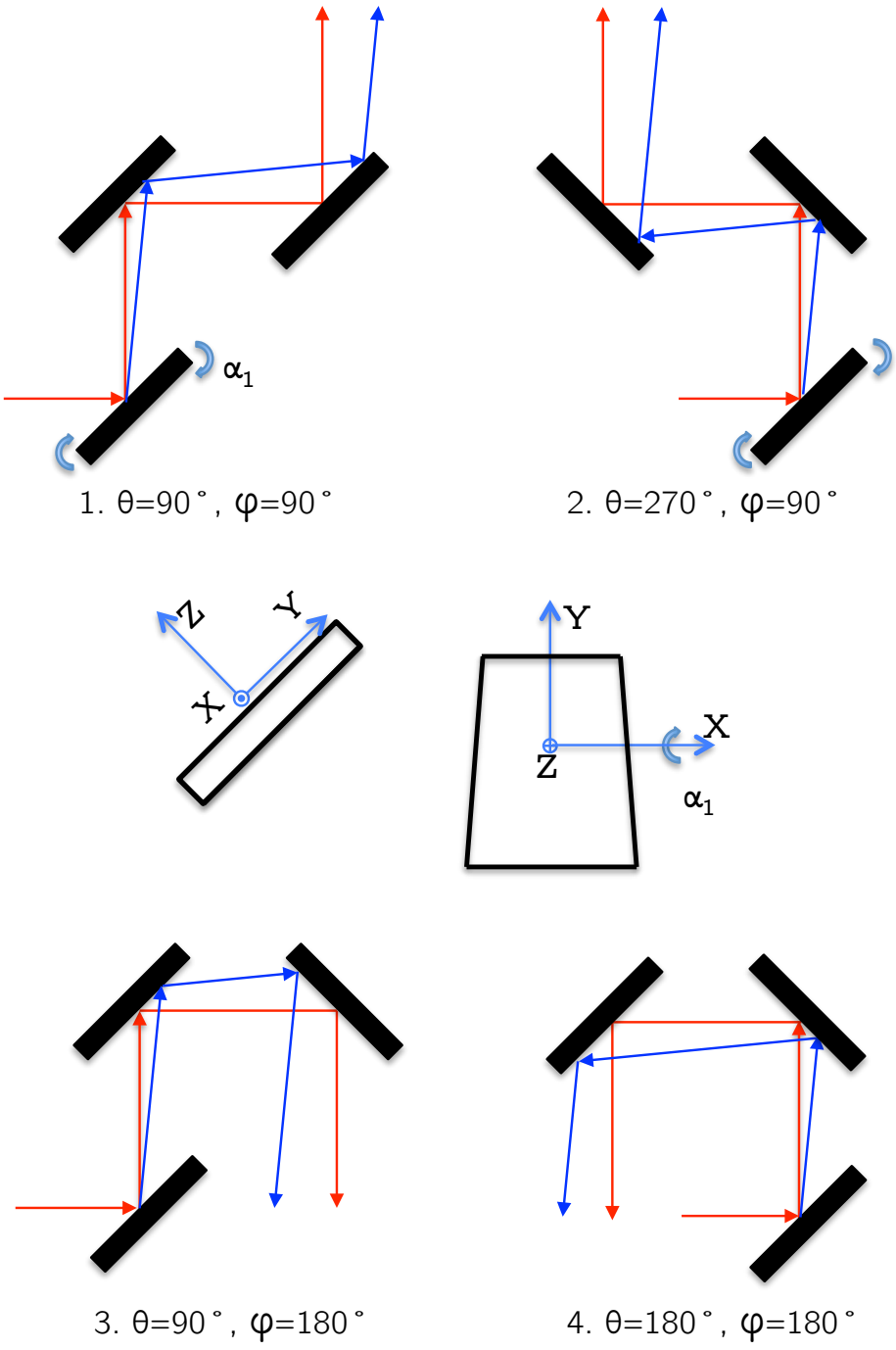

Figure B.6: Influence of the displacement of the mirror 1 on the expected laser beam direction. The red arrow lines represent the expected laser beam direction, while the blue arrow lines are the actual laser beam direction.

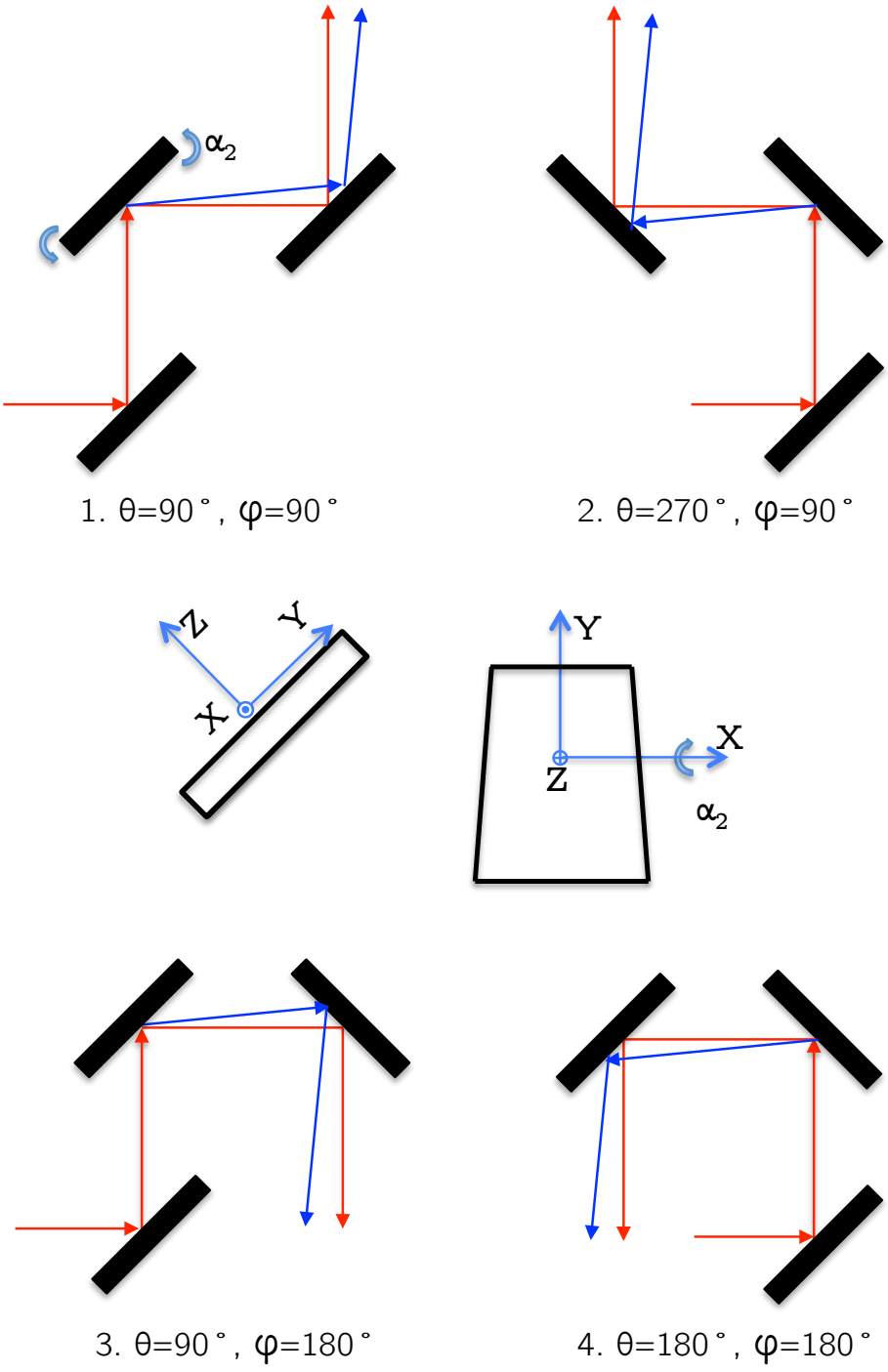

Figure B.7: Influence of the displacement of the mirror 2 on the expected laser beam direction. The red arrow lines represent the expected laser beam direction, while the blue arrow lines are the actual laser beam direction.

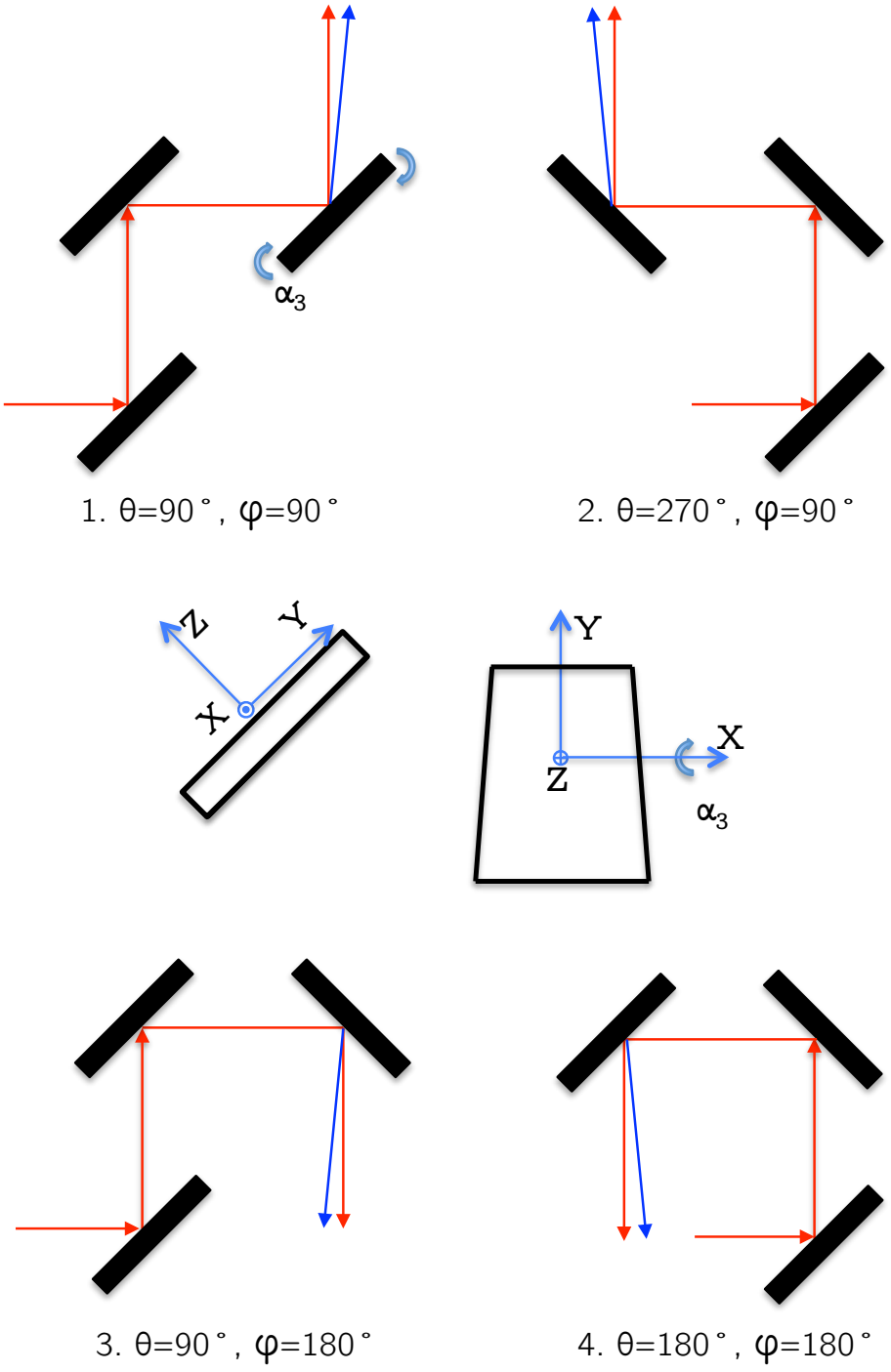

Figure B.8: Influence of the displacement of the mirror 3 on the expected laser beam direction. The red arrow lines represent the expected laser beam direction, while the blue arrow lines are the actual laser beam direction.

Appendix C

Abstract (Danish)

Denne afhandling viser resultater af et PhD studium, som havde til formål at udvikle et system bestående af 3 rum-tid synkroniseret pulset, kohærent Doppler "scanning" lidars koordineret af en fjern "master computer". Dette system har den unikke egenskab, at den kan måle en komplet tredimensional strømning ved at udsende laserstråler fra tre rumlig fordelte lidars, styre de tre stråler til at mødes i et punkt og bevæge skæringspunktet over et område af interesse.

Hver enkelt lidar er baseret på anvendelsesprincipper, der tillader nøjagtig synkronisering af laserpulsgeneration, laserpulsstyring og opsamling af det tilbagekastede lys. Principperne muliggør også nøjagtig tidsstyring af disse processer. Dette resultat er opnået gennem en ligestilling af lysemissionsprocessen med en stepmotor akseldrejningsproces. Både lidar- (lysemission, styring og opsamling) og stråleposition styring dirigeres af et enkelt komponent, nemlig bevægelsesstyringsenheden.

Systemet er konstrueret ved brug af en original fremgangsmåde, hvor en 'master computer' koordinerer samtlige fjerntliggende lidars ved hjælp af en datapakkeudveksling, over et UDP/IP og TCP/IP netværk. Da pakkens størrelse typisk er 1 kB, er hurtig og mulig uafbrudt koordinering af lidar'erne muligt, selv med langesomme netværkstyper, som GSM. En maksimal tidsforskydning af 10ms er observeret mellem lidar'er i systemet.

Laserstrålens positionsnøjagtighed af hver lidar er estimeret til $\pm 0.5^\circ$ for retningsnøjagtighed og cirka ± 5 m for måleafstand. Ved hjælp af forbedret procedurer, kan positionsnøjagtigheden øges med en faktor 20.

Afslutningsvis blev to eksperimenter udført, hvor multi-lidar systemet blev anvendt til synkroniserede målinger af vindhastighedsfelter i flere punkter i atmosfæren.

DTU Vindenergi er et institut under Danmarks Tekniske Universitet med en unik integration af forskning, uddannelse, innovation og offentlige/private konsulentopgaver inden for vindenergi. Vores aktiviteter bidrager til nye muligheder og teknologier inden for udnyttelse af vindenergi, både globalt og nationalt. Forskningen har fokus på specifikke tekniske og videnskabelige områder, der er centrale for udvikling, innovation og brug af vindenergi, og som danner grundlaget for højt kvalificerede uddannelser på universitetet.

Vi har mere end 240 ansatte og heraf er ca. 60 ph.d. studerende. Forskningen tager udgangspunkt i ni forskningsprogrammer, der er organiseret i tre hovedgrupper: vindenergisystemer, vindmølleteknologi og grundlag for vindenergi.

Danmarks Tekniske Universitet
DTU Vindenergi
Nils Koppels Allé
Bygning 403
2800 Kgs. Lyngby
Telefon 45 25 25 25